Optimisation de la performance thermique du détecteur Pixel Alpine

Zhan Zhang

UNIVERSITÉ GRENOBLE ALPES

THÈSE

Pour obtenir le grade de

DOCTEUR DE L'UNIVERSITÉ GRENOBLE ALPES

Spécialité : **Physique Appliquée**

Arrêté ministériel : 7 août 2006

Présentée par

Zhan Zhang

Thèse dirigée par **Lucia Di Ciaccio**

préparée au sein du **Laboratoire d'Annecy-le-Vieux de Physique des Particules** dans **l'École Doctorale de Physique de Grenoble**

Optimisation de la Performance Thermique du Détecteur Pixel Alpine

Thèse soutenue publiquement le **« 1 Décembre 2015 »**,
devant le jury composé de :

M, Giovanni Ambrosi
Chercheur Sénior, Istituto Nazionaie di Fisica Nucleare, Rapporteur

M, Philippe Schwemling
Professeur, Centre d'etude de Saclay Gif-sur-Yvette, Rapporteur

Mme, Lucia Di Ciaccio
Professeur, Université de Savoie-Mont Blanc, Directeur de thèse

M, Didier Ferrere
Chercheur Sénior, Université de Geneve, Examinateur

M, Stephane Jezequel
DR2, Laboratoire d'Annecy-le-Vieux de Physique des Particules, Examinateur

Mme. Sylvie Rosier-Lees
DR1, Laboratoire d'Annecy-le-Vieux de Physique des Particules, Président du jury

ABSTRACT

The ATLAS (A Toroidal LHC ApparatuS) detector is the largest detector of the Large Hadron Collider (LHC). One of the most important goals of ATLAS was to search for the missing piece of the Standard Model, the Higgs boson that had been found in 2012. In order to keep looking for the unknowns, it is planned to upgrade the LHC. The High Luminosity LHC (HL-LHC) is a novel configuration of the accelerator, aiming at increasing the luminosity by a factor five or more above the nominal LHC design. In parallel with the accelerator upgrade also the ATLAS will be upgraded to cope with detector aging and to achieve the same or better performance under increased event rate and radiation dose expected at the HL-LHC. This thesis discusses a novel design for the ATLAS Pixel Detector called the "Alpine" layout for the HL-LHC. To support this design, a local support structure is proposed, optimized and tested with an advanced CO_2 evaporative cooling system. A numerical program called “CoBra” simulating the two-phase heat transfer inside a pipe is developed by the author using the most up to date CO_2 heat transfer and pressure drop models. In this thesis, the program is mainly used to verify that the CO_2 two-phase cooling system is able to efficiently cool down the Alpine Detector. In addition, a Finite Element Analysis (FEA) model of the local support structure is built and analyzed in order to facilitate the evaluation of the prototypes. The two simulations (CoBra and the FEA) are combined to characterize the thermal performance of two prototypes: Proof-of-Concept prototype (PoC) and Functional-Demonstration (FD) prototype, produced by different institutes. The two prototypes are analyzed and tested. Studies of the systematic uncertainty affecting the result are present. The PoC prototype measurement shows that the Alpine design can be effectively cooled down. The measurements agree with the predictions within the considered systematic uncertainties. The first FD prototype produced based on the Alpine geometry with limited improvement on materials yet show a less satisfactory behavior. Possible effects occurring during the production that can be improved are identified. The future FD prototypes will be produced with an improved production procedure and using new materials in order to obtain the expected thermal performance.

RÉSUMÉ

L'ATLAS (A Toroidal LHC ApparatuS) détecteur est le plus grand détecteur du Grand Collisionneur de hadrons (LHC) du CERN. L'un des objectifs les plus importants de ATLAS était la recherche de la pièce manquante du Modèle Standard, le boson, de Higgs, qui a été trouvé en 2012. Afin de continuer à chercher les inconnues, il est prévu d'améliorer le LHC. La HL-LHC est un projet, visant à augmenter la luminosité d'un facteur cinq ou plus au-dessus de la conception nominale. En parallèle, l'ATLAS sera amélioré pour faire face au vieillissement des détecteurs et parvenir à la même ou meilleure performance avec un taux d'événements augmenté et une dose de rayonnement plus important. Cette thèse discute un nouveau design pour le Détecteur Pixel d'ATLAS, appelé "détecteur Alpine", pour HL-LHC. La structure du support local du détecteur Alpine est proposé, optimisé et testé avec un système avancé de refroidissement à deux phases qui utilise le CO_2. Un programme numérique appelée CoBra simulant le transfert de chaleur à deux phases à l'intérieur d'un tuyau est développé dans cette thèse en utilisant le plus à des modèles de transfert de chaleur la date de CO_2. Dans cette thèse, le programme est principalement utilisé pour vérifier que le système de refroidissement à deux phases CO_2 est capable de refroidir efficacement sur le détecteur alpin. En outre, un modèle analyse par éléments finis (FEA) de la structure de support local est construit et analysé afin de faciliter l'analyse de la performance thermique des prototypes. Les deux simulations (Cobra et la FEA) sont combinés pour caractériser la performance thermique de deux prototypes: Proof-of-Concept prototype (PoC) et fonctionnelle-démonstration (FD) prototype, produit par différents instituts. Les deux prototypes sont analysés et testés. Les études de l'incertitude systématique affecter le résultat est présents. La surement du prototype PoC montre que le design alpin peut être efficacement refroidi. Les mesures concordent avec les prévisions dans les incertitudes systématiques considérées. Le premier prototype FD produit sur la base de la géométrie alpin avec une amélioration limitée sur les matériaux encore montrer un comportement moins satisfaisante. Les effets secondaires possibles se produisant au cours de la production qui peut être amélioré sont identifiés. Les futurs prototypes FD seront produits avec une procédure d'amélioration de la production et l'utilisation de nouveaux matériaux afin d'obtenir la performance thermique prévu.

ACKNOWLEDGEMENT

This thesis has been carried out at the Laboratoire d'Annecy-le-Vieux de Physique des Particules (LAPP), France. Many great people have contributed to this thesis, even though only my name shows up on the cover page. I owe my gratitude to all of them. The experience and research ability I gained from them would be cherished forever.

My deepest appreciation goes for my advisor Professor Lucia Di Ciao. Thanks for giving me the opportunity and motivation to undertake this work. She had directed me by her strong physics background and spent a lot of time at discussing my manuscript. It is her confidence and the responsibility that finally granted me throughout my PhD study. I could not have imagined having a better advisor and mentor.

Besides my advisor, my sincere thanks go to the engineer Pierre Delebeque. He has always been available at LAPP for deep discussion and idea exchange. For the past three years, Pierre was willing to share his office with me and very often we chatted on the culture and the life in France, which helped me have a deep understanding about the country.

A special gratefulness is for Teddy Todorov, who introduced me to the group ATLAS-LAPP in 2012 when the IBL detector was under construction. It was him who convinced me that the upgrade of the future ATLAS Inner Detector would be a very interesting and special project and a good opportunity for me to further my knowledge. Even though, Teddy was not with us anymore, I often recall our casual talk on the way to Annecy, his humor and smiling, patient explanation for all my questions. I wishes all the best for his beautiful wife and two lovely daughters. I would like to thank the ATLAS-LAPP group to have welcomed me among them. I am also grateful to all my fellow labmates who have involved in this thesis, it is their help make it possible.

I would like to acknowledge several people from outside LAPP for their exceptional help and advice. Dr. Bart Verlaat from NIKHEF, Netherlands, for sharing his insightful idea and extensive experiences accumulated from the CO_2 two-phase cooling system. Paolo Petagna, the cooling manager from CERN, shared his expertise on heat transfer and had deep discussions and lectures with me on the related topics that helped me improve my knowledge in the area. The great thanks goes to Professor Zhenhui He from Sun Yat-sen University, China. His understandings and support are the basic of importance. In addition, I appreciate the help from the colleagues from the AMS-02 experiment.

Finally I thank my family for making my work and life possible by continuous and absolute support. They helped me overcome setbacks and stayed focusing on the study.

Contents

Chapter 1

The LHC and the ATLAS Experiment

This chapter introduces, in Section 1.1, the Large Hadron Collider (LHC) of CERN and presents in Section 1.2 a brief summary of each sub-detector system of the ATLAS detector (A Toroidal LHC ApparatuS). The rest of the chapter is organized as follows: Sections 1.3 and 1.4 describe the upgrade of the accelerator and of the detector, respectively; Section 1.5 presents the alternative layouts for the new ATLAS tracking system; Section 1.6 introduces general aspects of the design of its support structure; Section 1.7 describes the cooling system (another important element of the upgrade of the tracking detector); and finally Section 1.8 summarizes the main content of this thesis work.

1.1 The Large Hadron Collider

The LHC is a very large scientific instrument, which was built with the aim of investigating the fundamental laws of the nature [1]. It is located at the Centre of the European Organization for Nuclear Research (CERN) in Geneva, Swizerland. The LHC is a proton-proton collider, with the capability to collide proton beams up to an energy in the center of mass of 14 TeV. In order to produce beams with such high energy, LHC uses four stages of acceleration chains before reaching the main ring, as shown in Figure 1.1. The main parameters of the LHC are presented in Table 1.1.

Table 1.1: Machine parameters during the 2011 and 2012 data taking periods with proton-proton collisions, compared to the design values. The runs with centre-of-mass energy = 2.76 TeV is not considered.

	2011	2012	Design
centre-of-mass energy	7 TeV	8 TeV	14 TeV
Instantaneous luminosity(cm^{-2-1})	$10^{30} - 3.6 \times 10^{33}$	up to 8×10^{33}	10^{34}
Protons per bunch(10^{11})	$0.6 - 1.3$	up to 1.5	1.15
Number of colliding bunches	$3 \simeq 1332$	up to 1380	2808
Collisions per bunch-crossing	$\lesssim 15$	$\lesssim 35$	22(average)

At the intersection points of the LHC, there are four main detectors: ATLAS [2], ALICE [3], CMS [4], and LHCb [5]. The two general purpose detectors, ATLAS and CMS, are designed to study the theory of the particle interactions of the Standard Model (SM) and the physics beyond it, ALICE is optimized for the study of heavy ion collisions and LHCb is dedicated

to the study of charge-conjugation/parity violation effects and of rare decays of heavy-flavour particles. The work of this thesis is performed in the context of the upgrade of the ATLAS detector.

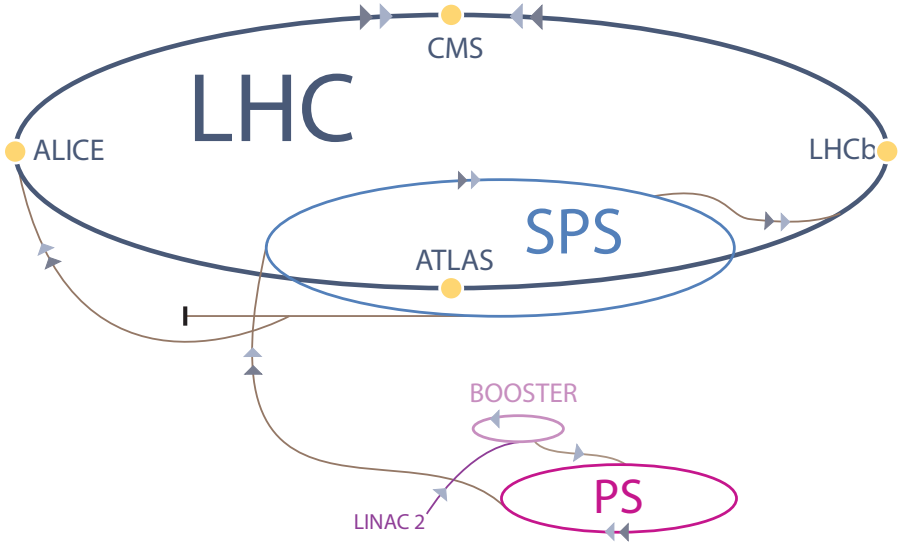

Figure 1.1: A schematic view of the accelerator system for the Large Hadron Collider.

1.2 The ATLAS detector

The ATLAS detector[2, 6, 7] is the largest detector of the LHC. It is 44 m long and has a diameter of about 25 m. One of the most important goals of ATLAS was to search for the missing piece of the Standard Model, the Higgs boson, which was found in 2012[8]. The purpose of the ATLAS detector is now to study in detail this new boson, the Standard Model and to reveal possible new effects beyond it. ATLAS is composed of three high precision sub-detector systems which are concentric around the beam pipe, as shown in Figure 1.2. The innermost part of the detector, the tracking system, imbedded in a solenoidal magnetic field, is used to reconstruct the track of the charged particles and measure their momenta. Outside the tracking system, the electromagnetic and hadronic calorimeters are used to identify and measure the energy of the photons, electrons and hadrons, respectively. The muon detector system, finally, is used to identify and measure the momenta of the muons.

A right-handed coordinate system is defined in ATLAS. The beam interaction point is taken as the origin. The y-axis is defined as pointing from the interaction point to upwards, the x-axis is defined as pointing from the interaction point to the center of the LHC ring, and the z-axis is chosen along the beam direction. The half of the detector at positive z is referred as A-side, the other half is called C-side. Positions in the plane (x-y), transverse to the beam direction are often described in terms of r-φ coordinates. The radial coordinate r, measures in the plane (x-y), the distance from the beam line. The azimuthal angle, ϕ, is the angle around the beam axis, and the polar angle θ is the angle with respect to the beam axis. An important quantity in hadron collider physics is the rapidity, y, of a particle, which is defined as:

$$y = \frac{1}{2} \ln \frac{E + P_z}{E - P_z} \tag{1.1}$$

where E denotes the particle energy and P_z is the momentum component parallel to the beam direction. For massless particles the rapidity reduces to the pseudorapidity, η, which depends

on the polar angle through the relation:

$$\eta = -\ln tan\frac{\theta}{2} \tag{1.2}$$

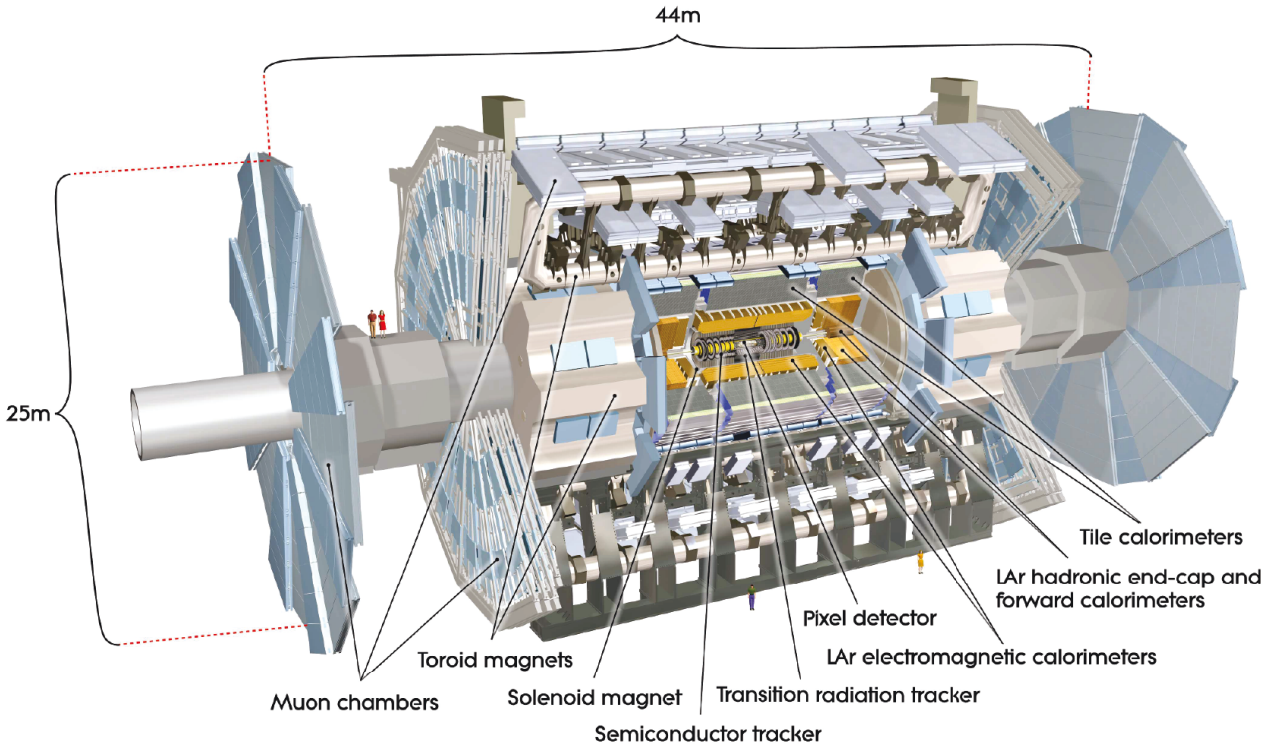

Figure 1.2: A schematic view of the ATLAS detector.

1.2.1 The Inner Detector

The sub-detector system closest to the beam pipe, the Inner Detector(ID), is composed of the Pixel Detector, the Semi Conductor Tracker (SCT) and the Transition Radiation Tracker (TRT) (see Figure 1.3 and 1.4). It has a length of 6.2 m and a diameter of 2.1 m. This part of detector is designed to measure the charge and the momentum of the traversing charged particles by measuring their trajectory. The coverage of the ID is up to $|\eta| < 2.5$.

Pixel Detector

The Pixel Detector is the closest sub-detector to the interaction point, therefore it has to stand high radiation doses. For this reason it is build with hybrid radiation-hard silicon pixel sensors [9]. During Run 1 (2010-2012) of the LHC data taking, the detector was composed of three barrel layers and three end-cap disks. With this configuration, the Pixel detector is able to provide three measurements for each charged particle with a resolution of 10 μm in the (r-φ) plane and 115 μm along the z direction. During the LHC long shut-down, which took place in 2013 and 2014, an additional barrel layer was installed called the Insertable B Layer (IBL)[10, 11]as shown in Figure 1.5.

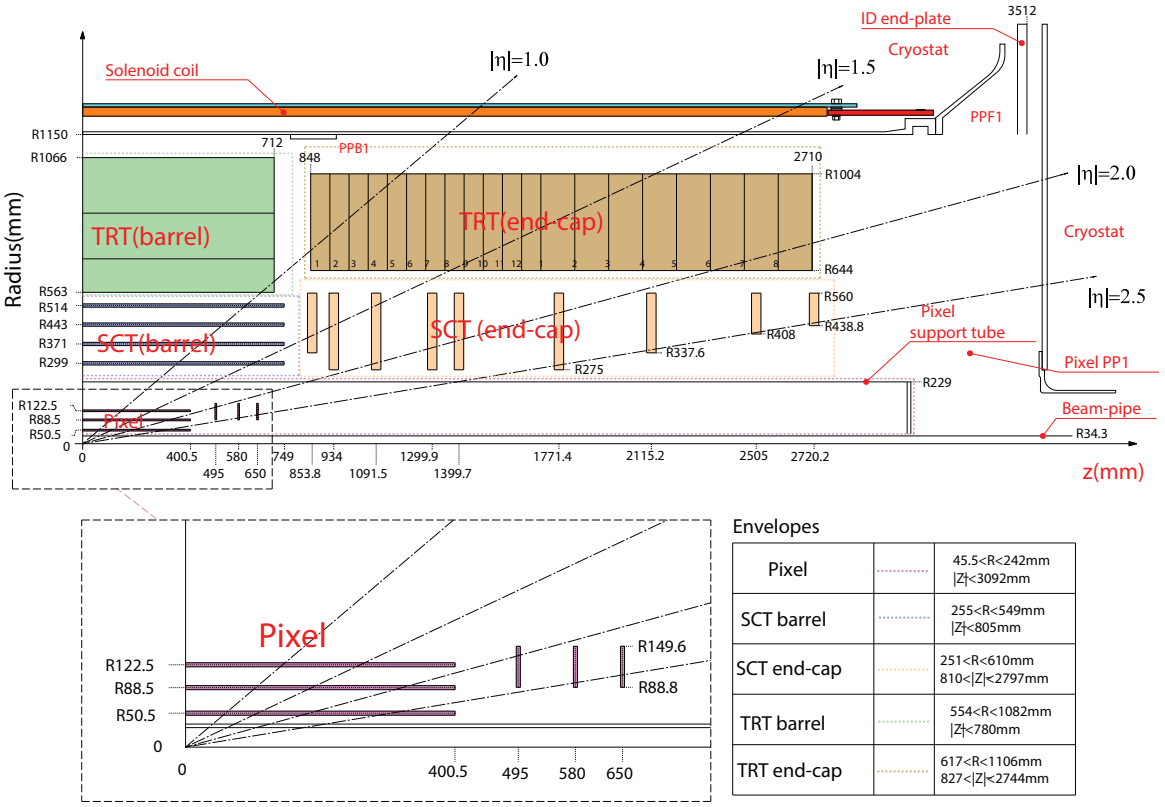

Figure 1.3: Coverage in η of the sub-detectors of the ATLAS Inner Detector

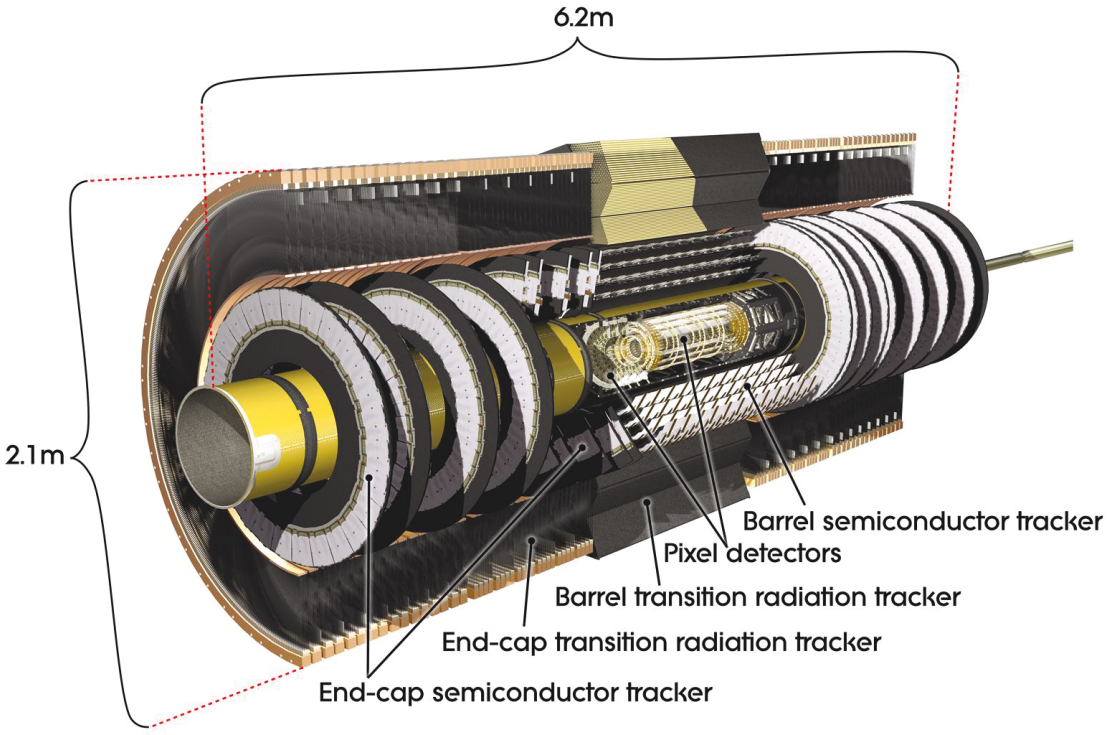

Figure 1.4: A schematic view of the sub-detectors composing the Inner Detector of ATLAS

The Semi Conductor Tracker

The Semi Conductor Tracker (SCT) consists of a barrel region [12] with a cylindrical geometry and an end-cap region [13], where the sensors are mounted on disks. Both the barrel and

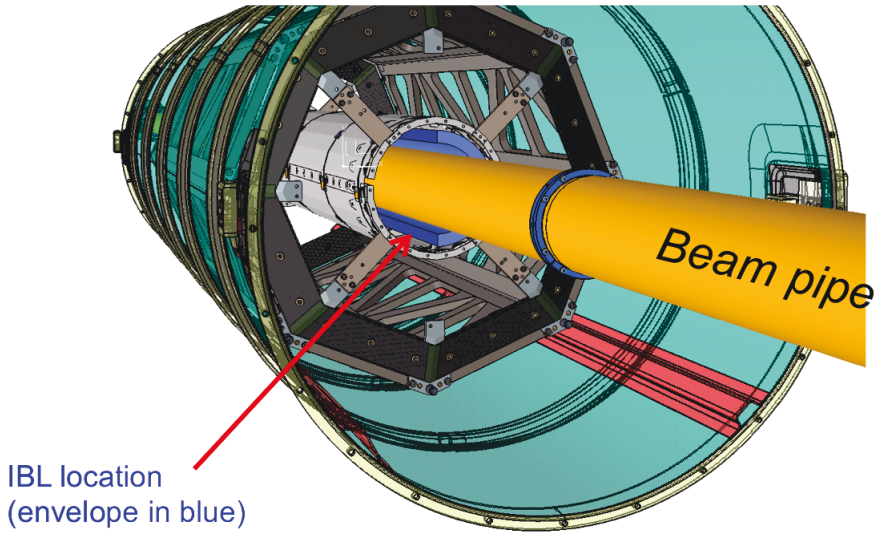

Figure 1.5: Illustration of the IBL location inside the current Pixel Detector.

the end-cap parts use micro-strip sensors made of silicon wafers[14, 15]. The intrinsic spatial resolution in the barrel region is 17 μm in (r-φ) and 580 μm along z. The SCT has physical goals similar to the Pixel Detector.

The Transition Radiation Tracker

At the outermost part of the ID, there is the Transition Radiation Tracker (TRT) composed of drift-tubes [16, 17, 18]. The TRT is 5.3 m long and has a diameter of 2.5 m, thus, its coverage is η <2.0. The gas in which the particles drift is a mixture of 70% Xe, 27% CO_2 and 3% O_2. With this gas mixture, a hit resolution of 130 μm is achieved.

1.2.2 The Calorimeters

The ATLAS Calorimeters are located outside the ID system, and include the Electromagnetic calorimeters[19] delicated to the measurement of the electron and photon energy, and the Hadronic calorimeters focusing on the measurement of hadronically interacting particles [20]. The layout of the calorimeter system is shown in Figure 1.6. By absorbing the energy, most of the particles will be stopped by the Calorimeter system, except the muons and the neutrinos.

1.2.3 The Muon Spectrometer

The Muon Spectrometer(MS) [21, 22] is used to identify the muons and measure their momentum. It is located outside the Calorimeter system. Figure 1.7 shows its layout. The main components of the MS are the toroid magnet system, the monitored drift tubes, the cathode strip chamber, and the resistive-plate chambers.

1.3 The High Luminosity Large Hadron Collider

The LHC has delivered proton-proton collisions at an energy in the center of mass of 7 TeV in 2010 and 2011, and of 8 TeV in 2012. The total integrated luminosity collected by each of the two multi-purpose experiments is about 25 fb^{-1}. The discovery of the long awaited Higgs particle took place in 2012. In order to keep looking for the unknowns, it is planned to upgrade

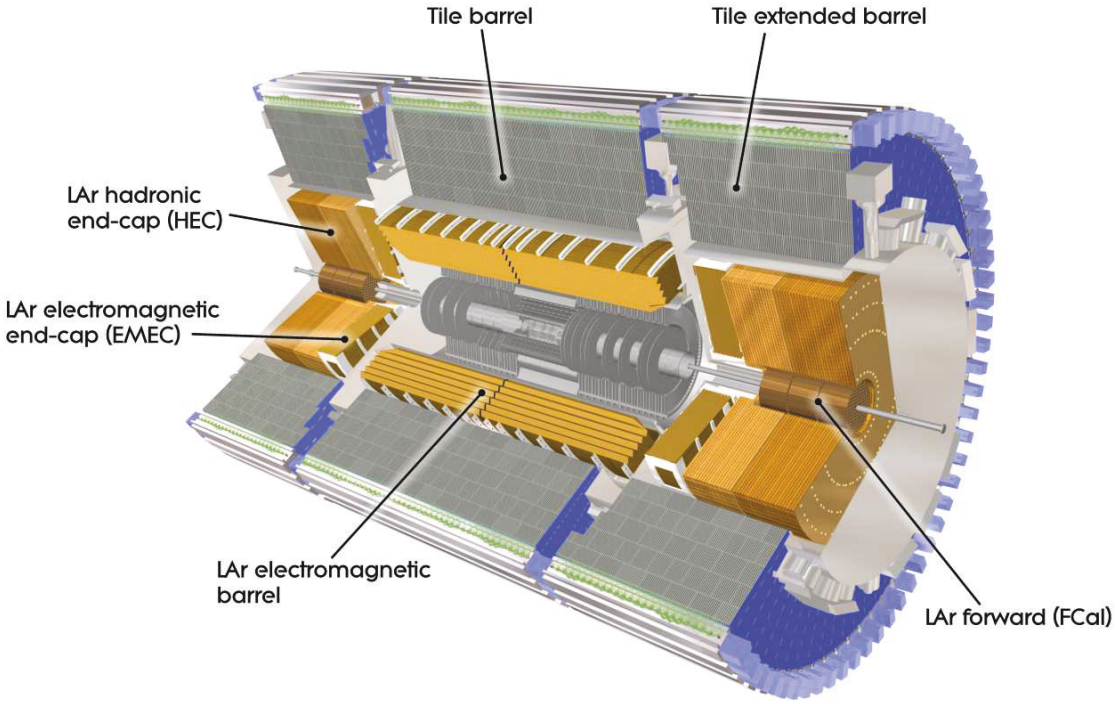

Figure 1.6: The ATLAS Calorimeter system.

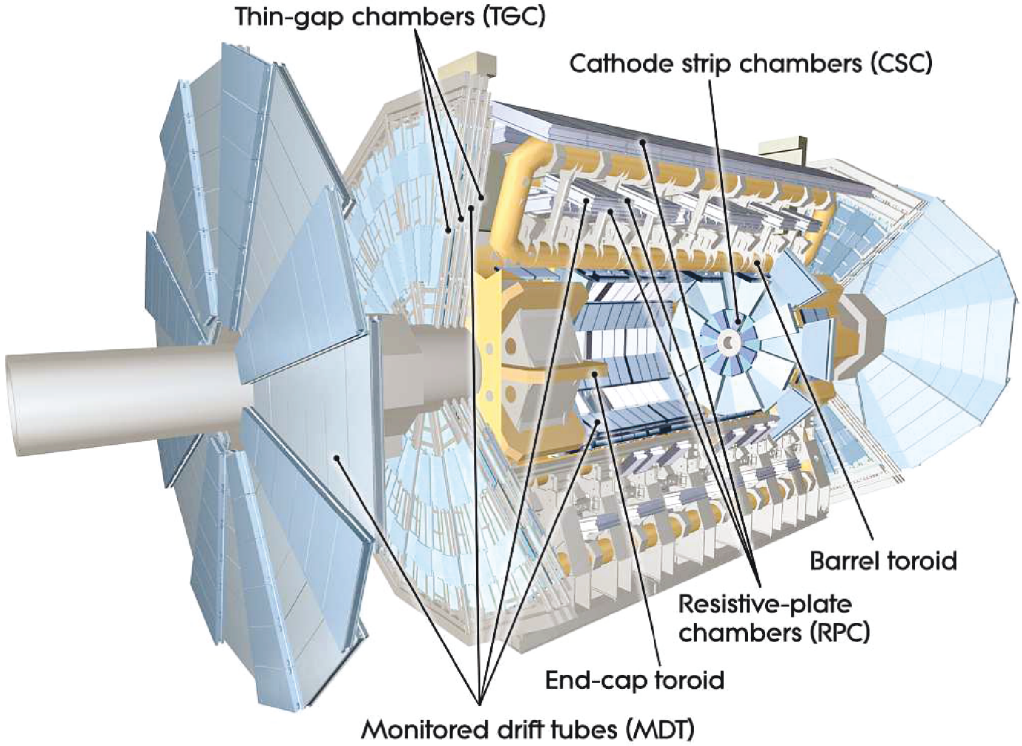

Figure 1.7: The ATLAS Muon system

the LHC. The High Luminosity Large Hadron Collider (HL-LHC) is a novel configuration of the accelerator, aiming at increasing the luminosity by a factor five or more above the nominal LHC design. This should allow to increase the integrated luminosity collected by the multi-purpose experiments ATLAS and CMS from the 300 fb^{-1} of the LHC original design up to 3000

fb^{-1}[23]. At present, it is foreseen that the HL-LHC will begin to provide collisions in 2025.

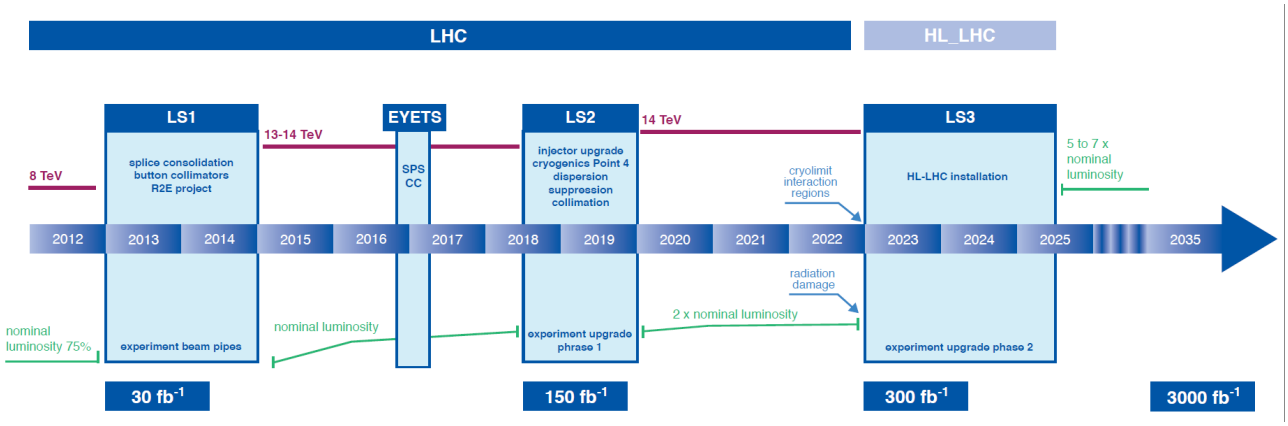

Figure 1.8: LHC delivered luminosity and energy up to now and plans for the next years.

Figure 1.8 shows the LHC energy and the delivered luminosity up to now and plans for the next years. The energy of the collisions is shown by the upper (red) line and the luminosity by the lower (green) lines . The first long shutdown (LS1) in 2013-14 had allowed to reach 13 TeV, an energy close to the design energy. During the second long shutdown (LS2) in 2018-19, the upgrade of the LHC injectors will take place. After LS3 (2023-2025), the machine will be in the High Luminosity configuration.

1.4 ATLAS upgrade

In parallel with the accelerator upgrade also the LHC detectors will be upgraded. The ATLAS upgrade is planned in three phases, which will take place during three long technical shutdowns of the LHC [23] The motivation of the upgrade is to cope with detector aging and to achieve the same or better performance under increased event rate and radiation dose expected at the HL-LHC.

Phase-0

During LS1, the consolidation of the acceleration took place. This should allow to reach safely the nominal design energy of 14 TeV, after a starting period at an energy in the centre of mass of 13 TeV. ATLAS had used this period for a "Phase-0" upgrade of some detector components. A major upgrade activity was the installation of a new barrel layer in the Pixel Detector, called the Insertable B-Layer (IBL) [10, 24]. This is a fourth layer added between a new beam pipe and the innermost layer of the Pixel Detector. The IBL is composed of 14 support structures, called staves. Each stave is instrumented along 64 cm long and 2 cm wide and is equipped with 32 front-end chips and sensors facing the beam pipe. The η coverage of IBL is up to 2.5 [25]. In order to deal with high radiation and pixel occupancy due to the proximity to the interaction point, a new read-out chip, called FE-I4 [26] is developed. There are two types of sensors named planar [27] and 3D [28, 29]. The planar technology is used in the central region and the 3D technology is used in the forward region. Figure 1.9 shows the locations of the IBL sensor types, the general layout and the stave configuration.

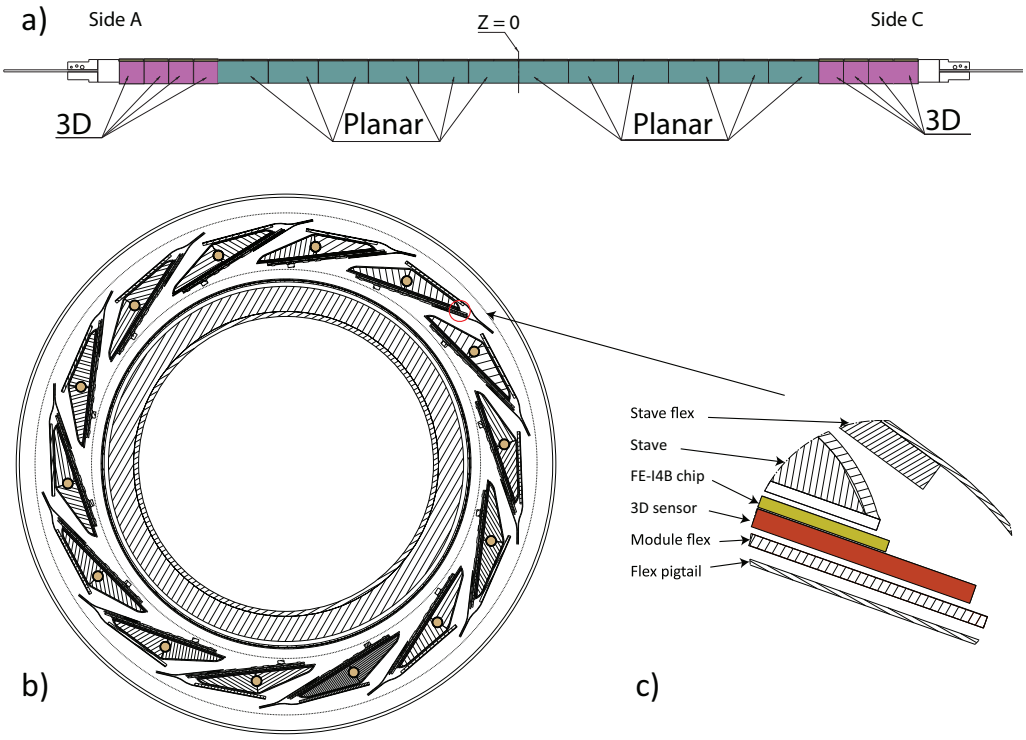

Figure 1.9: Layout of the IBL detector: a) sensor type on each stave, b) transverse view of the detector, c) detailed structure of the stave.

Phase-I

The LHC will undergo further upgrade during LS2 starting in 2018. The corresponding ATLAS upgrade activities, called ATLAS upgrade of Phase I, will involve an upgrade of the Muon Spectrometer, the upgrade of the Calorimeter read-out system as well as various improvement of the forward detectors.

Phase-II

The HL-LHC luminosity goals require a substantial upgrade of the ATLAS tracking system, to cope with five times the nominal LHC instantaneous luminosity (5×10^{34} cm^{-2} s^{-1}), and the full exploitation of the physics accessible with a total integrated luminosity up to 3000 fb^{-1}. The Pixel Detector may be the first part of the tracker that will show limitations in rate and therefore must be upgraded. It is expected that the work of redesigning and replacement of the detector will take about 10 years including prototyping and testing, therefore this work should start now in order to have the detector ready to be installed during the LS3. In the following section, alternative designs of the ID will be presented. The work of this thesis is focused on one of the proposals, called the Alpine design.

1.5 The new Pixel Detector

1.5.1 Alternative layouts

In order to improve the performance of the ATLAS Inner Detector, several layouts for the pixel part are proposed. An optimal design will result from a compromise which should take into

account the following aspects: tracking performance, easiness of construction and installation, ability to maintain an efficient detector throughout its lifetime as well as cost optimization [30].

To design a robust tracking detector and to have enough redundancy to cope with possible dead modules, the goal of the upgraded ID is to have on average 14 hits per particle track. For illustration purpose, Figure 1.10 presents a baseline design. The barrel part consists of four pixel layers with a minimal radius of 39 mm and a maximal radius of 250 mm. Six pixel disks were originally foreseen for the end-cap region. This layout will not be considered for the final upgrade due to several issues. For example, the placement of large disks in the end-cap region poses an engineering problem to the routing of the services of the pixel modules. In addition, the layout is not optimal in terms of the amount of silicon required. The total silicon area is 8.2 m^2 (5.1 m^2 for the barrel and 3.1 m^2 for the end-cap). It is desirable to minimize the amount of silicon, mainly to reduce the costs. Starting from this baseline, three additional optional

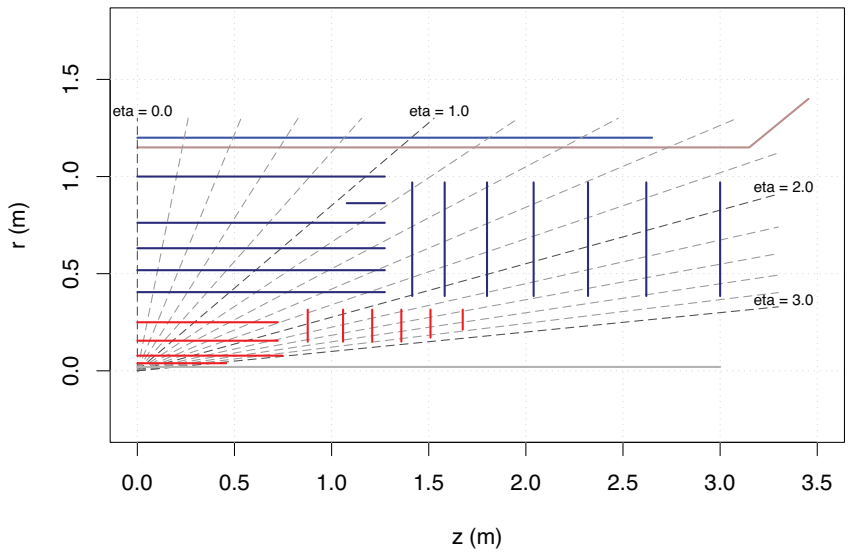

Figure 1.10: Baseline layout for the Inner Detector upgrade. The Pixel detector is shown in red.

designs covering a pseudorapidity region up to 2.7, were proposed at the time of the start of this thesis and will be described in the following. They are named as End-cap Ring layout, Conical layout and Alpine layout.

End-cap Ring layout

This layout is proposed in order to facilitate the routing of the services. It represents an improved version of the baseline design described above. As shown in Figure 1.11, the End-cap Ring layout modifies the end-cap region by replacing the large disks with a series of open pixel rings. The pixel area in the end-cap region is reduced from 3.1 m^2 to 2.6 m^2 compared to the baseline design. In addition, this design can be easily extended further with additional rings into the region at $\eta > 3$.

Conical layout

This layout has been proposed with the main aim of reducing the material crossed by the particle in the transition area between the barrel and end-cap region. As one can see from Figure 1.12, this layout introduces bent layers in the transition region, namely, a flat middle

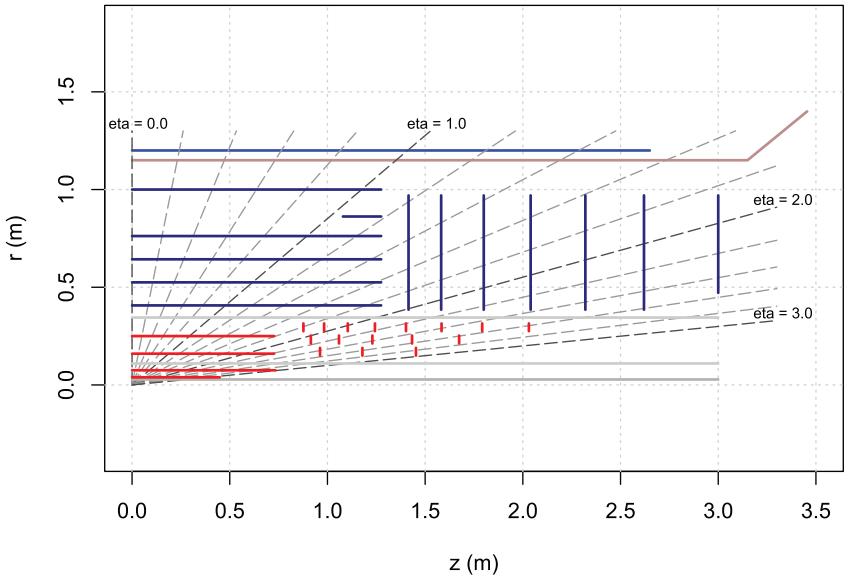

Figure 1.11: The End-cap Ring layout (in red) for the upgrade of the Pixel Detector.

section and a bent inwards geometry for the two outer layers. In this design, the active material traversed by a particle in the transition region is reduced since the crossing angle of particles emerging from the interaction point and incident on the detector is closer to 90^o. The two outer barrel layers in the Conical design are shorter compared with the baseline design and end at $z = 0.6$. With respect to the baseline design, the silicon area in the barrel region is reduced from 5.1 m^2 to 4.6 m^2.

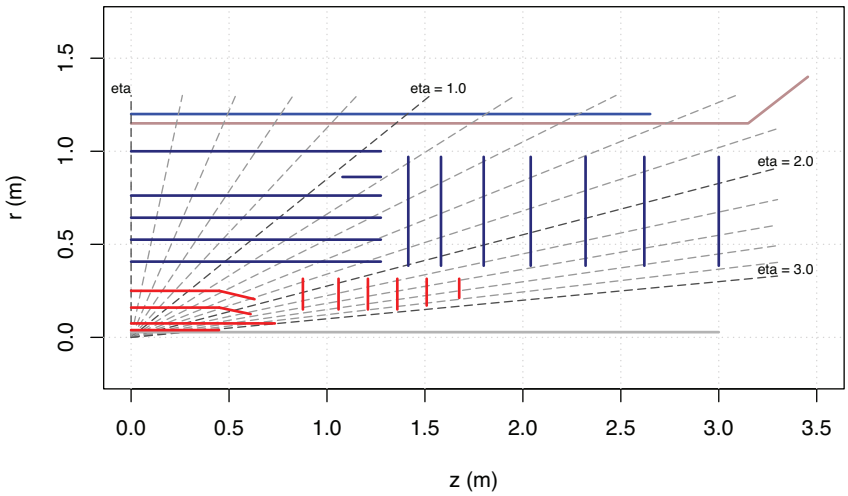

Figure 1.12: The Conical layout for the Pixel Detector upgrade.

Alpine layout

In order to minimize the material crossed by a particle, the ideal design for a tracking detector is to place the sensors in such a way that a particle emerging from the interaction point, crosses them almost perpendicularly. The distance between sensors should also be adjusted to guarantee a good hermeticity. The Alpine layout is an innovative design, proposed in order to satisfy these requirements. In the Alpine design, the central part of each layer and the innermost

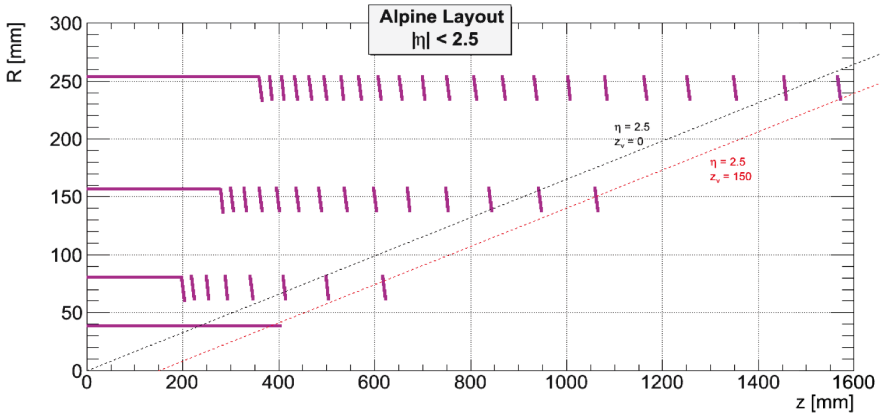

Figure 1.13: The Alpine layout for the Inner Detector upgrade.

layer (layer 0) use a classical "barrel" design, namely the sensors are parallel to the beam axis, as in the baseline layout. In the other three layers the sensors at high η ("mountain" region) are placed at an angle of 68^o with respect to the beam axis (see Figure 1.13). The barrel part of these three external layers is shorter compared to the baseline design. With respect to the baseline design, the total silicon area is reduced from 8.2 m^2 to 4.6 m^2. The main advantages of the Alpine layout with respect to the other layouts are:

- There is no gap between the barrel and the end-cap regions, and therefore no loss in the number of hits along a track crossing this region;
- The position along z of the start of the region where the sensors are inclined can be optimized with the sensor orientations close to optimal;
- The end-cap disks are removed and this fact reduces, in practice, the area of silicon by 50%.

1.5.2 Pixel modules

The core units of a Pixel Detector are the modules. They are highly integrated electronic units, including pixel sensors, readout chips bonded on the pixel sensors and hybrid circuits bonded on the readout chips. To cope with the higher instantaneous luminosity, that will be reached during the Phase-II, it is necessary to enhance the existing sensor technologies and electronics in terms of radiation hardness and occupancy. According to the Letter of Interest (LoI) for the phase II upgrade [30], different types of modules will be used for the upgrade of phase II. They are:

- Dual-modules with 2 read-out chips bump bonded on a sensor with a size of 2×4 cm^2.
- Quad-modules having 4 read-out chips bump bonded on a sensor with a size of 4×4 cm^2.

In the LoI, it is planned to use dual-modules for the innermost layers and quad-modules for the outermost layers The sensor types considered for the new pixel detector are Planar sensors, 3D sensors and Diamond sensors.

- Planar sensors (n-in-n and n-in-p) [27, 31, 32, 33]. They are well understood and exhibit good performance in the current tracking detectors. The construction of planar sensors has the advantage of relying on a long experience of high quality, low costs and high yield mass production. However, the planar sensors are very sensitive to radiation and require a high depletion voltage. Radiation damage[34] is easy to happen in planar sensors resulting in a short life time. The planar Research and Development (R&D) group is studying to extend the planar sensors' life time. Currently, due to the cost-effectiveness, they are planned to be used for large instrumented areas. N-in-n sensors are assumed to be used for the two innermost pixel layers based on test beam results. For the two outer layers, n-in-p planar sensors are assumed at the moment since they are cheaper and many suppliers exist.

- 3D sensors [28, 29]. For the new Pixel Detector, 3D sensors are alternatives to the planar sensors since they are more radiation resistant. They require a relatively low depletion voltage (200-300V) even after high irradiation doses, compared to planar sensors ($\backsim$1000V). However 3D sensors are more expensive. The 3D sensors are currently used in the IBL detector. A new generation of 3D sensors is under development for the upgrade of the ATLAS phase II.

- Diamond sensors [30]. Diamond detectors have lower capacitance and a better radiation hardness in terms of dark current. In principle they might not require cooling, while until now, all semi-conductor detectors use a cooling system. The diamond sensors are still expensive and in a phase of R&D.

The front-end readout electronics (FE) chips are the main contributors to the power consumption at start of the operation of the pixel detector while the sensor will have a significant contribution after severe radiation damage close to the end of the detector life time. The heat dissipated by both the FE electronics and the sensor at the end of its life time determine the cooling requirements. For IBL, a chip called FE-I4 is under use. However, it cannot be used for the upgrade of the pixel detector for HL-LHC due to the expected radiation and increased rate conditions. Researchers are working on new generation of pixel readout chips beyond FE-I4 on two parallel developments: 3D electronics integration and 65 nm size CMOS technology [35]. The 65 nm size CMOS technology is at least assumed as baseline for the ATLAS pixel detector for HL-LHC. The electrical signals from the modules are transmitted to the off-detector electronics via a cable path called "stave flex" which is tightly integrated with the stave in order to save space and material. One of the main challenges in the design of a stave flex is to provide a data transmission integrity along several meters with high speed (320 or up to 640 Mbps).

1.6 Upgrade of the pixel support

For each of the pixel layout design, a support structure equipped with an efficient cooling system is needed to maintain the module in place and to keep the temperature of the sensors and of the read-out elements within a safety range and uniform across the detector [36].It is required that the material of the support structure has a light weight, a good heat conduction, a small thermal expansion coefficient and that it is mechanically stable with respect to long

term operations[37]. Materials with long interaction length[38] (X_0[1]) are used to minimize the secondary interaction of the particles in the Pixel Detector allowing a better tracking and vertexing performance. Material with long X_0 are materials with low density.

According to the above requirements, carbon materials are in principle the best option. For example, the carbon foam [39] is a low density carbon material (down to a factor of 10 with respect to graphite) with still a relatively good thermal and mechanical property. The internal structure of this material is made of open cells with large surfaces. Therefore, it is widely used as main support part and as high thermally conductive heat sinks. In addition, the thermal and electrical conductivity of the foam can be adjusted according to the needs of a specific application. Another commonly used material is called carbon fiber[40]. It is made of extremely thin fibers that can be oriented in preferred directions for optimization of physical properties of the finished product. The carbon fiber has high thermal conductivity along the fiber direction, and low mass. The carbon fibers are mostly used in a material called "composite", a special synthetic resin, in which the carbon fibers are embedded. The stiffness of the composite is optimized by arranging the orientation of the fibers. In addition, fatigue and corrosion resistance are key benefits of carbon fiber composites.

The structure can be regarded as a thermal path, along which the thermal power is dissipated. It can be separated into a passive thermal conductance support path and an active control part, the cooling system. As illustrated in Figure 1.14, the heat load which originates from the sensors and the electronic chips passes through the support structure and reaches the cooling system, which consists in most of the cases in a pipe in which circulates a cooling fluid. The temperature on the sensors depends on the thermal performance of the entire thermal path. The concept of Thermal Figure of Merit ($TFoM$) is introduced to assess the thermal

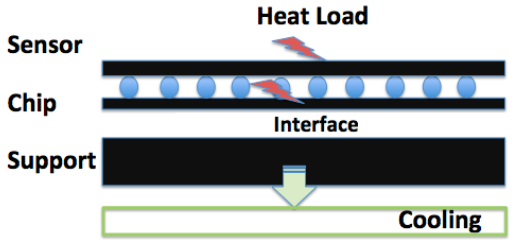

Figure 1.14: Illustration of the concept of a thermal path of a support structure.

performance of the thermal path. The $TFoM$ is defined as the temperature difference, ΔT, between the cooling fluid and the hottest point in the module divided by the total power density [2] generated by the sensor, read-out chip and module flex:

$$TFoM = \frac{\Delta T}{\dot{Q}/A_{sensor}} \tag{1.3}$$

The temperature on the sensor can be expressed as:

$$T_{sensor} = T_{fluid} + \frac{TFoM}{A_{sensor}} \times (\dot{Q}_{sensor} + \dot{Q}_{chip} + \dot{Q}_{flex}) \tag{1.4}$$

where $\dot{Q}_{sensor}$ is the generated power from the sensor; $\dot{Q}_{chip}$ is the chip generated power; $\dot{Q}_{flex}$ is the generated power from the module flex; A_{sensor} is the sensor active area corresponding to

[1]The radiation length is a characteristic of a material, related to the energy loss of high energy, electromagnetic-interacting particles. It is often expressed in $g \times cm^{-2}$

[2]The power density is the power per unit of surface

one chip; T_{fluid} is the temperature of the cooling fluid. A good design should have a low $TFoM$ with minimum material. This indicates a low thermal resistance across the entire thermal path, which finally prevents the thermal run-away [41, 42] from happening to the sensor.

A main concern in the silicon sensor is the phenomenon of "thermal run-away". It is related to the leakage current and silicon bulk damage. The leakage current in a semiconductor device is the current through that semiconductor device when the device is reverse biased. This current is due to thermally generated minority carriers that can not recombine under the electric field, including: diffusion current generated in the undepleted zone adjacent to the depletion zone; generation current originated in the depletion zone by defects or contaminants. Therefore, the leakage current is sensitive to the production process quality. The leakage current in a silicon sensor produce noise in the read-out and is therefore favorable to keep the leakage current as low as possible. In a harsh radiation environment, silicon sensor suffer from radiation damage. One of the gradual radiation damage seen in the silicon detector is increased leakage current, as the intrinsic charge carrier density increases with temperature. The leakage current also increases with the sensor temperature. The temperature dependence of the leakage current is expressed by the following equation:

$$I(T) = I(T_{ref}) \cdot (T/T_{ref})^2 \exp(-E_g/2k_B \cdot (1/T - 1/T_{ref})) \tag{1.5}$$

where T_{ref} is an arbitrarily chosen reference temperature, usually 273 K. E_g and k_B are the silicon band gap and Boltzmann constant, respectively. $I(T_{ref})$ is the leakage current under T_{ref}. As shown in equation 1.5, the leakage current is exponentially dependent on the temperature. When the leakage current is large, the heat generated by the leakage current leads to considerable increases of the temperature of the sensor, which in turns leads to an even larger leakage current. The self-heating and power contribution after radiation damage is becoming significant with respect to the FE chip contribution. Depending on the thermal dissipation this heat can be taken by the cooling system provided that the total heat flow is lower than the sensor self-heating. If not then it leads to unstable operation since it will permanently run way and over-heat.

The temperature of the sensor depends not only upon the support, but also the active cooling. Therefore an efficient cooling system is required to keep the temperature of the sensor under a certain threshold to avoid the thermal run-away.

1.7 Upgrade of the cooling system

Part of the cooling system of the detector, is deeply inserted into the detector volume, in particular the cooling pipe is housed in the local support structure, therefore, the mass of its material and of the cooling fluid are required to be as small as possible as well. An evaporative cooling system has been chosen for the Pixel Detector rather than a mono-phase cooling system. It makes use of the fact that a liquid (called refrigerant or coolant) absorbs heat when it evaporates. Evaporative cooling systems have a larger cooling capacity per unit of volume as result of utilizing the latent heat of vaporization rather than the specific heat capacity of a liquid. A smaller mass flow is therefore required. Evaporative two-phase cooling systems are characterized by their higher heat transfer coefficient (HTC) [3] between the cooling fluid and the local support structure, and a smaller temperature gradient along the cooling pipes which is favorable to avoid failure happening to the support structure due to thermal stress. The current cooling system of the Pixel Detector is similar to that of a standard industrial refrigerant plant,

[3]The heat transfer coefficient is a proportionality coefficient relating the heat flux and the temperature difference between the fluid and the wall flowed with the fluid.

using C_3F_8 [43, 44] while for the IBL detector carbon dioxide (CO_2). In view of the upgrade of the Inner Tracker, both for Pixel and Strip detectors, it is planned to use CO_2 only.

CO_2 has a high critical pressure [4] of 73.8 bar at 31 °C. The triple point [5] is at -56.5 °C at 5.1 bar (see Figure 1.15). CO_2 has more favorable convective and boiling characteristics due to its

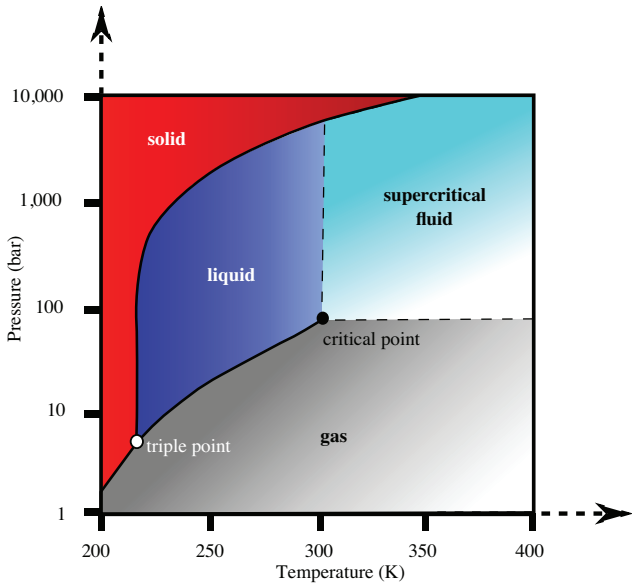

Figure 1.15: The pressure-temperature diagram of CO_2

high vapor density, low surface tension and low vapor viscosity. Thanks to its thermophysical properties, the *HTC* of CO_2 is greater than of conventional refrigerant by a factor between 2 and 3 at the same saturation temperature [45, 46, 47]. In order to have a better understanding of the differences of the thermophysical properties between a traditional coolant as C_3F_8 used for the present ID and the CO_2 fluid, a comparison of the thermophysical properties was done [48]. The properties of the fluids C_3F_8 and CO_2 are illustrated in the Figure 1.16. The upper left plot shows the latent heat of evaporation as function of the saturation temperature. At a given saturation temperature, such as -20°C the latent heat of CO_2 is at least two times higher than the one of C_3F_8, therefore CO_2 has higher cooling capacity. The upper right plot shows the viscosity as a function of the saturation temperature. This is one of the important parameters which determines the variation of the pressure (pressure drop) of the fluid along the cooling pipe due to the frictional force, caused by resistance to the flow. A low viscosity means a lower pressure drop, which in turn corresponds to a lower temperature drop assuring a better temperature uniformity across the detector. In addition to the latent heat and viscosity properties, the liquid to vapor density ratio of the cooling fluid is also important. Fluids with high liquid to vapor density ratios are unfavorable, since the vapor phase of the fluid moves much faster than the liquid phase of the fluid. High flow velocities induce considerable pressure drops which induces a large temperature variation along the cooling pipe.

In order to know if the use of the CO_2 as coolant will allow to build more efficient and less massive cooling systems compared to C_3F_8, a calculation [48] was done considering the pressure drop between the inlet and outlet of a cooling pipe as a function of the pipe diameter for the fluids CO_2 and C_3F_8 at a saturation temperature of -25 °C , with a heat input of 150 W and a ratio in mass of vapor to fluid at the exit of the cooling pipe of 40 %. The result is shown in

[4] The critical point is the end point of a phase equilibrium curve

[5] At the triple point, the three phases (gas, liquid and solid) of a substance coexist in thermodynamic equilibrium

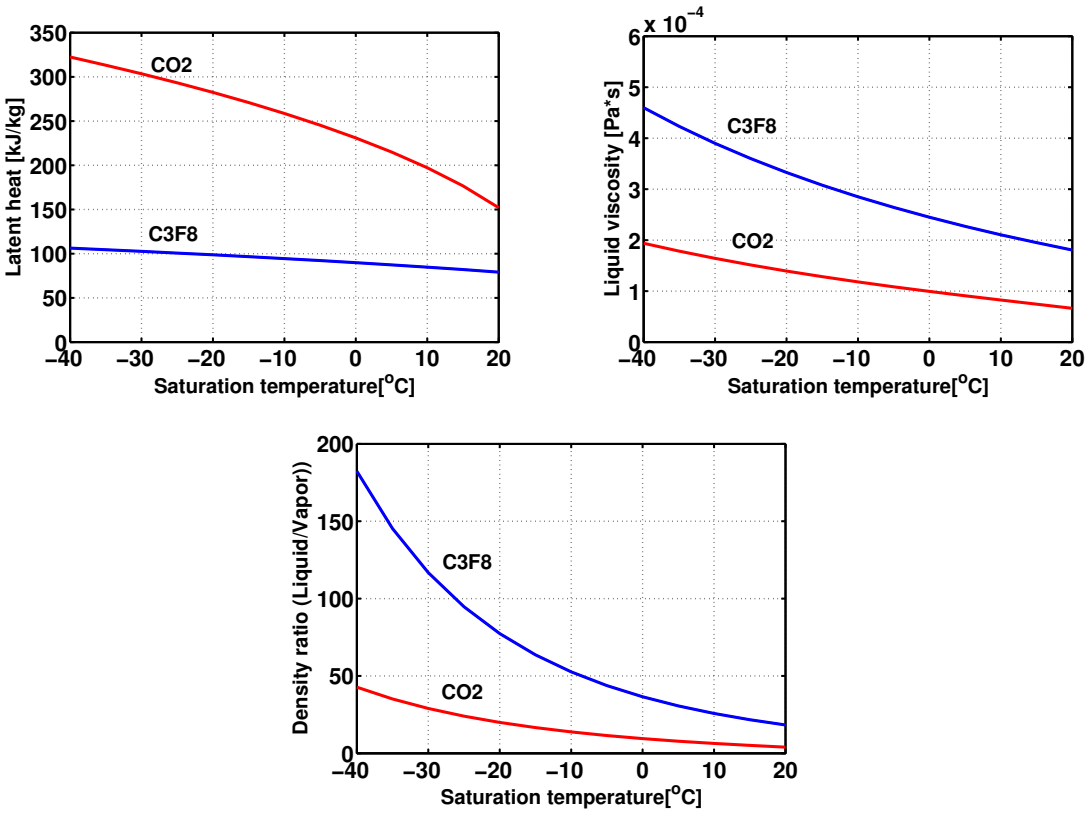

Figure 1.16: Latent heat of evaporation(top left), liquid viscosity(top right), liquid to vapor density ratio(bottom) as function of the saturation temperature for CO_2 and C_3F_8

Figure 1.17. It is found that to achieve the same pressure drop, for example 1 bar, the required diameter of the cooling pipe with CO_2 as cooling fluid is about 2.5 mm, while using C_3F_8 as the coolant, a pipe with an inner diameter of 4.5 mm is needed. This brings a larger amount of material and is not desirable, as explained in the previous Section. Using CO_2 will help reducing the amount of material contributing to the passive material budget.

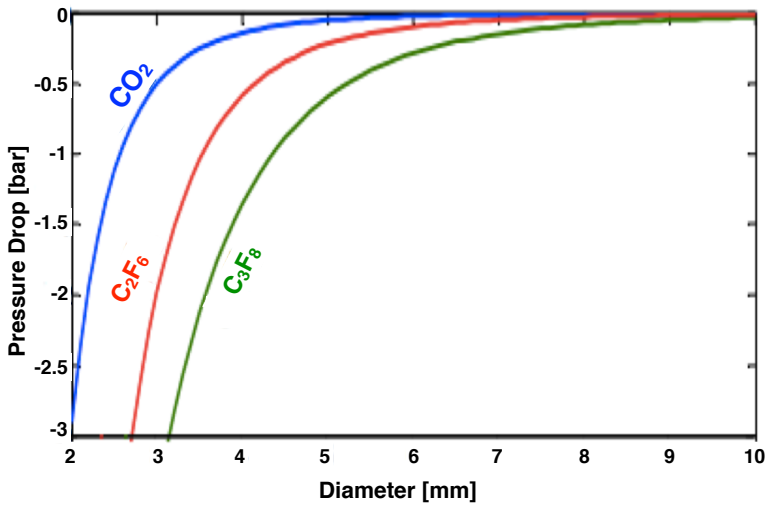

Figure 1.17: Pressure drop as a function of the tube diameter for CO_2, C_3F_8 and C_2F_6.The themodynamic properties of the fluids are specified in the text.

The first CO_2 two-phase cooling system for a particle physics experiment was used in the Silicon Tracker system of the Alpha Magnetic Spectrometer AMS-02 [49, 50]. AMS-02 is an astroparticle physics experiment operating successfully on the International Space Station since 2011. Based on the experience of this first CO_2 cooling system, the same criteria were also used for the detectors of the LHC. The VELO detector of LHCb as well as the IBL detector [51] uses the CO_2 evaporative cooling system [52, 53]. CO_2 two-phase cooling systems are gaining more and more interest in high energy physics experiments. The concept of cooling systems based on CO2 used in high energy detectors is the so-called Two-Phase Accumulated Controlled Loop (2PACL) [48, 54]. The system is divided into three distinct sections by locations. They are:

- The evaporator which is coupled with the detector and therefore is located in a non-accessible region. Inside this section, the initial part and final part of the transporting lines (outside the evaporator) are defined as the **Inlet tube** and **Outlet tube**.
- The cooling plant which is outside the detector in a free access area;
- The transfer lines between the evaporator and the cooling plant.

Figure 1.18 shows that the main components of a 2PACL cooling system. It includes a 2-Phase accumulator, a mechanical pump, a heat exchanger, an evaporator and a condenser. The accumulator is the key component of the cooling system and has two functions. The first

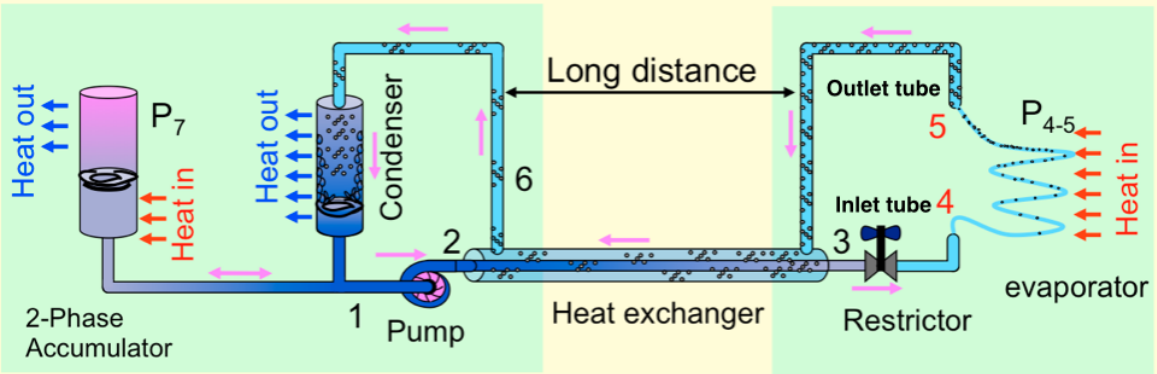

Figure 1.18: Illustration of a CO_2 cooling system.

function is to control the working temperature of the evaporator as explained in the following. The accumulator is partially filled with CO_2 in the state of two phases (liquid-vapor). The accumulator is controlled via heating or cooling to increase or decrease the temperature and therefore the pressure of the vapor-liquid mixture. The pressure drop in the return lines after the evaporator is low, therefore, the fluid pressure inside the accumulator is the same as in the evaporator with only a small offset. This gives the possibility to control and operate the evaporator over a wide range of temperature. The other function of the accumulator is to act as fluid reservoir: its volume must be adequate to supply CO_2 to the full cooling circuit or take in the surplus of CO_2 from full cooling circuit. For different applications, different accumulators should be specially designed.

In the high energy physics applications, the evaporator is a component which has a direct contact with the detector, therefore, it has to be designed in such a way that it remains compatible with the detector geometry. The material of the evaporator must be of low density in order to avoid extra particle interaction inside the detector, and has a small thermal expansion coefficient and a high thermal conductivity, as explained before.

The function of the heat exchanger is to exchange the heat between the evaporator return line and the line coming from the pump. The best and simple heat exchanger for a cooling

system is a concentric heat exchanger made of concentric pipes which allows heat exchanges between the fluid circulating in the internal and external pipe along the entire path of the transporting pipe. The liquid CO_2 flows in the internal pipe, the return two-phase CO_2 flows in the external pipe. The temperature of the liquid CO_2 which comes from the pump flows through the heat exchanger and increases up to the saturation value. A heat exchanger avoids the use of a pre-heating and therefore saves pre-heating power[48, 55].

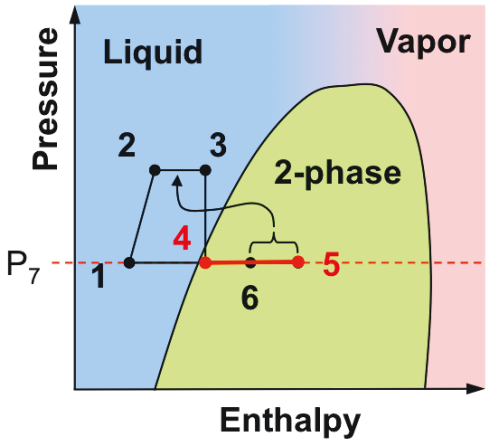

Figure 1.19: Operation cycle of a CO_2 cooling system illustrated in a pressure-enthalpy diagram

The thermodynamic processes occurring in a CO_2 cooling system are represented by a pressure-enthalpy diagram, shown in Figure 1.19:

- 1-2: A mechanical pump is used to increase the pressure of CO_2
- 2-3: The heat is exchanged, at constant pressure, between the CO_2 from the evaporator return lines and the CO_2 in the line coming from the pump
- 3-4: The pressure is lowered in order to reach the working temperature
- 4-5: The CO_2 collects the heat from the detector and evaporates
- 5-6: The heat is exchanged inside the heat exchanger
- 6-1: The CO_2 in two-phase state condenses inside the condenser.

1.8 Outline of thesis

This thesis focuses on the thermal optimization of the Alpine stave design, and addresses various design issues in order to reach a good preliminary understanding of the mechanical and thermal performance of the local support structure and of the CO_2 two-phase cooling system. This work will facilitate a final decision on the new Pixel Detector layout. In the following, Chapter 2 introduces the definitions of the terminologies of the two-phase heat transfer as well as models used for predicting the pressure drop and heat transfer coefficient of two-phase and mono-phase heat transfer. Chapter 3 details the logic of a numerical program used to facilitate the design of the CO_2 cooling system and its application example. Chapter 4 describes the process of designing the local support structure of the Alpine detector. The parameters related to the CO_2 cooling evaporator embedded inside the local support structure are also discussed. Chapter

5 presents the results of the measurements of two prototype: Proof-of-Concept prototype and Functional-Demonstration prototype. The first prototype is to prove the Alpine design, and the second one is to verify the thermal performance of the Alpine design using new materials and manufacture procedure. The measurements are compared with the predictions. Chapter 6 summarizes the thesis work.

Chapter 2

Theory of evaporative heat transfer

The ability to perform calculations and predictions of two-phase heat transfer phenomena is essential for designing and optimizing the cooling system for the upgrade of the ATLAS Inner Detector. In this section, we will review and summarize some aspects of the description of two-phase heat transfer inside a pipe. The basic principle and the definitions used to describe two-phase flow systems will be first reviewed in Section 2.1. The concept of non-dimensional numbers will be presented in Section 2.2. Based on the understanding of the main characteristics of the two-phase flow systems, the concept of flow pattern will be described in Section 2.3. In Sections 2.4, 2.5 and 2.6 the modeling of the thermal properties directly related to the cooling system design, such as pressure drop and heat transfer coefficient will be presented for two-phase and one phase fluid. The equations and the variables introduced in this part of the manuscript will be used extensively in the following chapter, where a numerical program, developed by the author of this thesis work, is described and is used for the simulation and the design of cooling systems.

2.1 Conservation principles and definitions

The numerical description of two-phase systems, flowing through a pipe, relies on the underlying concepts of the study of heat transfer, of thermodynamics and of fluid dynamics. In this Section, the main conservation equations and the definition or variables that will be used in this work are presented.

2.1.1 Conservation principles

Conservation of the mass

During an interval of time dt, the variation of the mass of a fluid in a control volume (dm_{cv}) is equal to the difference between the mass entering into the volume and the mass flowing out per unit of time:

$$\frac{dm_{cv}}{dt} = \dot{m}_{out} - \dot{m}_{in} \tag{2.1}$$

For a steady-state flow, the equation 2.1 is simplified into,

$$\dot{m}_{in} - \dot{m}_{out} = 0 \tag{2.2}$$

This relation expresses the continuity equation in fluid dynamics.

Conservation of energy

The fist law of thermodynamics applied to a steady-state flow of a fluid [56] expresses an energy conservation principle and can be formulated as:

$$\Sigma\dot{m}_{out}(h_{out} + \frac{\upsilon_{out}^2}{2} + gZ_{out}) - \Sigma\dot{m}_{in}(h_{in} + \frac{\upsilon_{in}^2}{2} + gZ_{in}) = \dot{W} + \dot{Q} \tag{2.3}$$

where h, υ and Z are the specific enthalpy, the velocity and the height of the fluid respectively. $\dot{Q}$ and $\dot{W}$ are the heat and the work per unit of time exchanged between the fluid and the outside.

2.1.2 Definitions

In this Section, the variables used to describe the heat transfer during the flow of a fluid in a two-phase state are defined.

Flow rate

The total mass flow rate ($\dot{m}$) is the sum of the mass flow rate of the liquid phase ($\dot{m}_L$) and the mass flow rate of the vapor phase ($\dot{m}_V$) of the fluid.

$$\dot{m} = \dot{m}_L + \dot{m}_V \tag{2.4}$$

The volumetric flow rate ($\dot{V}$) is the sum of the volumetric flow rate of the liquid phase ($\dot{V}_L$) and the volumetric flow rate of the gas phase ($\dot{V}_V$) of the fluid.

$$\dot{V} = \dot{V}_L + \dot{V}_V \tag{2.5}$$

The volumetric flow rate is related to the mass flow rate by the following expression:

$$\rho \equiv \frac{\dot{m}}{\dot{V}} \tag{2.6}$$

where ρ is an "effective" density of the fluid under consideration at a given temperature and pressure.

Vapor quality

The vapor quality (x) is the ratio of the vapor mass flow rate divided by the total mass flow rate.

$$x = \frac{\dot{m}_V}{\dot{m}} \tag{2.7}$$

The vapor quality is directly related to the thermal properties of the fluid, as it will be explained in detail later. However it is difficult to measure with precision the vapor quality of a liquid-vapor mixture flowing in a pipe during the change of phase. Moreover, when there is no thermal equilibrium between the two phases, the vapor quality can not be determined simply from the inlet vapor quality and the heat flux through the wall of the pipe.

A theoretical vapor quality, the so called "vapor quality from the thermodynamic equation" can be calculated by assuming that both phases are at the saturation temperature and pressure. It can be calculated as:

$$x = \frac{h_z - h_L}{h_{LV}} \tag{2.8}$$

where h_z is the specific enthalpy of the fluid at a given position z along the flow direction, h_L is the specific enthalpy of the saturated liquid and h_{LV} is the latent heat of vaporization.

Void fraction

In a two-phase flow, the void fraction (ϵ) is defined as the ratio of the volume occupied by the vapor (V_V) and the total volume (V) of the vapor-liquid phases.

$$\epsilon = \frac{V_V}{V} \tag{2.9}$$

The void fraction also represents the cross-section area occupied by vapor phase.

Mass velocity

The mass velocity (G) is defined as the ratio of the mass flow rate divided by the transverse area of the pipe A:

$$G = \frac{\dot{m}}{A} \tag{2.10}$$

Average flow velocity

Applying the conservation of the mass, the mass velocity G, can be expressed as the average flow velocity multiplied by the density. It follows that the average flow velocity of the vapor (u_V) and of the liquid state (u_L) can be expressed as :

$$u_V = \frac{Gx}{\rho_V \epsilon} \tag{2.11}$$

$$u_L = \frac{G(1-x)}{\rho_L(1-\epsilon)} \tag{2.12}$$

2.2 Non-dimensional numbers

Non-dimensional numbers are quantities without an associated physical dimension. They are widely used in many fields such as mathematics, physics, engineering and in the analysis of mass and heat transfer systems. Several non-dimensional numbers are introduced in order to describe the fluid dynamics of mono-phase and two phase-flow phenomena. They are useful in deducing basic relations among system variables that are valid for a wide ranges of fluids under different configurations. The most commonly used numbers are discuss in this Section.

Reynolds number

The Reynolds number(Re) represents the ratio of the inertial forces to the viscous forces acting on a fluid. For the particular case of forced convection inside a tube, the Reynolds number of a liquid flowing in a pipe is expressed as:

$$Re_L = \frac{\rho_L u_L D_h}{\mu_L} \tag{2.13}$$

where u_L and μ_L are respectively the flow velocity and the viscosity of the fluid in the liquid state. D_h is the hydraulic diameter defined as the ratio of the transverse area of the pipe and P_L is the wetted perimeter.

$$D_h = \frac{4A}{P_L} \tag{2.14}$$

If the cooling channel is a pipe with a circular shape transverse to the flow direction and the fluid is in liquid state, then the hydraulic diameter equals to the tube diameter.

Prandtl number

The Prandtl number (Pr) represents the ratio of the momentum diffusivity to the thermal diffusivity of the fluid. For a liquid, it is expressed as:

$$Pr_L = \frac{C_{PL}\mu_L}{k_L} \tag{2.15}$$

where C_{PL} and k_L are respectively the thermal capacity and the thermal conductivity of the fluid in the liquid state. For vapors, the Prandtl number is expressed in a similar way using the corresponding vapor properties (C_{PV}, μ_V and k_V).

Nusselt number

The Nusselt number (Nu) expresses the ratio of convection to conduction temperature gradient within a fluid under the same heat flux. Under internal forced convection for a single phase and two-phase fluid in a tube, the Nusselt number is defined as:

$$Nu = \frac{hD_c}{k} \tag{2.16}$$

where h is the heat transfer coefficient of the fluid, D_c is a characteristic length that can be taken as the tube diameter and k is the thermal conductivity of the fluid.

Liquid Weber number

The Weber number (We) is useful when analyzing flow processes with an interface[1]. For two-phase flow, it expresses the ratio of inertial forces acting on the fluid to surface tension forces σ. The liquid Weber number is expressed as:

$$We_L = \frac{\rho_L u_L^2 D_c}{\sigma} \tag{2.17}$$

The reference length (D_c) for a liquid in a circular pipe can be taken as the tube diameter. For two-phase heat transfer, the We depends on details of the particular model description.

Froude number

The Froude number (F_R) represents the ratio of the inertial forces to the gravitational forces acting on the fluid, and it is expressed by:

$$F_R = \frac{u}{\sqrt{gL}} \tag{2.18}$$

u is a characteristic flow velocity, g is the acceleration of gravity, and L is a characteristic length.

For two-phase heat transfer, the F_R depends on the specific model as will be discussed later.

[1]The interface is between two different phases or between two different fluids

2.3 Flow pattern

A fluid in a two-phase state of liquid and vapor, flowing through a pipe, is characterized by a flow pattern or flow regime, which represents the way in which the flow of the fluid takes place. Different flow patterns result in different mechanisms of mass and heat transfer. The calculations of pressure drop and the heat transfer coefficient are closely related to the local flow pattern of the fluid, and thus the flow pattern is an important aspect for the modeling of the evaporation process.

2.3.1 Flow patterns in horizontal flows

The two-phase flow pattern have been studied extensively in literature. In the following, the flow pattern inside a horizontal pipe will be introduced.

The flow patterns of a vapor and a liquid in a horizontal tube are strongly influenced by the gravity force which try to separate the liquid to the bottom of the tube and the vapor to the top. The liquid and vapor phases distribute themselves into several recognizable flow structures. Several distinct flow patterns exists in the two-phase flow. There are different ways to name the flow patterns. A common way is the following: bubbly flow, stratified flow, stratified-wavy flow, intermittent flow, annular flow, dry-out and mist flow(see Figure 2.1).

- Bubbly flow. When the mass flow rate is high and the vapor quality is low, the bubbles are dispersed uniformly with an higher concentration of bubbles in the upper half of the tube due to the buoyancy. In this case, the shear forces are dominant and the bubbles tend to disperse uniformly.

- Stratified flow. When the average flow velocities of the liquid and of the gas is low, the two phases are completely separated, namely the vapor goes to the top and the liquid to the bottom of the tube. The two phases are separated by an undisturbed flat interface. Since the liquid and vapor are stratified in this regime, this pattern is called stratified flow.

- Stratified-wavy flow. In a stratified flow, waves propagate along the interface between the liquid and vapor. This happens when the average flow velocity of vapor is increased along the direction of the flow. The amplitude of the waves is noticeable but does not touch the top of the tube. A fine layer of liquid film is presented in the lower part of the tube.

- Intermittent flow. The intermittent flow happens at low vapor quality with the tube wall fully wet with liquid. In this regime, waves of large amplitude touch the top of the tube, and bubbles are present. Intermittent flow can be regarded as the combination of the plug and slug flow regimes.

  - Plug flow. This regime has liquid "plugs" separated by elongated bubbles, of transverse diameters much smaller than the tube diameter. The liquid phase is continuous below the bubbles.
  - Slug flow. When the vapor quality is high, the transverse diameters of elongated bubbles have almost the same dimension as the diameter of the tube.

- Annular flow. The annular flow is the ideal flow regime for a two-phase heat transfer, and is characterized by a continuous film formed on the wall of the tube. The vapor tends to remain in the center. Due to gravity and buoyancy effects, the liquid film is thicker at the bottom than at the top of the tube.

- Dry-out flow. In the dry-out regime, differently with respect to the regimes described above, the pipe surface is no longer in direct contact with the liquid, but with the vapor. This results in a sharp decrease of the heat transfer coefficient and is the point that in the design of cooling systems should be avoided, since the cooling capabilities of the fluids are greatly reduced [57].
- Mist flow. The mist flow occurs when the whole liquid film dries out, and only a very small amount of droplets are trapped within the vapor. Compared to the dry-out flow, mist flow has worse ability of heat transfer.

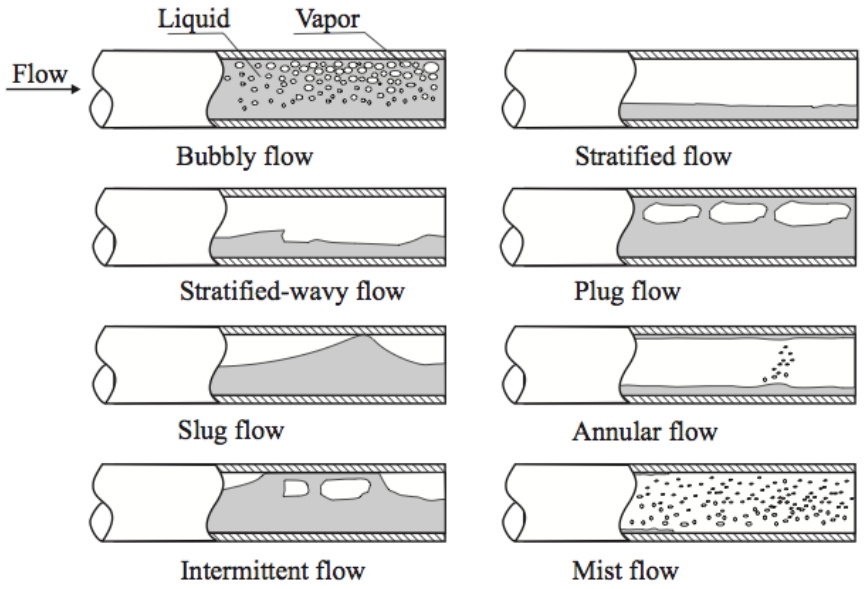

Figure 2.1: Flow patterns during evaporation in horizontal flow [58]

Figure 2.2 is a schematic representation of a horizontal pipe heated by a uniform heat flux, showing the flow patterns of a fluid in a two-phase state flowing along the pipe.

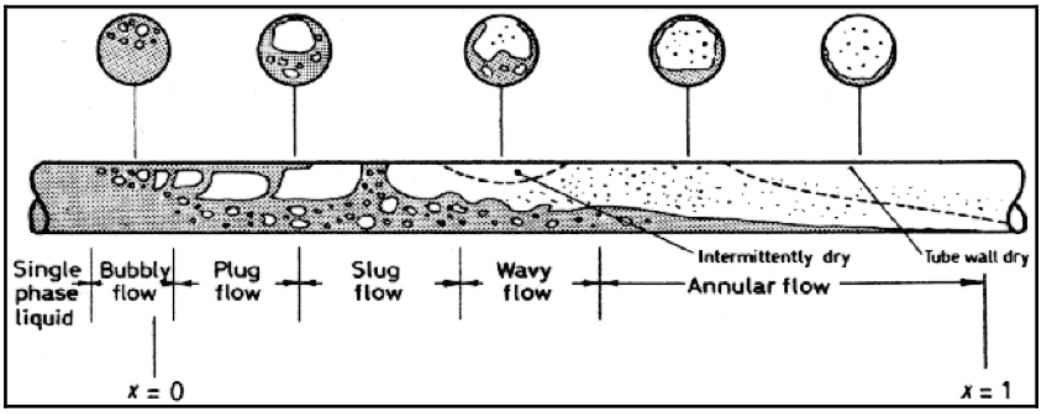

Figure 2.2: Flow patterns during the evaporation process in a horizontal tube [58]

2.3.2 Flow-pattern map

In order to model the heat transfer process of a two-phase flow inside a pipe, it is necessary to establish a reliable flow pattern map. Flow pattern maps are represented as areas on a map

separated by transition lines. The variables reported on a flow-pattern map can be the average gas versus the liquid flow velocities or generalized variables containing these velocities. A good flow-pattern map helps to choose the best working range in order to fully deploy the cooling capacities of the fluids and avoid the dry-out and mist flow regimes.

The first person who recognized the importance of the flow-pattern map as a starting point for the calculation of the heat and mass transfer was Baker [58]. The Baker map was not considering the heat exchange during the evaporation processes. Later on, Taitel and Dukler[58] and Taitel [58] developed comprehensive methods to predict the transitions between flow patterns. However, these maps were for adiabatic [2] processes during evaporation, and could not be used to describe the evaporation processes for cooling process. It is desirable to define a flow-pattern map that includes the influences of the heat exchange. Kattan et al. [59] developed a diabatic two-phase flow pattern map based on the works of Taitel and Dukler and Steiner. The Kattan flow pattern map indicates the characteristic of the flow process in a diagram of the mass velocity (G) as a function of vapor quality(x), given the fluid properties, the pipe diameter (D) and the heat flux (q) across the pipe wall. This map includes five flow regimes, stratified flow

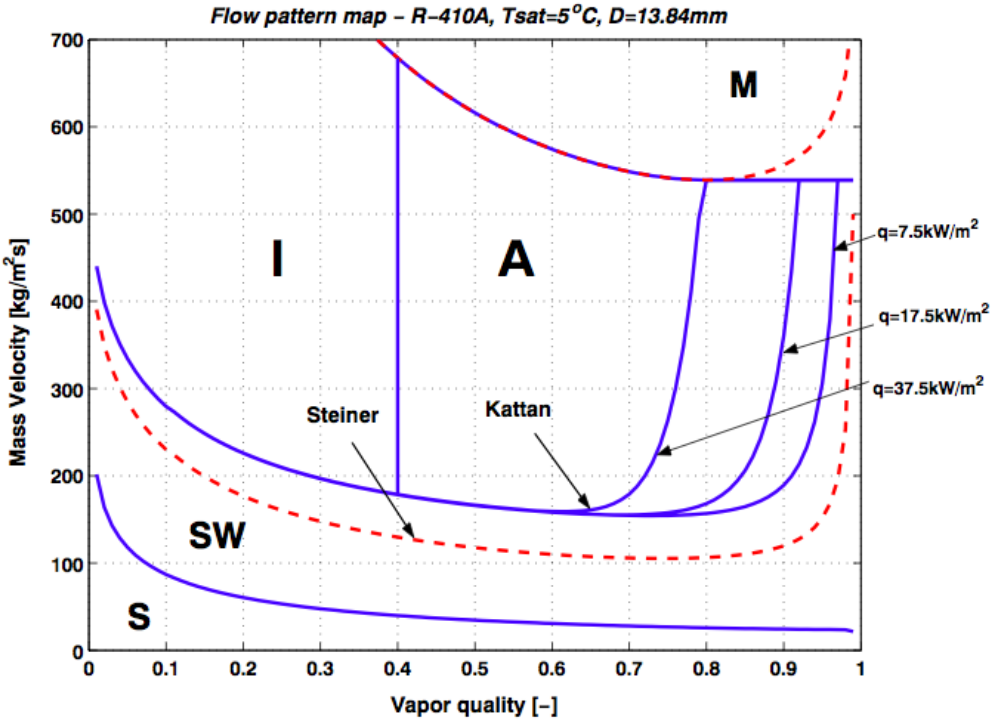

Figure 2.3: Kattan (1998) flow pattern map (solid lines) evaluated for refrigerant R-410A at Tsat = 5 °C in 13.84 mm internal diameter tube. The Steiner flow-pattern map is also shown (red dashed line). The letters **S**, **SW**, **I**, **A** and **M** indicate stratified, stratified-wave, intermittent, annular and mist flow, respectively[59].

(**S**), stratified-wave flow (**SW**), intermittent flow (**I**), annular flow (**A**) and mist flow (**M**). A method to predict the onset of dry-out in evaporating annular flow is included in this model, i.e. the transition of annular flow into annular flow with partial dry-out. The latter is classified as stratified-wavy flow on the map. One example of Kattan flow pattern map is shown in Figure 2.3 for the refrigerant R-410A, at the evaporation temperature of 5 °C for a pipe with an inner tube diameter of 13.84 mm. The boundaries between each flow regimes are shown. Three heat

[2] An adiabatic process is a process with no heat exchange

fluxes are considered, 7.5 kw/m^2, 17.5 kw/m^2 and 37.5 kw/m^2, respectively. The region where the blue curves increase at high vapor quality indicate the onset of dry-out. It is seen that at higher heat flux the dry-out phenomenon occurs earlier during the evaporation process.

The flow pattern map for many traditional refrigerants were gradually developed, but, none of them is applicable to CO_2, since the use of this fluid is characterized by high reduced pressure[3] and low surface tensions. To fill this void, a new CO_2 flow pattern map, the **Cheng-Ribatski-Wojtan-Thome(CRWT)** CO_2 flow-pattern map[60] was developed and compared with experimental data (see Figure 2.4). Compared to the previous flow pattern maps, this new map includes the transition from dry-out flow to mist flow and the transition from intermittent flow and bubble flow.

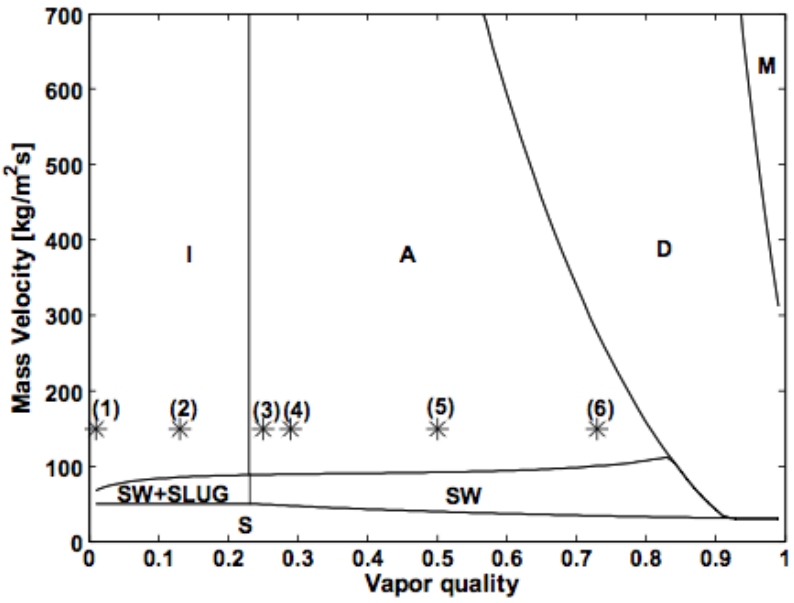

Figure 2.4: Cheng-Ribatski-Wojtan-Thome CO_2 flow-pattern map with experimental data superposed (stars)[60].

The **CRWT** map is going to be used for the design of the cooling system of the Alpine Pixel Detector, therefore, it is briefly described in the following. The mathematical relations expressing the equations of the boundary between regimes are given. They are used in the simulation program developed by the author of this thesis described in Chapter 3. Figure 2.5 illustrates the stratified flow pattern inside a horizontal circular tube. The **CRWT** model was developed based on this figure. For a circular tube, the tube diameter (D) is taken as the reference length; in the other cases, an equivalent diameter D_{eq} is used:

$$D_{eq} = [\frac{4A}{\pi}]^{1/2} \tag{2.19}$$

where A is the area of the transverse section of the pipe. Six dimensionless geometrical parameters are defined and will be used in the following to express the boundaries between flow regimes:

$$P_{LD} = \frac{P_L}{D_{eq}} \tag{2.20}$$

$$P_{VD} = \frac{P_V}{D_{eq}} \tag{2.21}$$

[3]The reduced pressure of a liquid is defined as its actual pressure divided by its pressure at the critical point

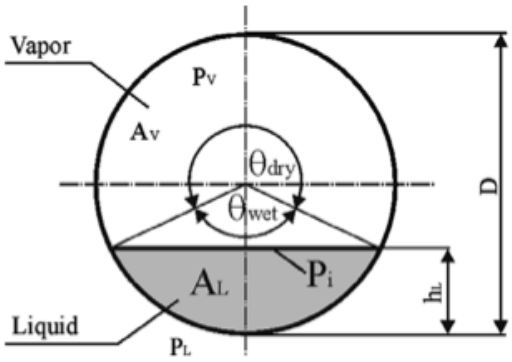

Figure 2.5: Schematic diagram of a stratified two-phase flow in a horizontal tube[60].

$$A_{LD} = \frac{A_L}{D_{eq}^2} \tag{2.22}$$

$$A_{VD} = \frac{A_V}{D_{eq}^2} \tag{2.23}$$

$$h_{LD} = \frac{h_L}{D_{eq}} \tag{2.24}$$

$$P_{iD} = \frac{P_i}{D_{eq}} \tag{2.25}$$

P_L and P_V are respectively the wetted and dry perimeter for the liquid and the vapor, A_L and A_V are the cross sectional areas of the region occupied by the liquid and vapor, Pi is the length of the interface between the liquid and the vapor, and h_L is the height of the liquid phase from the bottom of the tube (see Figure 2.5). The dimensionless geometrical parameters A_{LD}, A_{VD}, h_{LD} and P_{iD} are calculated from the following relations:

$$A_{LD} = \frac{A(1-\epsilon)}{D_{eq}^2} \tag{2.26}$$

$$A_{VD} = \frac{A\epsilon}{D_{eq}^2} \tag{2.27}$$

$$h_{LD} = 0.5[1 - \cos(\frac{2\pi - \theta_{strat}}{2})] \tag{2.28}$$

$$P_{iD} = \sin(\frac{2\pi - \theta_{strat}}{2}) \tag{2.29}$$

where ϵ and θ_{strat} are the void fraction and the stratified angle, respectively. ϵ is determined with the Rouhani−Axelsson drift flux model [61], since this procedure avoids iterative calculations.

$$\epsilon = \frac{x}{\rho_V}[(1 + 0.12(1-x))(\frac{x}{\rho_V} + \frac{1-x}{\rho_L}) + \frac{1.18(1-x)[g\sigma(\rho_L - \rho_V)]^{1/4}}{G\rho_L^{1/2}}]^{-1} \tag{2.30}$$

The stratified angle θ_{strat} is a parameter calculated with the following expression:

$$\theta_{strat} = 2\pi - 2\{\pi(1-\epsilon) + (\frac{3\pi}{2})^{1/3}[1-2(1-\epsilon)+(1-\epsilon)^{1/3}-\epsilon^{1/3}] - \frac{1}{200}(1-\epsilon)\epsilon[1-2(1-\epsilon)][1+4(1-\epsilon)^2+\epsilon^2] \tag{2.31}$$

An important feature in a flow pattern map are the transition lines between flow regimes. To give a taste of the complexity of the calculation, the main analytic expressions used to calculate the boundaries between flow regimes are given explicitly here. They express the mass velocity as function of the vapor quality.

- The transition curve from stratified flow to stratified-wavy flow (**S-SW**) is calculated from the relation:

$$G_{strat} = [\frac{226.3^2 A_{LD} A_{VD}^2 \rho_V (\rho_L - \rho_V) \mu_L g}{x^2 (1-x) \pi^3}]^{1/3} \tag{2.32}$$

- The boundary between stratified-wave and intermittent flow (**SW-I**) or between stratified-wave and annular flow (**SW-A**) is calculated from the expression:

$$G_{wavy} = \{\frac{16 A_{VD}^3 g D_{eq} \rho_L \rho_V}{x^2 \pi^2 [1-(2h_{LD}-1)^2]^{1/2}} [\frac{\pi^2}{25 h_{LD}^2} \frac{F_{RL}}{We_L} + 1]\}^{1/2} + 50 \tag{2.33}$$

  where We_L and F_{RL} are the Weber and Froude number for liquids, obtained using the mass velocity (G) according to the expression:

$$F_{RL} = \frac{G^2}{\rho_L^2 g D_{eq}} \tag{2.34}$$

$$We_L = \frac{G^2 D_{eq}}{\rho_h \sigma} \tag{2.35}$$

- The vapor quality x_{IA} at the boundary between the intermittent and the annular flow (**I-A**) is calculated from the expression:

$$x_{IA} = [1.8^{1/0.875} (\frac{\rho_V}{\rho_L})^{-1/1.75} (\frac{\mu_L}{\mu_V})^{-1/7} + 1]^{-1} \tag{2.36}$$

  This boundary is extended down to its intersection with G_{strat} (see Figure 2.4).

- The boundary between the annular and the dry-out flow (**A-D**) is calculated from the relation:

$$G_{dryout} = \{\frac{1}{0.236} [\ln \frac{0.58}{x} + 0.52] (\frac{D_{eq}}{\rho_V \sigma})^{-0.17} [\frac{1}{g D_{eq} \rho_V (\rho_L - \rho_V)}]^{-0.17} (\frac{\rho_V}{\rho_L})^{-0.25} (\frac{q}{q_{crit}})^{-0.27}\}^{1.471} \tag{2.37}$$

  All the variables of this relation have been previously defined and q_{crit} is the critical heat flux when the dry-out happens. The application of heat fluxes above this value produces the dry-out phenomenon. The critical heat flux is calculated from the relation A.9 in the Appendix. Beyond the q_{crit}, the heat transfer coefficient falls drastically and the temperature of the tube wall increases abruptly.

- The transition from the dry-out to the mist flow (**D-M**) is calculated from the relation:

$$G_M = \{\frac{1}{0.502} [\ln \frac{0.61}{x} + 0.57] (\frac{D_{eq}}{\rho_V \sigma})^{-0.16} [\frac{1}{g D_{eq} \rho_V (\rho_L - \rho_V)}]^{-0.15} (\frac{\rho_V}{\rho_L})^{0.09} (\frac{q}{q_{crit}})^{-0.72}\}^{1.613} \tag{2.38}$$

  In the **CRWT** model, one new flow regime called "bubble flow" is introduced.

- The boundary from the intermittent to the bubbly flow (**I-B**, not shown in Figure 2.4) is calculated from:

$$G_B = \{\frac{256 A_{VD} A_{LD}^2 D_{eq}^{1.25} \rho_L (\rho_L - \rho_V) g}{0.3164(1-x)^{1.75} \pi^2 P_{iD} \mu_L^{0.25}}\}^{1/1.75} \tag{2.39}$$

Based on the above relations expressing the transition lines between different flow regimes, a CO_2 flow map like Figure 2.4 can be drawn for subsequent use.

2.4 Pressure drop

The pressure drop of a fluid flowing through a tube is the difference in absolute pressure between two points along the tube. It directly influences the thermal properties of the liquid and hence the working temperature of the cooling system. The total pressure drop of a fluid in a tube is the sum of three contributions. The first is due to the variation of the potential energy of the fluid (ΔP_{static}), the second contribution depends on the variation of the kinetic energy of the fluid (ΔP_{mon}) and the third contribution is related to the friction of the fluid on the pipe wall (ΔP_f). The flow pattern has an effect on the last contribution. The total pressure drop ΔP_{total} is expressed as:

$$\Delta P_{total} = \Delta P_{static} + \Delta P_{mon} + \Delta P_f \tag{2.40}$$

For a horizontal tube, there is no change in altitude, therefore, ΔP_{static} is equal to zero. The momentum pressure drop between two points ("in" and "out") of a pipe, related to the change in kinetic energy of the fluid, is given by equation A.1. It is hard to predict accurately the two-phase frictional pressure drop ΔP_f as the flow pattern of a liquid-vapor mixture is highly non-uniform [62]. Many calculation relying on different models have been carried out [63, 64]. They are all based on the observation of **semi-empirical** correlations, targeting different low reduced pressure refrigerant flowing mainly in macro-channel tubes. The **phenomenological** method [65, 66] was developed based on flow-pattern maps, and was shown to provide useful and more accurate predictions of ΔP_f.

2.4.1 The semi-empirical method

The semi-empirical method is commonly employed to model the pressure drop for a two-phase refrigerant resulting from the friction of the fluid on the tube wall. It makes use of sets of experimental measurements collected in a database. The method is easy to implement but provides a good accuracy only in a certain range of values of pressure drops. A disadvantage of this method is that no single relation is able to provide an acceptable accuracy for the full range of thermodynamic parameters in a two-phase heat transfer.

One of the most accurate two-phase pressure drop correlations[4] is from Friedel [67]. It was obtained by fitting an equation using a large database of two-phase pressure drop measurements. The Friedel correlation is applicable to vertical upflow and to horizontal flow. It covers vapor qualities between $0 \leq x \leq 1$ and utilizes a so called "two-phase multiplier", ϕ_{fo}^2:

$$\Delta P_f = \Delta P_{LO} \phi_{fo}^2 \tag{2.41}$$

where ΔP_{LO} indicates the pressure drop for a liquid state which is given by the expression:

$$\Delta P_{LO} = 4 f_{LO} \frac{L}{D_{eq}} G^2 (\frac{1}{2\rho_L}) \tag{2.42}$$

[4]The term correlation is employed to indicate the correlation of the pressure between two points of the fluid

where L is the length of the cooling pipe, and D_{eq}, ρ_L and G have been previously introduced. The friction factor f_{LO} is expressed for a turbulent flow as:

$$f_{LO} = \frac{0.079}{Re_{LO}^{0.25}} \tag{2.43}$$

The Reynolds number Re_{LO} for a liquid is expressed using the mass velocity (G) as:

$$Re_{LO} = \frac{GD_{eq}}{\mu_L} \tag{2.44}$$

The two-phase multiplier ϕ_{fo}^2 is expressed by an empirical relation:

$$\phi_{fo}^2 = E + \frac{3.24FH}{F_{RH}^{0.045} We_L^{0.035}} \tag{2.45}$$

F_{RH} is the Froude number calculated with equation 2.34 using the homogeneous density of the fluid, ρ_H, defined by equation A.2 in Appendix. A homogeneous fluid is a convenient concept for modeling two-phase pressure drops. It is a pseudo fluid that obeys the equations for single-phase fluids and is characterized by suitably averaged properties of the liquid and vapor phase. In equation 2.45, We_L is the Weber number in liquid state and the parameters E, F and H are defined in the appendix by equations from A.3 to A.5.

Friedel model will be used to describe the ΔP_f for vertical fluid flow in the next Chapter where a numerical program is developed to facilitate the cooling system design.

2.4.2 The phenomenological method

Phenomenological models [68, 69] of the pressure drop for a fluid in a two-phase state are "more theoretical" methods. In these models, the interfacial structure between the liquid and vapor phase (namely the different flow regimes) is taken into account, which results in models that can be applied in more general cases. Despite this obvious advantage, an important drawback of this approach is that some empiricism is still required in order to obtain, ΔP_f. Another important aspect to point out is that no general flow pattern based model is yet available. In practice, the predictions are only available for particular fluids. This observation preludes one of the major difficulty in following this approach: namely this approach needs a very reliable flow- pattern map in order to give reliable predictions.

A new two-phase frictional pressure drop model for CO_2 based on a flow pattern map was made by Thome [60, 70] by modifying the model of Moreno and Thome developed for the coolants of R-22, R-410a and R-134a. It incorporates updated flow pattern map, using a published pressure drop database and is a phenomenological two-phase frictional pressure drop model. This model is valid for tube diameter between 0.8 mm and 10 mm and will be used in the next Chapter to describe ΔP_f for horizontal flow. The different analytic expressions of ΔP_f for different flow patterns are presented here.

- The frictional pressure drop in the case of an annular flow (**A**) is given by:

$$\Delta P_A = 4 f_A \frac{L}{D_{eq}} \frac{\rho_V u_V^2}{2} \tag{2.46}$$

  where f_A is a two-phase flow friction factor for the annular flow given by:

$$f_A = 3.128 Re_V^{-0.454} We_L^{-0.0308} \tag{2.47}$$

  The average velocity of the vapor phase u_V is calculated using equation 2.11. Re_V and We_L are respectively the Reynolds number and Weber number for the vapor and liquid phase.

- The frictional pressure drop for an intermittent (**I**) flow is given by:

$$\Delta P_{SLUG+I} = \Delta P_{LO}(1 - \frac{\epsilon}{\epsilon_{IA}}) + \Delta P_A \frac{\epsilon}{\epsilon_{IA}} \tag{2.48}$$

  ΔP_A is calculated from equation 2.46 and ΔP_{LO} uses equation 2.42. This term ϵ is calculated by equation 2.30. The term ϵ_{IA} is the void fraction at the vapor quality x_{IA}, which is calculated with equation 2.36.

- The frictional pressure drop of a stratified-wavy flow (**SW**) uses the same expression as the one used for annular flow (equation 2.46), with a different two-phase friction factor f_{SW},

$$f_{SW} = (\theta^*_{dry})^{0.02} f_V + (1 - \theta^*_{dry})^{0.02} f_A \tag{2.49}$$

  The factor f_{SW} is a combination of liquid and vapor friction factor f_A and f_V. The parameter θ^*_{dry} is the normalized dry angle and is expressed as:

$$\theta^*_{dry} = \frac{\theta_{dry}}{2\pi} \tag{2.50}$$

  where θ_{dry} is expressed by:

$$\theta_{dry} = \theta_{strat}(\frac{G_{wavy} - G}{G_{wavy} - G_{strat}})^{0.61} \tag{2.51}$$

  and G_{wavy}, G_{strat} are the boundary mass velocity expressed by equations 2.33 and 2.32.

  The single-phase friction factor of the vapor phase f_V is calculated using equation 2.43 using vapor properties.

- The friction pressure drop for a slug-stratified wave flow (**SW+SLUG**) is a combination of the single liquid phase pressure drop (ΔP_{LO}) and the stratified wave flow(ΔP_{SW}):

$$\Delta P_{SLUG+SW} = \Delta P_{LO}(1 - \frac{\epsilon}{\epsilon_{IA}}) + \Delta P_{SW}(\frac{\epsilon}{\epsilon_{IA}}) \tag{2.52}$$

- The pressure drop for the mist flow (**M**) regime is calculated from the relation:

$$\Delta P_M = 4 f_M \frac{L}{D_{eq}} \frac{G^2}{2\rho_H} \tag{2.53}$$

  where f_M is defined by:

$$f_M = \frac{91.2}{Re_M^{0.832}} \tag{2.54}$$

  The Reynolds number Re_M is calculated using equation 2.44 with the homogeneous dynamic viscosity (μ_H) defined by equation A.6.

- The frictional pressure drop for the dry-out flow (**D**) is given by:

$$\Delta P_{dryout} = \Delta P_{tp}(x_{di}) - \frac{x - x_{di}}{x_{de} - x_{di}}[\Delta P_{tp}(x_{di}) - \Delta P_M(x_{de})] \tag{2.55}$$

  where x_{di} and x_{de} are the vapor quality when the dry-out regime starts [71, 72] and ends, respectively. They are also called "incipient vapor quality"(x_{di}) and "completion vapor quality" (x_{de}). $\Delta P_{tp}(x_{di})$ is the frictional pressure drop, calculated with equation 2.46 at the vapor quality of x_{di} and $\Delta P_M(x_{de})$ is the frictional pressure drop, calculated as in the case of stratified wavy flow at a vapor quality of x_{de}. Detailed equations of x_{di} and x_{de} are given in the Appendix by A.7 and A.8.

- For the calculation of the frictional pressure drop in a stratified flow (**S**), two zones are considered. The first zone is defined by: $x \geqslant x_{IA}$ (see Figure 2.4). In this case $\Delta P_{strat(x \geqslant x_{IA})}$ is calculated using equation 2.46 with a new two phase multiplier.

$$\Delta P_{strat(x \geqslant x_{IA})} = 4 f_{strat(x \geqslant x_{IA})} \frac{L}{D_{eq}} \frac{\rho_V u_V^2}{2} \tag{2.56}$$

  where $f_{strat(x \geqslant x_{IA})}$ is computed as:

$$f_{strat(x \geqslant x_{IA})} = \theta^*_{strat} f_V + (1 - \theta^*_{strat}) f_A \tag{2.57}$$

  where θ^*_{strat} is the normalized stratified angle defined as:

$$\theta^*_{strat} = \frac{\theta_{strat}}{2\pi} \tag{2.58}$$

  and θ_{strat} is calculated with equation 2.31. For the other zone of stratified flow $x < x_{IA}$,

$$\Delta P_{strat(x < x_{IA})} = \Delta P_{LO}(1 - \frac{\epsilon}{\epsilon_{IA}}) + \Delta P_{strat(x \geqslant x_{IA})}(\frac{\epsilon}{\epsilon_{IA}}) \tag{2.59}$$

- The frictional pressure drop in **bubbly** flow:

$$\Delta P_B = \Delta P_{LO}(1 - \frac{\epsilon}{\epsilon_{IA}}) + \Delta P_A(\frac{\epsilon}{\epsilon_{IA}}) \tag{2.60}$$

The pressure drop of bubbly flow is a combination of the single liquid phase pressure drop, ΔP_{LO} calculated with equation 2.42 and the pressure drop of annular flow, calculated with equation 2.46.

2.5 Heat transfer for evaporating CO_2

There are many models [73] to predict the local heat transfer coefficient (HTC) for evaporating fluids. One of the mostly used based on the Kandlikar model [74] is an empirical relation valid for two-phase fluid flowing in a horizontal or vertical tubes. Since, this thesis work mainly discusses the CO_2 fluid in horizontal flow, using the updated CO_2 flow-pattern map, an updated model for the HTC was also used for CO_2 evaporating inside horizontal tubes [70]. In the next Chapter, Kandlikar model and the updated CO_2 evaporating heat transfer model will be used to describe the HTC for the vertical and horizontal flow respectively.

The basic expressions of the HTC of the updated CO_2 evaporating heat transfer model are expressed as:

$$HTC = \frac{\theta_{dry} h_V + (2\pi - \theta_{dry}) h_{wet}}{2\pi} \tag{2.61}$$

where the angle called θ_{dry}, is introduced in Figure 2.5 and defines the flow structures and the ratio of the tube perimeter in contact with liquid and vapor. θ_{dry} has different values depending on the flow pattern. For the stratified flow (**S**), θ_{dry} =θ_{strat}(see equation 2.58). For the stratified-wavy zone (**SW**), when $x > x_{IA}$, θ_{dry} is calculated with equation 2.51. When $x < x_{IA}$, θ_{dry} is calculated with the following relation:

$$\theta_{dry} = \theta_{strat} \frac{x}{x_{IA}} (\frac{G_{wavy} - G}{G_{wavy} - G_{strat}})^{0.61} \tag{2.62}$$

For the annular flow (**A**), intermittent flow (**I**), and bubble flow (**B**), the $\theta_{dry} = 0$.

The parameters h_V and h_{wet} in equation 2.61 are the heat transfer coefficient of the vapor and liquid state fluid. The vapor heat transfer coefficient (h_V) is calculated with the Dittus Boelter [75] relation assuming turbulent flow inside the tube:

$$h_V = 0.023 Re_V^{0.8} Pr_V^{0.4} \frac{k_V}{D_{eq}} \tag{2.63}$$

where Re_V and Pr_V are the Reynolds and Prandtl number for the vapor phase, and k_V is the thermal conductivity in vapor phase. The expression of h_{wet} is given in Appendix.

The heat transfer coefficient in the mist flow (**M**) regime is calculated with the expression:

$$h_M = 2 \times 10^{-8} Re_H^{1.97} Pr_V^{1.06} Y^{-1.83} \frac{k_L}{D_{eq}} \tag{2.64}$$

where the homogeneous Reynolds number Re_H and the correction factor, Y, are defined by equation A.15 and A.16 in Appendix. Pr_V is the Prandtl number for the vapor phase. k_L is the thermal conductivity in liquid phase.

The heat transfer coefficient in the dry-out flow (**D**) is calculated using a linear interpolation.

$$h_{dryout} = h_{tp}(x_{di}) - \frac{x - x_{di}}{x - x_{de}} [h_{tp} x_{di} - h_M(x_{de})] \tag{2.65}$$

where $h_{tp}(x_{di})$ is the two-phase heat transfer coefficient calculated at the dry-out inception quality, x_{di}, and $h_M(x_{de})$ is the mist flow heat transfer coefficient calculated at the dry-out completion quality, x_{de}.

The heat transfer coefficient in the bubble flow (**B**) is calculated with the same method as that in the intermittent flow.

2.6 Model of single-phase pressure drop and heat transfer

The Darcy-Weisbach equation [75] is most commonly used to express the frictional pressure drop, ΔP_f, of a single phase fluid flowing in a pipe. It is valid for steady-state flow of incompressible fluid having high mass velocity. The Dittus-Boelter equation is used to calculate the heat transfer coefficient for turbulent flow of a single phase liquid. The turbulent flow happens when the viscous effects due to the shear stress between the fluid particles and the pipe wall create a fully developed velocity profile of the fluid as it travels through the length of the pipe. The velocity of the fluid is the highest at the center of the pipe, and the lowest on the wall. The two models mentioned above can be easily found in the textbook, therefore, they are not described in this thesis.

Chapter 3

Modeling of CO_2 two-phase cooling systems

The implementation of a numerical model into a software program of the heat transfer process for a two-phase CO_2 fluid is important for any practical application of this process, and in particular for the design of the cooling system of the detector components discussed in this thesis. In existing software package such as the Computed Fluid Dynamic (CFD) method, the description of liquid-vapor two-phase heat transfer is not particularly suitable for the CO_2 fluid.

A considerable and original effort of this thesis work was spent in building a software program based on the theory presented in Chapter 2 to describe two-phase system heat transfer process using CO_2 as coolant. The original idea of the program, known as CoBra (CO_2 BRAnch Calculator) was developed by Bart Verlaat [55]. The author of this thesis has given major contributions in implementing numerical models of evaporation and condensation processes. More recently, the author has developed a Graphical User Interface (GUI) enabling a wide use of this program within the ATLAS CO_2 cooling system design community. The CoBra program has a great potential in unifying various approaches and provides a common platform for different detector cooling applications.

In this Chapter, the CoBra program is described in detail. The program is applied to the calculation of various system parameters such as pressure drops and temperature gradients. These calculations are used in various design stages, including the verification of the required cooling power and the selection of system parameters such as the diameter of the cooling pipe and the mass flow rate.

3.1 Basic concepts

The aim of a cooling system is to bring the detector to a given predefined temperature and to keep the temperature constant even in presence of heat exchange between the detector and the cooling system. The process which happens inside the cooling part embedded in the detector is the evaporation process. Ideally the evaporation process is an iso-thermal process with the evaporation temperature depending on the pressure of the evaporating fluid. Along the cooling circuit, the heat absorbed by the fluid is used only for the phase transition, therefore, in principle, its temperature remains unchanged. However, in reality, as explained in Section 2.4, the pressure of the evaporating liquid inside the tube is subject to variations. Due to these variations, the temperature at which the evaporation process occurs also changes along the flow circuit, hence, the real evaporation process is not isothermal.

The heat exchanged during the flow in a pipe of an evaporating fluid results in a negative temperature gradient along the flow direction, while in a single-phase liquid flow the temper-

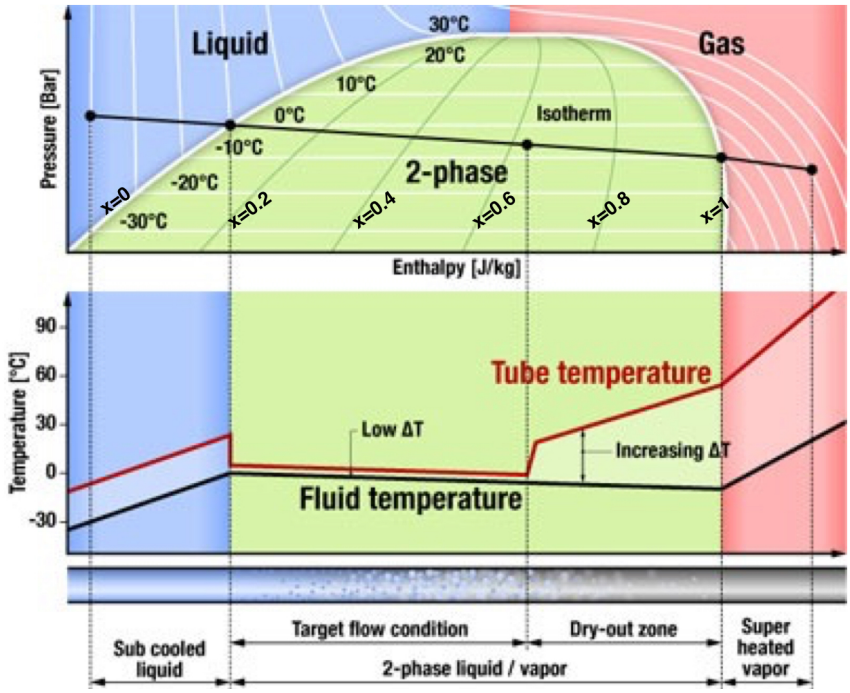

Figure 3.1: CO_2 phase diagram. The pressure (top plot) and temperature (bottom plot) along the cooling pipe are shown. The flow pattern inside horizontal tube is also shown.

ature gradient is positive. Figure 3.1 (top plot) is a phase diagram of CO_2. The plots on the top and on the bottom of the Figure represent respectively, the pressure and the temperature of the fluid as function of the specific enthalpy. The white lines in the top plot are the isothermal lines. The black lines in both plots describe respectively the pressure and temperature of the fluid flowing and exchanging heat along a pipe, while the red line in the bottom plot refers to the temperature evolution of the wall of the cooling pipe. The fluid in a liquid phase first absorbs heat and its temperature increases until the start of the liquid-vapor transition (bottom plot, black line). The temperature on the tube wall also continuously increases during this process (bottom plot, red line). Once the fluid enters into the state of liquid-vapor, the wall temperature drops to nearly the same as the temperature of the fluid. Afterwards, both temperatures of the fluid and the wall diminish due to the pressure drop as previously explained. This process happens within a certain range of value of the vapor quality. At a certain point, the temperature of the wall of the tube increases again, even though the fluid is still in a two-phase state. This point is where the fluid starts to enter into the dry-out and mist flow regimes as mentioned in Chapter 2. Once the fluid is completely changed into the vapor state, the temperatures of the fluid and of the tube wall increase rapidly.

3.2 Heat transfer model in CoBra

The CoBra program is able to perform various simulations of CO_2 heat and mass transfer during a steady-state flow inside a generic tube, for mono-phase and two-phase systems, with horizontal and vertical setup. In this program, the heat transfer process of conduction and convection are considered. The generic pipe will be also referred here as cooling circuit.

According to the first law of the thermodynamic (equation 2.3), the enthalpy variation of a fluid flowing in a steady-state condition through a pipe of constant cross sectional area is

related to the work and the heat exchange per unit of time via the relation:

$$\dot{m}(h_{in} - h_{out}) + \dot{Q} + \dot{W} = 0 \tag{3.1}$$

where $\dot{m}$ is the mass flow rate, h_{in} and h_{out} are the specific enthalpy at the inlet and outlet of the system (the pipe). The terms $\dot{Q}$ and $\dot{W}$ represent, respective as, the average exchanged heat and work per unit time. In the design of a cooling system for a detector, $\dot{Q}$ represents the heat per unit of time generated from the electronics and sensors. For a horizontal tube, there is no device producing work. The equation 3.1 is simplified as:

$$\dot{m}(h_{in} - h_{out}) + \dot{Q} = 0 \tag{3.2}$$

In the modeling of the heat exchange process, the cooling pipe is divided into a finite number of elements along the flow direction, called also segments. Each element is indicated by the letter "i". For each element, the energy conservation principle is applied and the pressure drop is calculated. The input parameter is the saturation temperature ($T(i)$) of the coolant. From $T(i)$, the saturation pressure ($P(i)$) and the enthalpy ($H(i)$) are derived (see Figure 3.1).

In a given segment, the heat input ($\dot{Q}_{ave}$(i)) from the detector is transferred to the fluid and the value of the enthalpy in $i+1$, $H(i+1)$ is computed, using equation 3.2. The pressure in $i+1$, $P(i+1)$, is obtained using the calculation of the pressure drop across the segment as explained in the previous Chapter. The local vapor quality $x(i+1)$ is then computed. The process is iterated for the next element and the calculation finishes at the end of the cooling pipe. Inside the program, at each element, the thermal properties of the CO_2 are updated based on its current thermophysical state. The thermal properties of CO_2 are taken from the database REFPROP developed by the National Institute of Standards and Technology (NIST, http://webbook.nist.gov/chemistry/fluid/). This CoBra program is developed using the computing language MATLAB. An interface function ("refpropm") which relates MATLAB

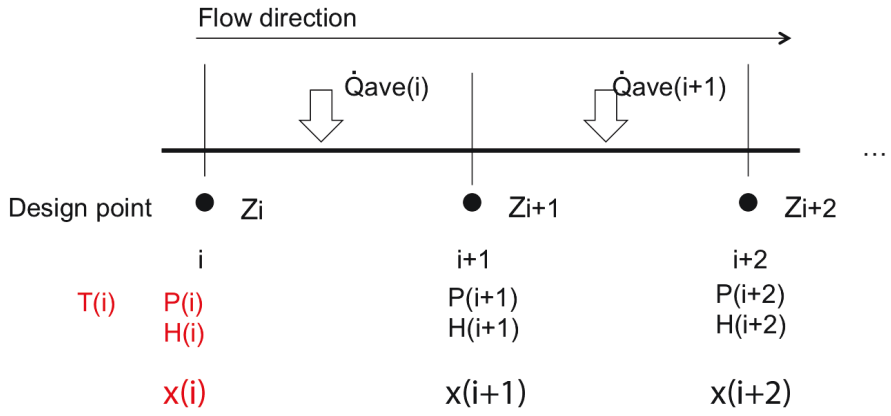

Figure 3.2: Illustration of the calculation procedure of CoBra.

and the CO_2 property database is used to retrieve the value of a given specific variable.

$$result = refpropm(prop_{req}, spec_1, value_1, spec_2, value_2, substance) \tag{3.3}$$

where $prop_{req}$ is an input character string indicating the property that is requested. $spec_1$ is a character specifying an input fluid parameter like, temperature, pressure, enthalpy or density. $value_1$ is the corresponding value for $spec_1$. $spec_2$ is a character giving a second specification, and $value_2$ is the value of $spec_2$. $substance$ is the name of a fluid in this case $'CO_2'$. As an

example, the saturation pressure (P_{sat}) is obtained from the saturation temperature when the vapor quality is equal to 0.

$$P_{sat} = refpropm('P','T', T_{sat},'X', 0,'CO2') \tag{3.4}$$

The vapor quality (x) is calculated according to the pressure and enthalpy values ($value_P$ and $value_H$ respectively):

$$x = refpropm('X','P', value_P,'H', value_H,'CO2') \tag{3.5}$$

A flow chart is drawn in Figure 3.3 to explain the program. The calculation steps are described in the following for horizontal flow:

- The input parameters, namely the saturation temperature (T_{sat}), the heat load ($\dot{Q}$), the length of the cooling pipe (L) the inner tube diameter (D), the angle of the pipe with respect to horizontal (θ_{tube}) and the mass flow rate (Fr) are given;
- The saturation pressure (P_{sat}) and the enthalpy of liquid (H_{liq}) are computed and used as initial parameters, P_{in}=P_{sat}, H_{in}=H_{liq};
- The physic state of the fluid is assessed based on the P_{in} and H_{in} (liquid, liquid-vapor, solid, gas, super-critical). If P_{in} is bigger than the pressure at the critical point (P_r), the fluid is in the super-critical state. If P_{in} is smaller than the pressure at the triple point (P_{tri}), the fluid is in the state of sublimation. If P_{in} is between P_{tri} and P_r, the fluid is either at liquid, vapor, or a mixture of liquid-vapor state;
- The super-critical state and sublimation process are not treated;
- If the fluid is in a liquid or vapor phase, the heat transfer coefficient and pressure drop are calculated using models of the heat transfer process for single-phase fluid;
- If the fluid is in a liquid-vapor state and θ=0^o, the flow pattern based on the local properties (G and x) is obtained. Possible patterns are Stratified flow, Intermittent flow, Annular flow, Dry-out flow, Mist flow and Bubble flow. The heat transfer coefficient (HTC) and the frictional pressure drop (ΔP_f) and the momentum pressure drop (ΔP_{mon}) are computed.
- The total pressure drop, the local HTC, the vapor quality (x), the temperature of the fluid (T_{CO2}) and the state of the fluid are returned;
- The temperature of the tube wall is calculated;
- The new pressure and enthalpy for the next element are computed;
- The calculation stops until the length reaches the end of the cooling pipe.

One of the parameters matters is the step size corresponding to the length of each element. This can be adjusted depending on various requirements of the termination.

As described above, the initial state is set manually giving the value of the saturation temperature, consequently, the saturation pressure and enthalpy are calculated, namely the saturation state is considered as the initial state. However, in our application the temperature of the Pixel Detector is controlled by the pressure in the accumulator (see Figure 1.18) since the pressure drop in the return line is small. As consequence the temperature at the outlet rather than at the inlet of the cooling pipe is fixed to the designed (saturation) temperature.

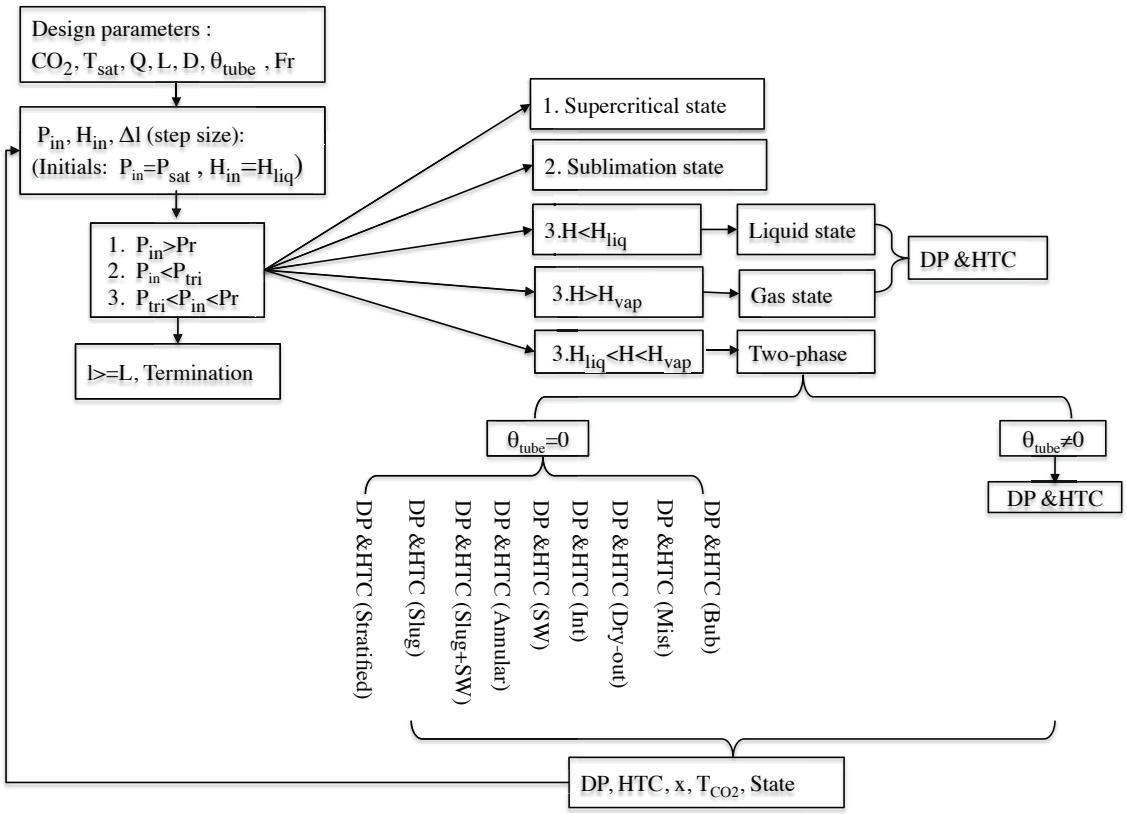

Figure 3.3: Flow chart of the CoBra program without iteration.

Motivated by this requirement, an iterative calculation is implemented to verify that the state parameters (pressure and enthalpy) at the outlet of the cooling pipe are at the saturation values. In the iteration, the initial parameters are still the saturation temperature, pressure and the initial enthalphy as previously described. At the end of the cooling pipe, the absolute pressure is compared with the saturation pressure. If there is a discrepancy, the initial tentative pressure is adjusted, until a converge criteria is reached. This part of iteration is illustrated in Figure 3.4 in the colored shapes. It is very likely that the fluid at the entrance of the cooling pipe is in a sub-cooled state at a condition of high pressure drop, therefore the liquid state calculations are also implemented in this design program.

3.3 Examples of CoBra

With the CoBra program, it is possible to predict the CO_2 thermal properties in a single phase (liquid or vapor) or two-phase heat transfer cooling system. The program allows to obtain the following quantities along the cooling pipe:

- The temperature distribution of the fluid and of the tube wall;
- The pressure distribution of the fluid;
- The vapor quality;
- The local heat transfer coefficient;

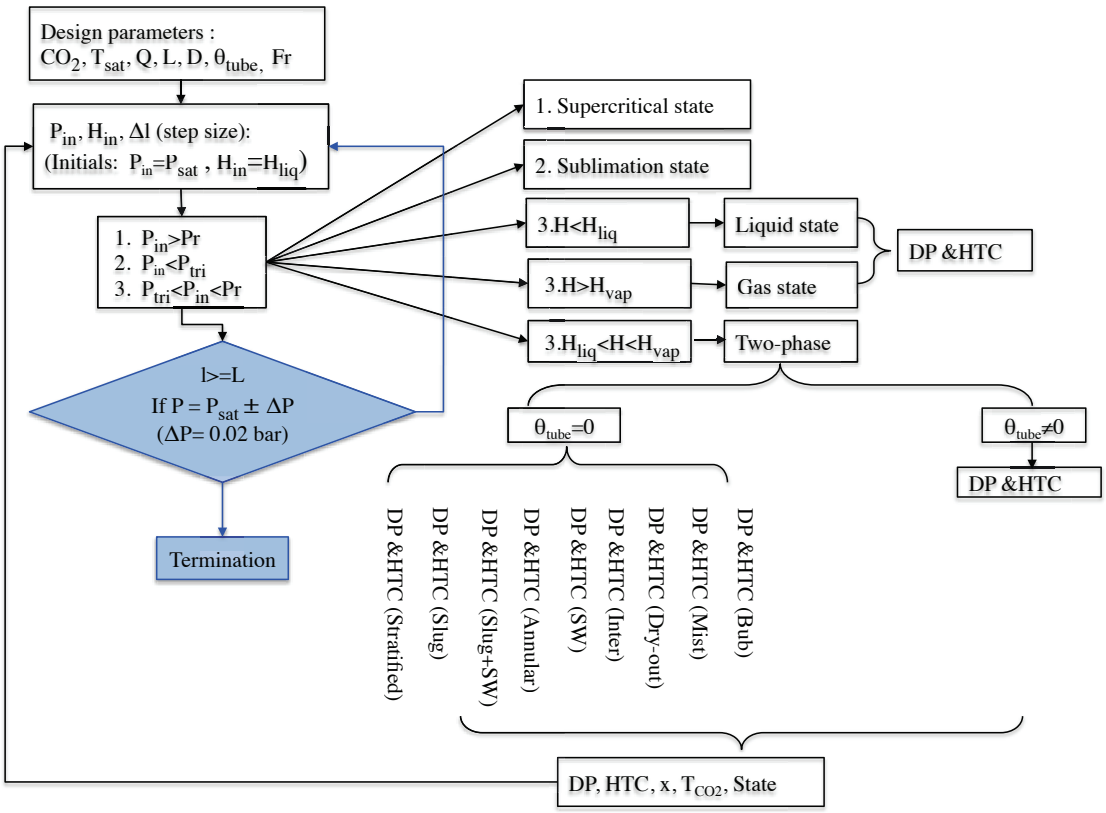

Figure 3.4: Flow chart of the CoBra program with iteration.

- The flow patterns inside horizontal tube with an equivalent diameter from 0.8 mm to 10 mm.

This information helps the design of cooling systems for tracking detector, as it allows the study of the impact on the cooling performance of parameters such as the length and the diameter of the cooling pipe for different power dissipation, at any given saturation temperature and mass flow rate. In the following section, realistic examples will be given to demonstrate the basic functionality of the program. In these examples, unless otherwise stated, the length of the cooling pipe is l= 1.5 m, the tube inner diameter is D =1.5 mm and the dissipated power is $\dot{Q}$ = 200 W. The saturation temperature (T_{sat}) is -20°C and a fluid mass flow rate (Fr) of 1 g/s is assumed.

3.3.1 Temperature and pressure distribution

In order to study the characteristic of such system and to verify whether this choice of parameter allows an efficient cooling, the fluid and tube wall temperatures, as well as the absolute pressure distribution along the cooling pipe are calculated and plotted in Figure 3.5. The blue line denotes the CO_2 fluid temperature (T_{CO2}), and the red line denotes the temperature of the pipe wall (T_{wall}). The CO_2 at the entrance of the cooling pipe at $L = 0$ is in the condition of two-phase state ($x \approx 0$). The Y-axis on the right is the absolute pressure (P) of CO_2 denoted by the black curve. A pressure drop of 0.5 bar between the entrance and the exit of the cooling pipe is induced by the two-phase flow. Such pressure drop causes a fluid temperature drop of 1 °C, from -20 °C to -21 °C. At the beginning of the cooling pipe the temperature difference between T_{wall} and T_{CO2} is 2.8 °C . This difference decreases along the flow direction until the

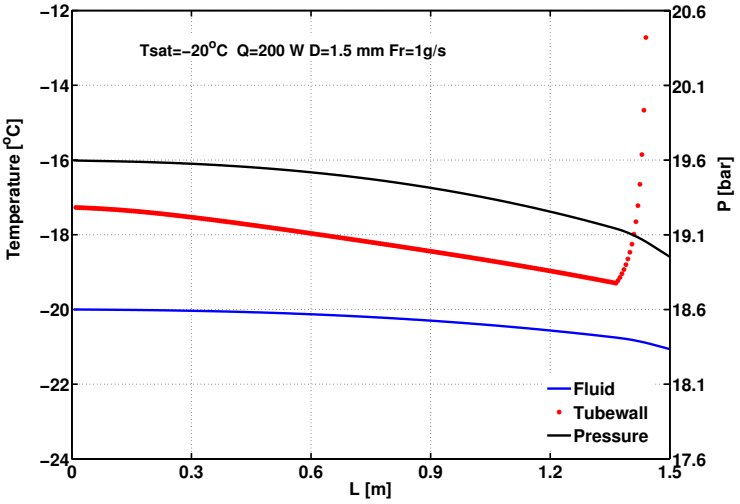

Figure 3.5: Temperature and pressure of the fluid and temperature of the tube wall along the flow direction for T_{sat}= -20 °C, $\dot{Q}$=200 W, Fr=1 g/s and D=1.5 mm.

fluid reaches the position l=1.36 m. Afterwards T_{wall} increases abruptly. This result shows that the assumed parameters do not allow an efficient cooling, since it would induce an extreme high temperature on the detector during normal operation. In the following, sections 3.3.2 and 3.3.3 will explain this phenomenon.

3.3.2 Vapor quality and heat transfer coefficient

The sudden change of the tube wall temperature can be understood by looking at the evolution of the vapor quality (x) and the local HTC along the flow path. These are presented in Figure 3.6. The left plot shows that x increases linearly along the flow direction. At the end of the pipe, it reaches a relatively high value of 0.7. The right plot shows the local HTC behavior along the cooling pipe. First, the local HTC increases with increasing x due to the more efficient two-phase heat transfer process with respect to mono-phase cooling. This is the main reason of the continuous drop of the temperature difference between T_{wall} and T_{CO2} along the flow direction until the position L =1.36 m is reached (as seen in Figure 3.5). After this position, a sharp decrease of a factor 10 of the HTC occurs which causes T_{wall} to increase dramatically. At this position (L =1.36 m), x reaches 0.65 and the two-phase flow begins to enter into the dry-out regime in which the liquid film around the tube wall starts to break into emerging bubbles. This dramatically decreases the local HTC and therefore leads to a large temperature difference between T_{wall} and T_{CO2} as also explained in [57].

3.3.3 Flow-pattern map

To understand the behavior of the local HTC along the fluid flow direction, the program provides the flow-pattern of the system according to the fluid and the pipe parameters. This is a powerful tool to know the flow conditions and helps to understand if the cooling fluid works efficiently and to estimate the margin to the dry-out regime. A flow-pattern map with the above defined parameters (T_{sat}, $\dot{Q}$, D, and l) is presented in Figure 3.7. In this figure, the chosen flow rate (Fr=1 g/s) is expressed in term of mass velocity (G=570 Kg/m^{2}s) and represented by the dashed blue line. Six flow regimes are represented on the Figure: Stratified flow (**Strat**), Stratify-wavy flow(**Strat-wavy**), Intermittent flow (**Intermittent**), Annular flow (**Annular**),

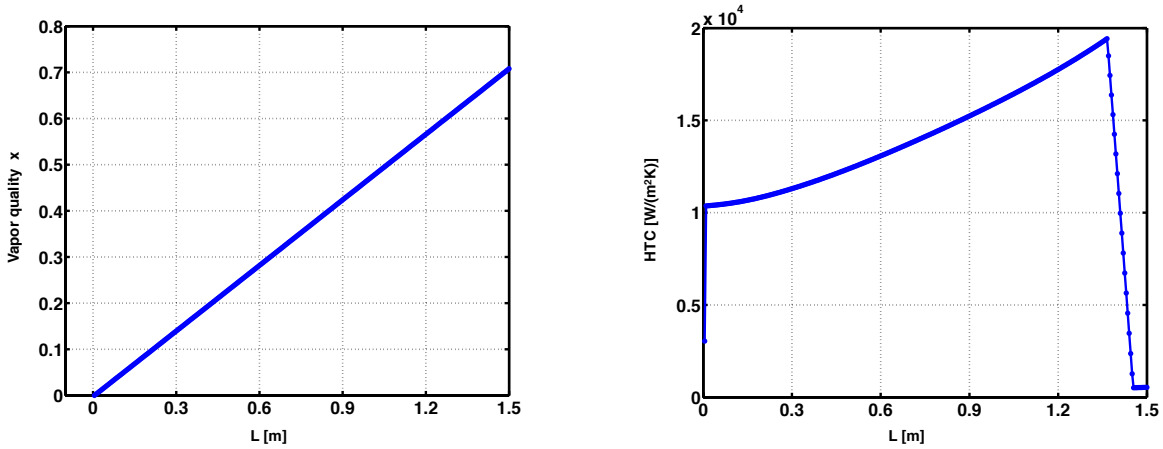

Figure 3.6: (Left) Vapor quality and (Right) heat transfer coefficient along the cooling pipe for T_{sat}= -20 °C, $\dot{Q}$=200 W, Fr=1 g/s and D=1.5 mm.

Dry-out flow (**Dry-out**) and Mist flow (**Mist**). The bubble flow regime requires a much higher mass velocity and therefore is not shown. The Figure shows that for the given mass velocity (G=570 Kg/m^{2}s), the CO_2 passes through the intermittent flow, the annular flow the dry-out flow regimes (at x=0.65) and finally ends in the mist flow regime.

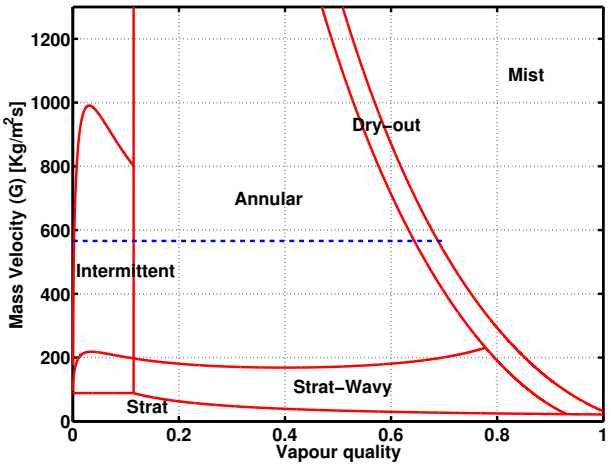

Figure 3.7: Flow pattern map of CO_2 for T_{sat}= -20 °C, $\dot{Q}$=200 W, Fr=1 g/s and D=1.5 mm.

Since with the assumed design parameters, (given as starting example) a sudden increase of the tube wall temperature is observed, these design parameters must be re-evaluated. Assuming that initially the fluid is in a liquid state, the total heat per unit of time ($\dot{Q}$) exchanged through the pipe can be expressed as:

$$\dot{Q} = Fr(C_p \Delta T_{liq} + x h_{LV}) \tag{3.6}$$

The specific thermal capacity of the cooling fluid is indicated with C_p and the first term represents the exchanged heat per unit of time which produces a temperature increase of ΔT_{liq} of CO_2 in the liquid state until the evaporation process starts. The second term is the exchanged heat per unit of time responsible for the evaporation process where h_{LV} is the latent heat of evaporation. It is expected that under a constant heat load, the increase of the mass flow rate will decrease the value of the vapor quality x at the end of the cooling pipe and allow more margin before the fluid reaches the dry-out regime, as shown from the left plot of Figure 3.8.

The right plot shows the effect of doubling the mass flow rate from 1 g/s to 2 g/s. The CO_2 does not enters into dry-out regime and the temperature of the tube wall does not have the dramatic increase as seen before.

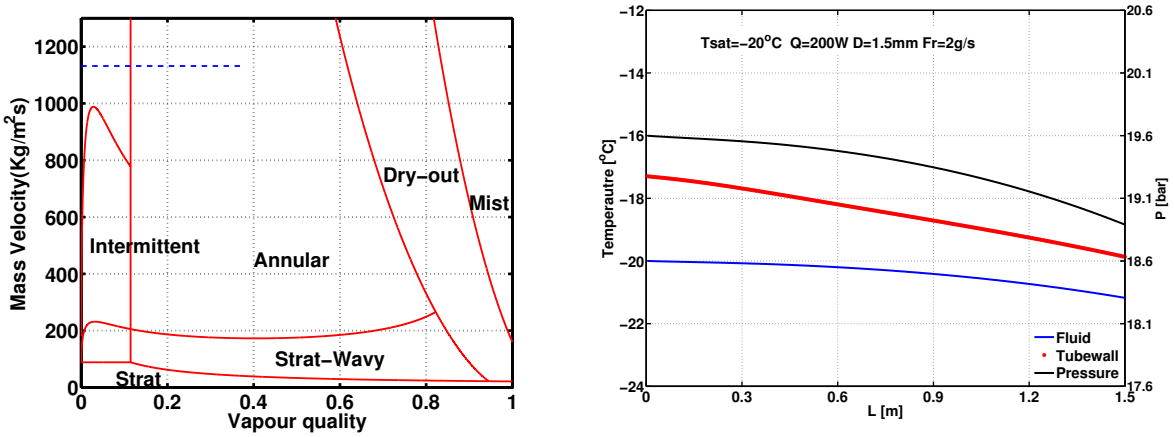

Figure 3.8: Flow pattern map of CO_2 (left plot) and temperature, pressure of the fluid, temperature of the tube wall along the flow direction for T_{sat}= -20 °C, $\dot{Q}$=200 W, Fr=**2 g/s** and D=1.5 mm.

Another possibility to avoid the sudden increase of the tube wall temperature is to increase the surface area of the cooling pipe, for example, by using a D=2 mm tube. Figure 3.9 (left plot) shows that with a bigger tube diameter, the mass velocity G (dashed line) is smaller and the transition boundary between annular and dry-out regimes is at a higher vapor quality, therefore the vapor quality at the end of the cooling pipe is far away from the dry-out regime. The right plot in Figure 3.9 shows the temperature and pressure distribution after increasing the tube diameter. It is seen that T_{wall} does not have anymore a sudden increase.

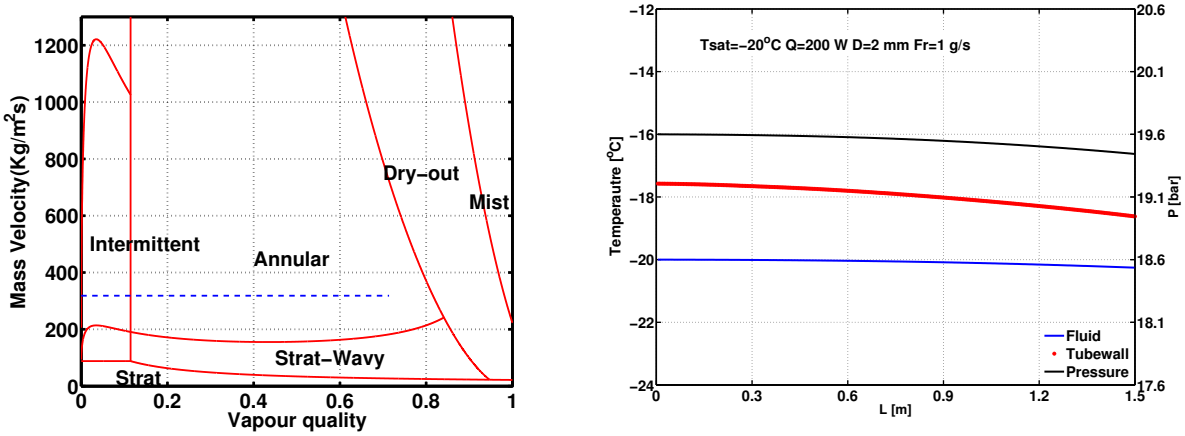

Figure 3.9: Flow pattern map of CO_2 (left plot) and temperature, pressure of the fluid, temperature of the tube wall along the flow direction for T_{sat}= -20 °C, $\dot{Q}$=200 W, Fr=1 g/s and D=**2 mm**.

A third possibility is to work at a lower saturation temperature of the CO_2 which leads to a higher h_{LV}. This change is expected to be less effective since h_{LV} changes very little as a function of saturation temperature.

3.3.4 Optimization of the tube diameter

The optimization of the tube diameter means to find the best value satisfying a given thermal performance in terms of tube wall temperature and temperature uniformity along the pipe, while using as less material as possible. One of the parameters to characterize this thermal performance is the observable ΔT_{total} which is the sum of two contributions:

$$\Delta T_{Total} = \Delta T_{HTC}^{MAX} + \Delta T_{dP} \tag{3.7}$$

The first contribution, ΔT_{HTC}^{MAX} represents the maximum temperature difference between the fluid and tube wall and is related to changes of the local HTC. The value of ΔT_{HTC} varies slowly along the flow direction and has a maximum at the inlet of the pipe (see Figure 3.10). This is considered as a characteristic value of the system. The second contribution, ΔT_{dP} is the temperature difference of the fluid between inlet and outlet of the evaporator due to the pressure drop. The sum of these two contributions quantify the maximum temperature difference between the tube wall and the saturation temperature of CO_2 . This is illustrated in Figure 3.10. The fluid temperature at the outlet of the pipe is taken as the designed saturation temperature.

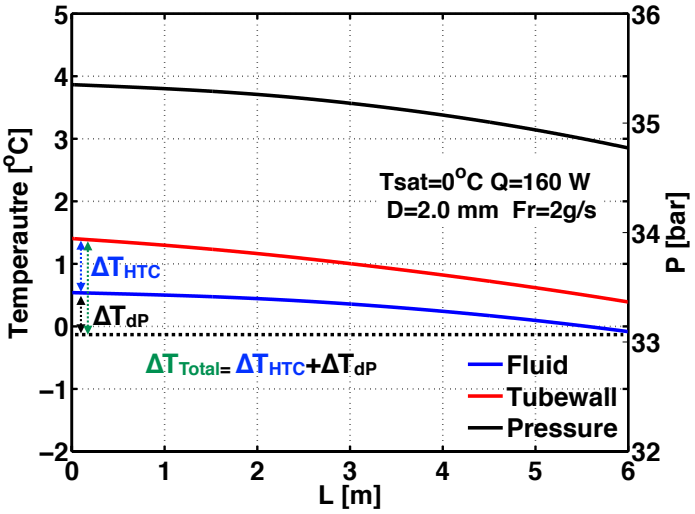

Figure 3.10: Fluid, tube wall temperature and pressure distribution for T_{sat}=0 °C, $\dot{Q}$=160 W, Fr=2 g/s and D=2 mm.

Another variable characterizing the thermal performance of the cooling system is the volumetric heat transfer coefficient (HTC_{vol}) defined as:

$$HTC_{vol} = \frac{\dot{Q}}{V_{vol}\Delta T_{Total}} \tag{3.8}$$

where $\dot{Q}$ is the total exchanged power through the pipe wall and V_{vol} is the total volume of the pipe (evaporator). This variable quantifies the heat transfer efficiency per unit of volume and serves as an optimization parameter. For a fixed $\dot{Q}$, a larger HTC_{vol} means a lower temperature gradient and less material. The optimum tube diameter in terms of thermal performance and material saving is achieved when HTC_{vol} reaches its maximum value.

As an illustration, HTC_{vol} and the temperature gradient ΔT_{HTC}, ΔT_{dP} and ΔT_{total} are presented in Figure 3.11, as a function of the tube diameter for the above system shown in Figure 3.10. In this case, the maximum of HTC_{vol} is reached at a value of tube diameter of

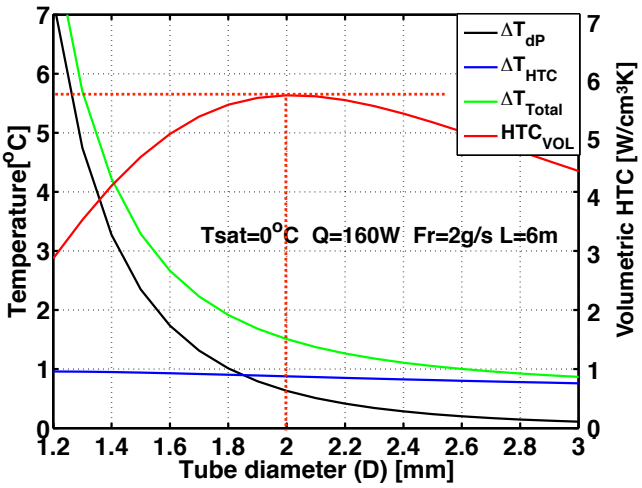

Figure 3.11: Optimal tube diameter for T_{sat}=0 °C, $\dot{Q}$=160 W, l= 6 m and Fr=2 g/s.

about 2.0 mm which corresponds to the optimal diameter. In addition, it is noticed that ΔT_{dP} has a significant dependence on tube diameter, while ΔT_{HTC} is almost constant. The large dependence of ΔT_{dP} on the tube diameter is due to the fact that two-phase frictional pressure drop is strongly and inversely proportional to tube diameter. The variable ΔT_{HTC} is related to HTC by the flow relation:

$$\Delta T_{HTC} = \frac{\dot{Q}}{HTC_{local} A} \tag{3.9}$$

As explained in Chapter 2, one of the advantage of two-phase cooling systems is that a larger input heat flux leads to a larger local HTC and therefore to a small ΔT_{HTC}.

To illustrate the impact of the tube diameter on the temperature of the tube wall, an example is given here. In this example, the total length of the cooling pipe is l =6 m, the evaporation temperature of CO_2 is 0 °C, the flow rate is 2 g/s and inlet vapor quality is x= 0.01. Results of the local HTC, pressure (P) and temperature of the tube wall (T_{wall}) obtained with D=1.0 mm, 1.5 mm, 2.0 mm and 3.0 mm for a heat load of $\dot{Q}$=160 W are shown in Figure 3.12 and Figure 3.13. When D=1.0 mm (upper left plot), the local HTC is the highest, as shown by the blue curve in Figure 3.12. In this case the pressure drop across the pipe (black curve) is above 15 bar and as a consequence, the change of T_{wall} along the cooling pipe is significant as shown by the blue curve in Figure 3.13. When the tube diameter increases, the local HTC significantly decreases and the pressure drop decreases also. As a result, the change of T_{wall} along the cooling pipe decreases as shown by the red, green and black curves in Figure 3.13.

In summary, the selection of the diameter of the cooling pipe is a trade-off process. On one hand, a small tube diameter is preferred since it allows to get a high local heat transfer coefficient and correspondingly a lower tube wall temperature and leads to less inactive material for tracking detector, while on the other hand, a smaller tube diameter generates higher pressure drop and correspondingly a high temperature gradient along the flow direction. A large temperature gradient is unfavorable as it may potentially affect the performance of the module and cause excessive thermal stress on the support structure of the detector.

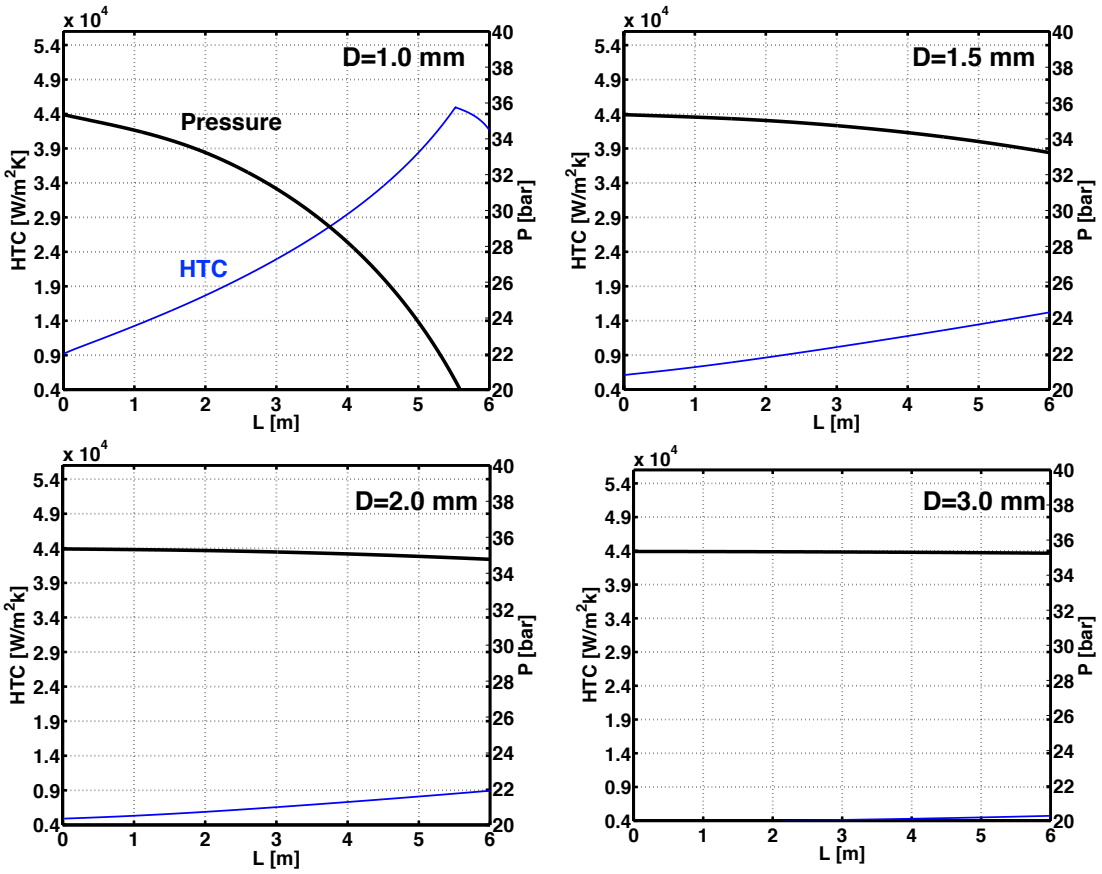

Figure 3.12: Heat transfer coefficient and pressure along the cooling pipe using a tube diameter of 1.0 mm, 1.5 mm, 2.0 mm and 3.0 mm. The applied heat load is 160 W, the saturation temperature is 0°C and flow rate is 2 g/s.

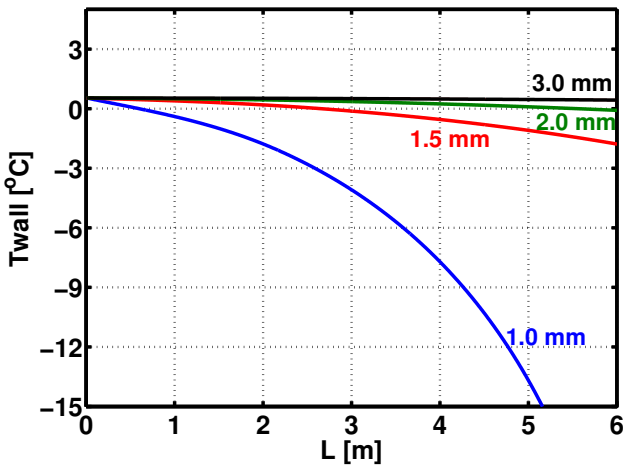

Figure 3.13: Comparison of the tube wall temperature along the pipe using a tube diameter of 1.0 mm, 1.5 mm, 2.0 mm and 3.0 mm. The applied heat load is 160 W, the length of the cooling pipe is 6 m and the saturation temperature is 0°C .

3.3.5 Minimum mass flow rate

As already described, in order to keep the system temperature under thermal requirements, it is mandatory to keep the two-phase flow away of the dry-out regime. This imposes a minimum

mass flow rate depending on specific heat load. To understand the minimum mass flow required for a given specific heat load, the pressure drop as a function of mass flow rate is studied. Figure 3.14 shows an example for a system with D=1.9 mm, l=6 m and T_{sat}= 0 °C . In this Figure,

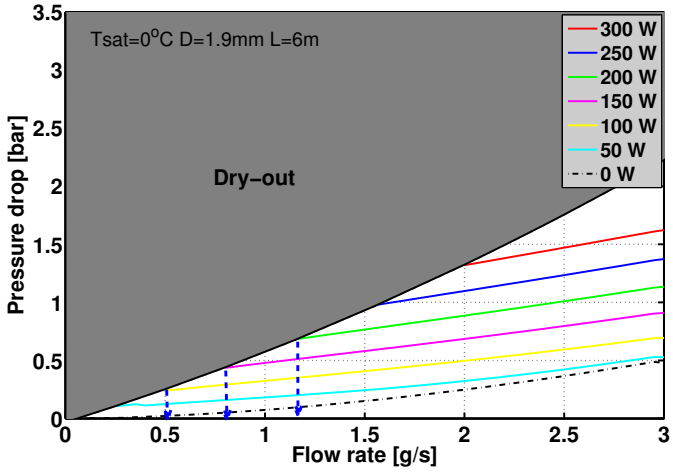

Figure 3.14: Pressure drop as function of the flow rate for different heat load.

the different colored curves represent the relation between the pressure drop and the flow rate under different heat load. For a given flow rate, the pressure drop increases with heat load. The grey area represents the dry-out region. The minimum required mass flow is defined by the intersection between each curve with the dry-out region is illustrated by the dash blue lines. As the heat load increases, the minimum flow rate increases: for example, 100 W of heat load requires a minimum mass flow rate of 0.5 g/s, 200 W of heat load needs a minimum flow rate of 1.2 g/s.

3.3.6 Mass distribution in parallel channels

The design of a complete cooling system for a tracking detector brings additional challenges with respect to the design of single cooling pipe. Since the detector is composed of several staves, the fluid must flow in separated branches and each branch is used for the cooling of one stave. The mass distribution of the cooling fluid in the branches is an important aspect. It has been observed that under a non-uniform heat load [76], the amount of fluid in different branches can be different. Therefore, while the fluid in some branches are enough to cool the stave, in some other branches the amount of fluid is insufficient leading to a larger vapor quality and as a result, the dry-out regime may occur [77]. In this case, the local temperature in the part of the detector may exceed the design requirements and may lead to safety problems [46].

In the following, the effects of unbalanced mass distribution in a multi-channel cooling systems will be discussed. Each branch is composed of an **Inlet tube**, a cooling pipe thermally connected to the heat source (detector component) and an **Outlet tube**, see also Figure 1.18 for the definition of the Inlet Tube and Outlet Tube. All the inlet tubes are connected to a **Inlet Manifold** where the fluid gets distributed, while the outlet tubes are connected to the **Outlet Manifold** where the fluid merges together. Figure 3.15 illustrates the configuration with inlet tubes, cooling pipes and outlet tubes with a length of 5 m, 3 m and 5 m, respectively. Various heat loads are applied to the different branches.

Figure 3.16 (left) shows the pressure drop as function of the mass flow rate for different branches under different power dissipation. The tube diameters are set to D_{inlet}= D= D_{outlet}= 2.0 mm. The plot on the right shows the result for the same configuration but with the inlet

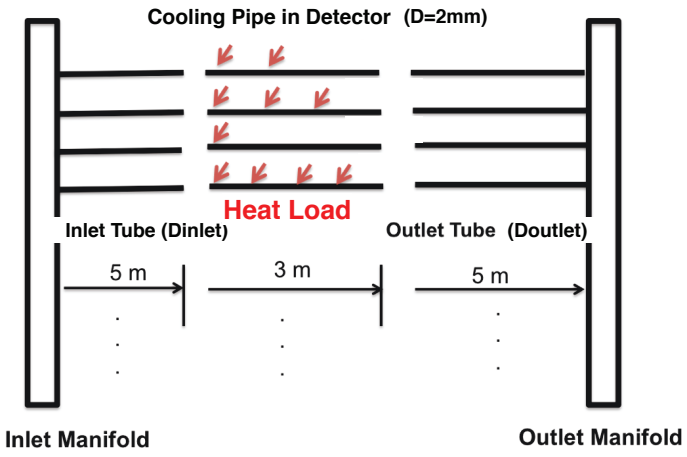

Figure 3.15: A schematic view of a multi-channel cooling system.

tube diameter changed from 2.0 to 1.0 mm. For both Figures the saturation temperature is 0 °C . Since the inlet and outlet tubes are connected to manifolds, the pressure drop are the

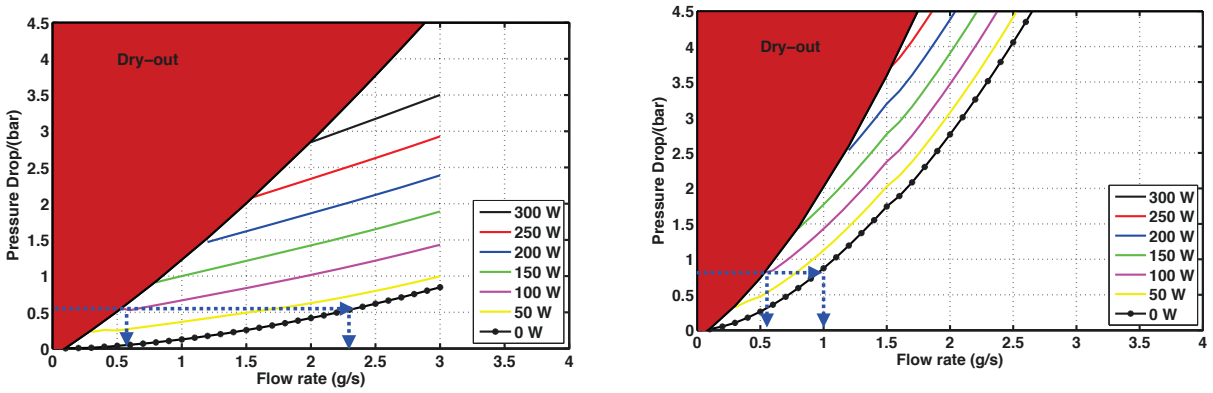

Figure 3.16: Pressure drop as function of the flow rate for different heat load: diameter of Inlet Tube is 2 mm (left) and 1mm (right)

same for all the branches. Therefore the channel with higher power density will have less fluid and it will be in this condition easier to reach the dry-out regime. This is illustrated by the blue dashed lines in the Figure. Assuming that one channel has a total power dissipation of 100 W (channel 1, red line), another channel has 50 W (channel 2, yellow line) and a third channel has no heat load at all (channel 3, black line), for a pressure drop (between the two manifolds) of 0.5 bar, the minimum flow rate is 2.3 g/s for channel 3, 1.7 g/s for channel 2 and 0.6 g/s for channel 1. When the inlet tube diameter is decreased to 1.0 mm, as in the case of Figure 3.16 on the right, for the same power input, a higher pressure drop is obtained and the minimum mass flow rate in the parallel channels is more uniform. This shows that the mass distribution between different channels can be highly asymmetric under unbalanced heat load and that carefully selecting the size of the tube diameters in different section of the cooling system helps mitigating this problem.

3.4 Graphical User Interface

For the HL-LHC, several detectors are going to use CO_2 based two-phase cooling system for their silicon detectors. To facilitate the design and to provide a general tool for optimizing the parameters of a cooling system, a User Graphic Interface(GUI) is also developed in the content of this thesis work. The first public version of this GUI is released in December of 2014. Apart from being used for the ATLAS pixel detector upgrade, this software is also used to develop CO_2 two-phase cooling system for ATLAS strip tracking detector.

The functionalities of the numerical program discussed above are provided. In the current version of GUI, they are implemented into three executable functions:

- Function 1: **Evaporator properties (dT,dP, VaporQuality and FlowPattern)**
- Function 2: **Evaporator Tube Diameter Optimization**
- Function 3: **Capillary+Inlet+Evaporator+Outlet(between manifolds)**

Figure 3.17 illustrates the results of function 1 which calculates the properties of the evaporator given the user input design parameters. There are four plots inside this interface. The top left plot shows the results of the temperature and pressure change with the flow direction. Top right and bottom left give the result of vapor quality and heat transfer coefficient. The flow pattern map is shown by the bottom right plot, which will guide designer to estimate the margin to dry-out regime.

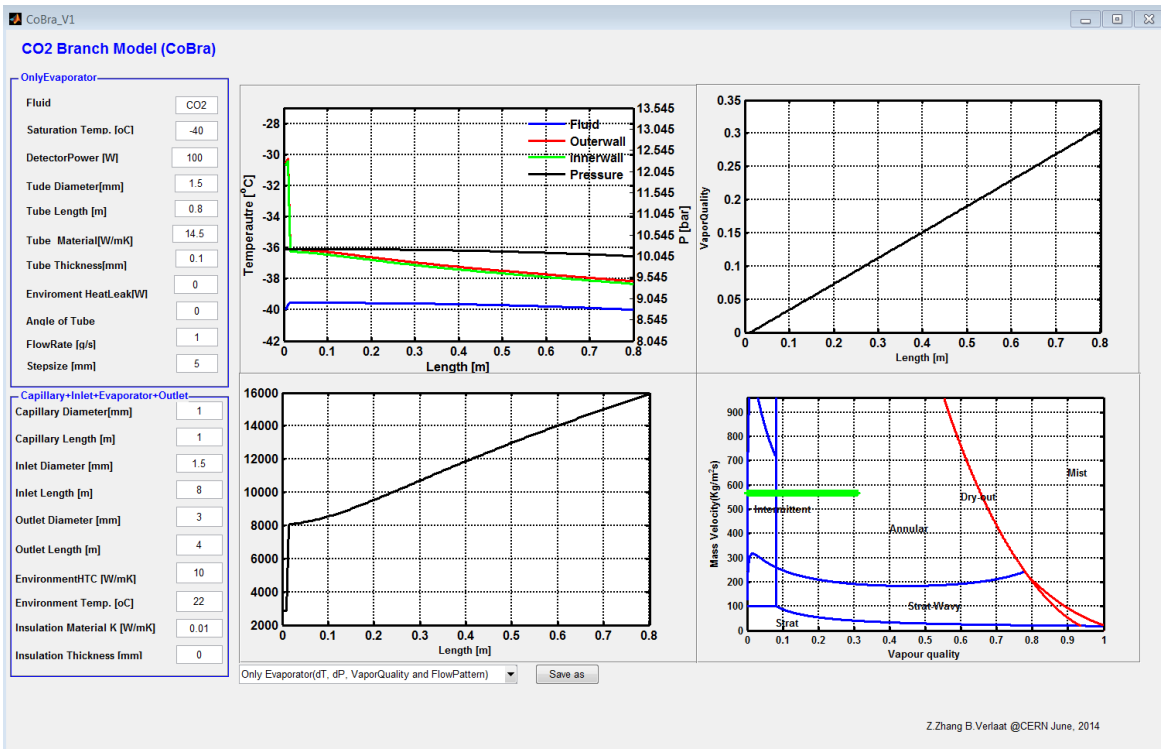

Figure 3.17: User graphic interface of CoBra-Function 1

Figure 3.18 presents usage of function 2 to evaluate the optimal tube diameter for a given configuration as described in Section 3.3.4. Figure 3.19 shows function 3 which is used to evaluate the heat transfer performance for several sections. Additionally, the environmental heat leak effect is implemented into this function.

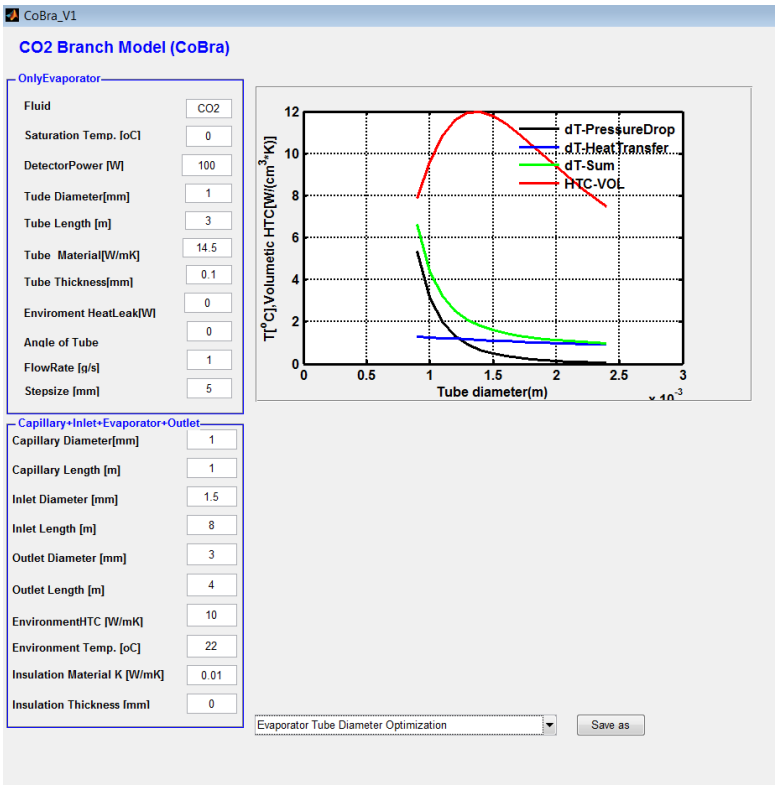

Figure 3.18: User graphic interface of CoBra-Function 2

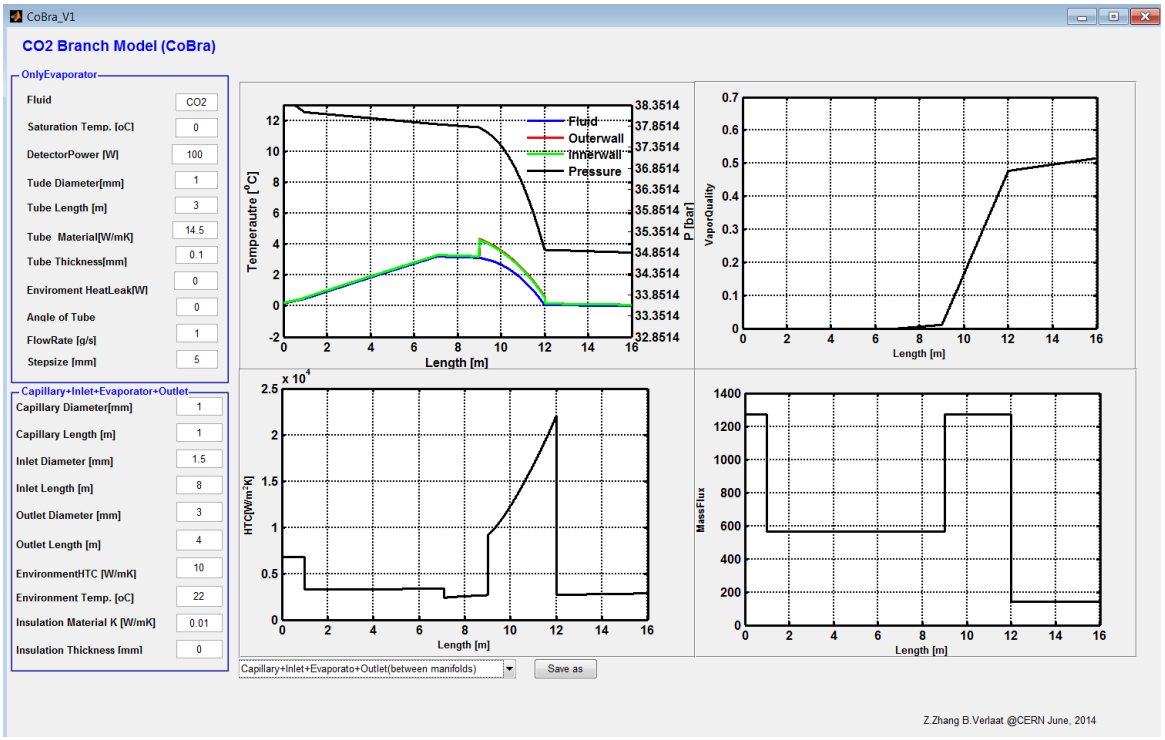

Figure 3.19: User graphic interface of CoBra-Function 3

The future development for this framework, including its GUI is to cover design and validation of all the components in the cooling system. Future development of the CoBra program and its GUI includes:

- Implement condensation heat transfer application for GUI;

- Improve user interface and implement multiple data exporting options;
- Introduce multi-channel functionality including description of mass distribution at manifold;
- Allow user-specification of discreet heat load configuration;
- Implement heat exchange process for two-phase heat exchanger design;
- Inclusion of micro-channel two-phase heat transfer model to extend the applicable range of the program;

3.5 Summary

In this chapter, a numerical program of CO_2 heat transfer called CoBra is developed. Its functionalities are described by giving examples. Several basic thermal properties of a cooling system are covered, namely the temperature and pressure distribution of the fluid, the vapor quality along the cooling pipe, the local heat transfer coefficient and the two-phase flow pattern. Several use cases of this framework such as tube diameter evaluation, mass flow rate selection and mass flow distribution are discussed. These functionalities make possible designing and evaluating the parameters for a detector cooling system. A graphical user interface is developed to facilitate the use of the program at design of the cooling system for tracking detector in ATLAS experiment. The work developed in this chapter will be used to design the cooling evaporator for the Alpine stave which is the subject of the second part of this thesis.

Chapter 4

Alpine Stave Design

In this Chapter, in addition to a more detailed presentation of the design of the Alpine stave, the material investigation, the structure optimization, the cooling properties evaluation and the choice of some operational parameters will be described. Finite Element Analysis (FEA) is used to analyze the temperature distribution and the thermal performance of the Alpine stave. The CO_2 evaporative heat transfer program developed in Chapter 3 is used to choose the operational parameters of the evaporator in the Alpine stave.

Section 4.1 gives a detailed introduction of the Alpine detector. The thermal requirements for the upgraded Pixel detector are presented in Section 4.2. These requirements define the design criteria for the local support structure and the cooling system. In Section 4.3, using the FEA technique, a preliminary design of the local support structure is presented. In Section 4.4, various optimization of the mechanical structure are described. In Section 4.5, a material investigation is carried out. Section 4.6 presents the design of the evaporator and its operational parameters, including the temperature and pressure drop distribution, the effects of varying the mass flow rate and the local heat flux.

4.1 Alpine stave

As described in Chapter 1, the Alpine layout is based on the innovative idea of building a Pixel detector with tilted sensors. The geometry of the Alpine stave presents many technical challenges, requiring a careful study of the mechanical stiffness and the thermal properties of the local support structure. Four layers of pixel are considered in the Alpine layout. The layer closest to the beam (Layer 0) has modules with "plains", while the other three layers have modules with "plains" and "mountains". As the current Pixel detector, the Alpine layout is separated into two symmetric parts at the position z=0: the "A side" and "C side". A view of the "A side" of the Alpine design is shown in Figure 4.1. The region with modules parallel to the beam axis is in the middle of the detector and is called "barrel", while in the region at higher η, ("end-cap"), the sensors are mounted on tilted support structures.

Figure 4.2 shows the geometry of one stave of the Layer 1 of the Alpine layout. The stave uses a carbon fiber composite as support material, like the IBL stave. A module is attached to it via a "face-plate" in composite material. For each stave, a titanium cooling tube is used to circulate the fluid in order to cool the modules. Since the detector is divided into two parts at z=0, the cooling tube, which is embedded in the stave, cannot pass through the X-Y plane at z=0. Instead, it makes a U-turn and returns to the place where the fluid enters. Therefore, the length of the cooling pipe in each stave is about twice longer than that of the stave itself. The two parts of the cooling pipe will be identified as "in-going" pipe and "out-going" pipe.

Different types of modules are foreseen depending on the different locations on the stave.

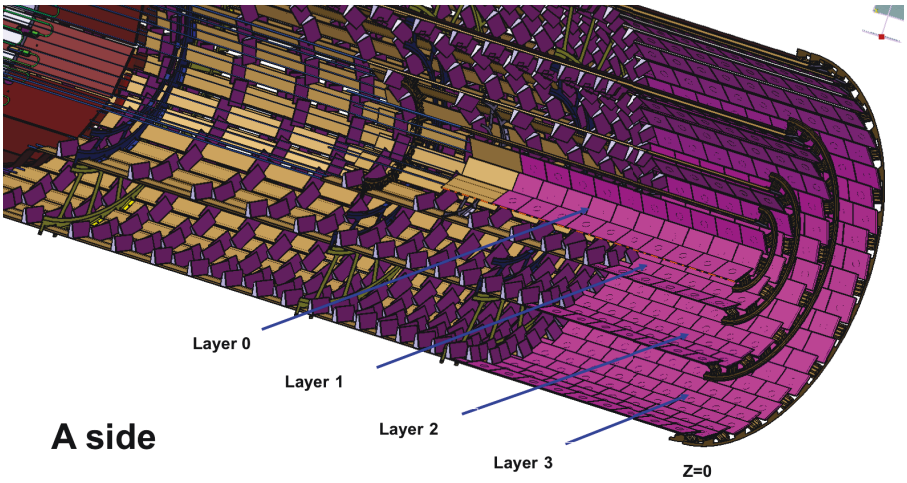

Figure 4.1: A detailed view of the "A side" of the Alpine Pixel detector.

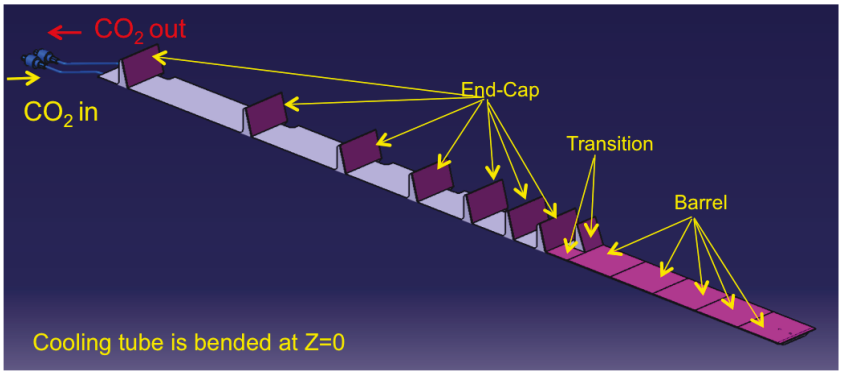

Figure 4.2: Preliminary design of one stave of Layer 1.

In the barrel region of the stave, "quad" modules (M4) are placed. In the end-cap (mountain) region, "dual" modules (M2) are located. In the transition region, modules (M1) with one read-out chip are under consideration. As an example, in Layer 1, there are five M4 modules, seven M2 modules and two M1 modules. As illustrated in Figure 4.3, Layers 0, 1, 2 and 3 have in total 8, 16, 32 and 52 staves, respectively.

A module "flex" lays on top of the modules and connects the front-end electronics and the sensors (bump-bonded together) to the stave flex which transmits the data to the outside of the detector. The connection between module flex and stave flex is realized by wire bonding. Figure 4.4 shows a preliminary design of the module flex implementation for different regions of the Alpine stave. As it is shown, at present, a bend of the module flex is envisaged to follow the Alpine geometry. The stave flex lays on the bottom of the stave.

4.2 Thermal requirements

The power per unit of surface (power density) from each module is assumed to be between 0.5 W/cm^2 and 0.7 W/cm^2 depending on the radial distance of the layer to the beam axis. These values include a safety factor of 1.2. Layer 0 and 1, closer to the beam, are exposed to higher radiation. For this reason a power density of 0.7 W/cm^2 is considered while for Layers 2 and 3 a power density of 0.5 W/cm^2 is assumed. Taking into account the module area, the power density from a module is converted into power dissipated and shown in Table 4.1. Based on the assumed power dissipated by the different module types, the total power consumption for

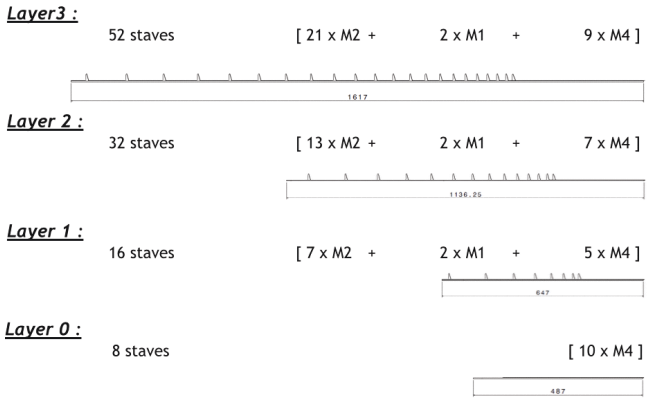

Figure 4.3: Number of staves per layer and number and type of sensors (M1, M2 and M4) per stave

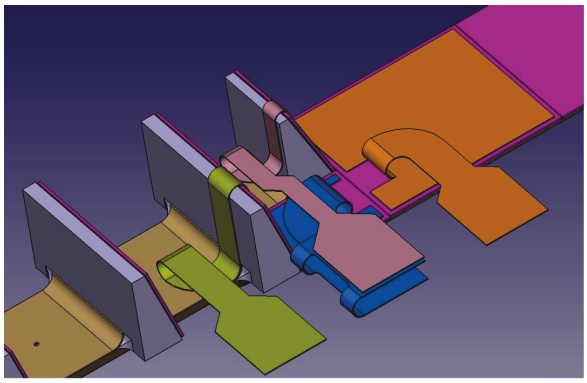

Figure 4.4: Preliminary design of the implementation of the module flex.

each stave is calculated and listed in Table 4.2.

Assumptions are made in order to establish preliminary baseline requirements. One of the assumption is that the sensors on the outermost layers (i.e. Layer 2 and Layer 3) will stand the radiation dose for the full life time of the experiment (about 10 years), while the innermost layers (i.e. Layer 0 and Layer 1) will be replaced at least once during the same period. The Thermal Figure of Merit of the local support structure ($TFoM_{Support}$), defined in Chapter 1 without considering the heat transfer process, needs to be below 15 Kcm^2/W for the innermost layers and below 13 Kcm^2/W for the outermost layers [78, 79] based on the preliminary analysis for the Planar and 3D sensors. A list of preliminary values for the main design parameters related to the thermal behavior of the support structure is given in Table 4.3.

As already mentioned, the purpose of a cooling system is to collect the dissipated heat in the Pixel detector modules, to transport it to the cooling plant, and to keep the sensors' temperature below a certain value in order to avoid the thermal runaway phenomenon. In the two-phase cooling system, the requirement on the evaporation temperature of the cooling fluid in Table 4.3 derives from the following consideration. Generally, for tracking detector, the sensor temperature should be below -20 °C during normal running. This is reasonably safe for avoiding radiation damage effects and thermal runaway. A typical thermal gradient between the sensors and the evaporation temperature of the cooling fluid is of the order of 15 °C, meaning that the temperature of the fluid needs to be around -35 °C or lower to keep the sensors below

Table 4.1: Power dissipated per module for the three module types (M1, M2 and M4)

Regions	Module name	Module surface [mm^2]	Power(L1) [W]	Power(L2 and L3) [W]
Transition	M1	20.4×18.0	2.3	1.6
Mountain	M2	20.4×35.6	4.6	3.2
Plain	M4	40.4×35.6	9.2	6.4

Table 4.2: Numbers of module per stave and total power consumption per stave for Layer 1, 2 and 3.

Layer	Mod./stave M4	Mod./stave M2	Mod./stave M1	Num. Stave	Length [m]	Heat load/stave [W]
1	5	7	2	16	0.6	83
2	7	13	2	32	1.1	90
3	9	21	2	52	1.6	128

-20 °C. Therefore, the requirement for the maximum temperature of the cooling fluid is set preliminarily at -35 °C. A two-phase cooling system using CO_2 with saturation temperature at -40 °C is expected to match the requirement.

4.3 Design of the local support structure

The structure of the Alpine stave has a relatively complex geometry with multiple materials and is impossible to obtain an analytic expression of the temperature distribution and corresponding thermal performance. Therefore, in this work, a thermal analysis of the Alpine structure is performed using a finite element analysis (FEA). FEA is a numerical analysis technique for obtaining approximate solutions for a wide variety of engineering problems. For this work, a software named ANSYS[80] will be used. A steady-state condition is considered.

4.3.1 Description of the local support structure

As a first step of this calculation, the support structure for the mountain regions is described using a 3D FEA model. Figure 4.5 shows the dimensions of a mountain of the tilted region (20.4 mm x 35.6 mm). For the module, an inclination of 68 °, shown in Figure 4.5, is designed with respect to the horizontal plane for a better tracking of the particles emerging from the beam interaction point. To simulate a mountain region, layers of different materials are introduced in the 3D FEA model, as described in the following and in Figure 4.6. The mountain is mainly made of carbon foam. Then one layer of glue is used to glue the face-plate, which is the surface background for implementing the pixel modules. Starting from the face-plate and moving towards the outside of the inclined structure, there are layers of parylen (for electrical insulation), thermal grease (for heat transfer), electronic chip, bump-bounding and silicon sensor. The thickness and thermal properties of the various material are listed in Table 4.4. The thermal properties are based on the IBL detector. The cooling pipe is also implemented in this 3D model, together with one fine layer of glue between the tube and the carbon foam. The diameter of the titanium tube is 1.5 mm, with a distance of 18 mm between the in-going

Table 4.3: Preliminary design parameters for the local support structure

Innermost layers: 0, 1	Design values
Module power density[W/cm^2]	0.7
$TFoM_{Support}$ [Kcm^2/W]	15
Temperature uniformity within a module [°C]	±1
$T_{Evaporation}$ [°C]	-35
Outermost layers: 2, 3	**Design Values**
Module [W/cm^2]	0.5
$TFoM_{Support}$ [Kcm^2/W]	13
Temperature uniformity within a module [°C]	±1
$T_{Evaporation}$ [°C]	-35

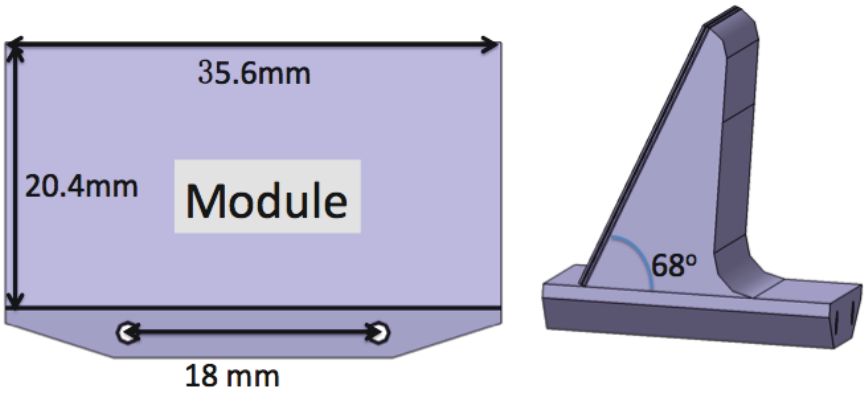

Figure 4.5: 3D drawing of an mountain

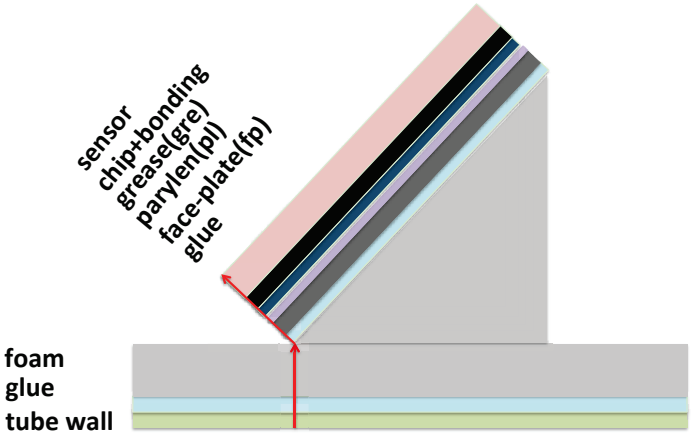

Figure 4.6: Illustration of the materials used in the FEA simulations.

and out-going pipe. It is important to notice, as this is of relevance for the simulation, that the face-plate material is a composite material made of three layers of carbon fibers (K13C/RS3) with fibers direction of $0^o/90^o/0^o$ piling up and cured together.

Table 4.4: Thermal properties and thickness of each layer used in the simulation

Materials	Thermal conductivity [W/m·K]	Thickness [mm]	Density kg/m^3
Silicon sensor	148	0.23	2.3
Bump-bonding	6.3	0.02	1.4
Silicon chip(FEI4)	148	0.15	2.3
Grease(HTCP Electrolub)	1.5	0.10	3.0
Parylen	0.2	0.05	1.4
Face-plate (K13C/RS3)	96/0.5/0.5 (Kx/Ky/Kz, see text)	0.145	1.7
Carbon foam (K9)	40		0.22
Glue (Stycast 2850FT)	1.1	0.10	2.7
Titanium tube (T40)	16.5	0.10	4.5

4.3.2 Steady-state thermal analysis

This section describes a preliminary study done using FEA. A power density from the modules of 0.4 W/cm^2 is used without considering the safety factor, as required for Layer 2 and 3. The basic procedure of a thermal steady state analysis in ANSYS proceeds [80] along the following steps:

- input the thermal properties of the materials (mode "Engineering Data"),
- import the mechanical geometry model (mode "Geometry"),
- mesh the mechanical geometry,
- apply the initialization and thermal loads to the model,
- solve and get the results.

To simulate the face-plate material, its thermal conductivity is set independently along x ("in-plane", along mountain slope), y ("in-plane", orthogonal to x) and z ("through-plane") directions.

A constant temperature 0°C is applied on the internal faces of the cooling pipe considered as the heat sink. Therefore, the results of FEA have to be interpreted as a temperature difference with respect to the inner tube wall ($\Delta T_{Support}$). As described later, the temperature difference between the inner tube wall and the CO_2 fluid (ΔT_{CO2}) is calculated using the CoBra program developed in Chapter 3. The combination of the FEA calculation of $\Delta T_{Support}$, and the calculation from the CoBra of ΔT_{CO2}, gives a full description of the thermal performance of the support stave.

It is expected that in each layer, the maximum temperature will be reached at the top of the mountains since these regions are far from the cooling pipe. Therefore, if the temperature requirements are satisfied at these locations, they will be automatically satisfied at every location along the stave. Figure 4.7 shows the simulated structure and, using different color, the FEA results of the temperature distribution in the mountain region of Layer 1. The temperature difference of $\Delta T_{Support}$ reaches the highest values at the top of each mountain, as expected.

With a distance between consecutive mountains varying from 118 mm to 20 mm, the temperature at top of the mountain increases less than 0.2 °C from 6.4 °C (on mountain 1) to 6.6 °C (on mountain 7). If the ΔT_{CO2} is designed to be less than 5°C , this result shows that in the assumed conditions, the studied design meets the requirement of keeping the sensor and the electronics at a temperature below -20 °C since the thermal gradient between the CO_2 fluid and the top of each mountain is expected to be less than 15 °C .

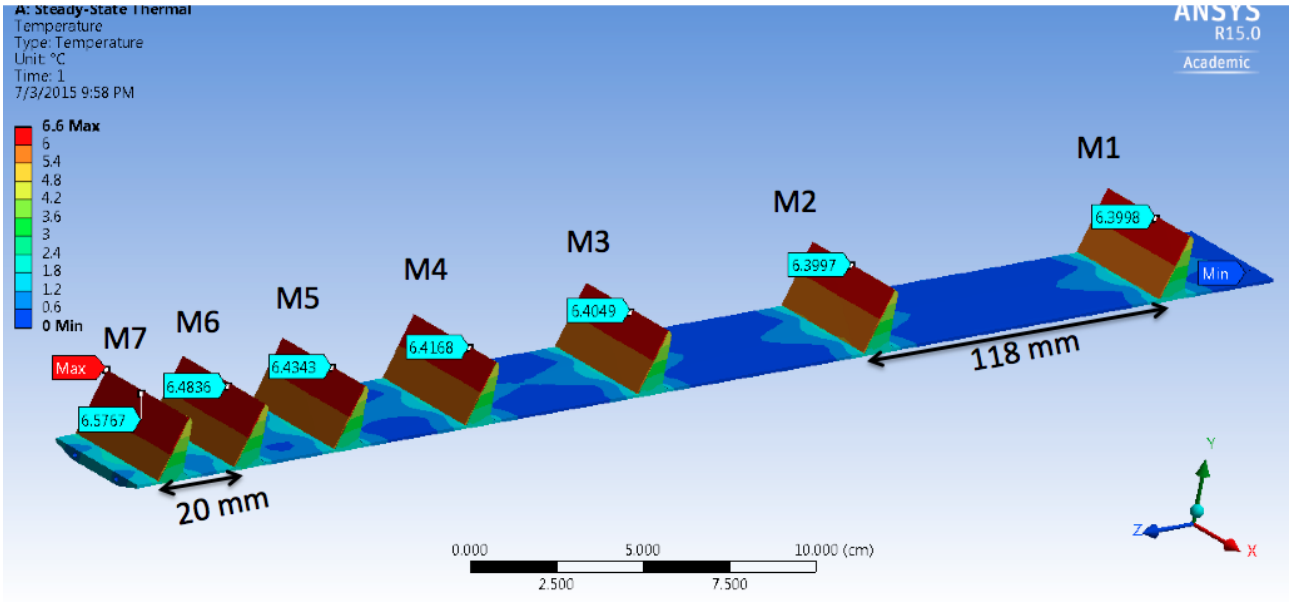

Figure 4.7: Temperature distribution in Layer 1 with seven mountains (FEA results). From right to left, the mountains are counted as M1 to M7. The temperature difference at the top of each mountain is also shown.

Figure 4.8 shows the temperature distribution on the sensor (left) and on the face-plate (right). The temperature uniformity across sensors and face-plates are within 1.0 °C and 3.0 °C respectively. These results suggest that even if a bigger temperature gradient exist across the face-plate, the high thermal conductivity of the silicon mitigates the temperature gradient across the sensors. The heat flux through the wall of the cooling pipe as function of the flow

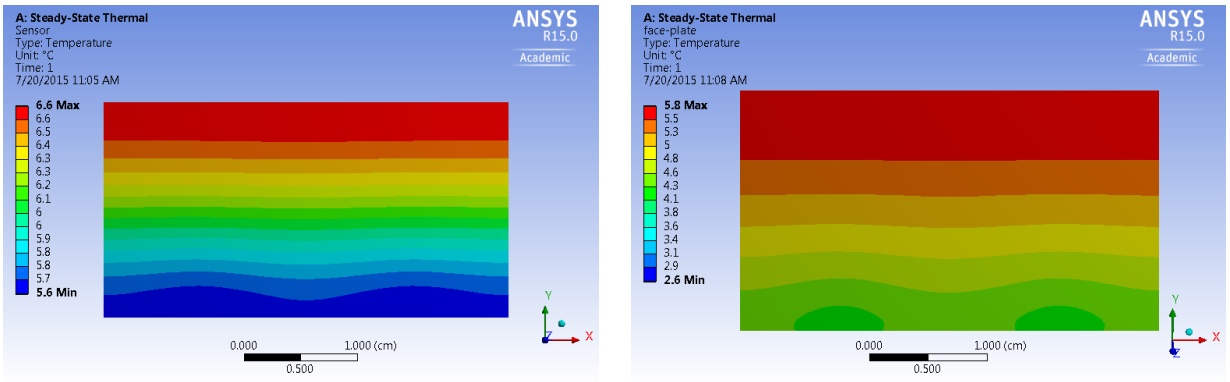

Figure 4.8: Temperature distribution on the sensor(left) and on the face-plate (right). The minimum temperature is 5.6 °C and 2.6 °C for the sensor and face-plate, respectively. The maximum is 6.6 °C and 5.8 °C for the sensor and face-plate, respectively.

direction is illustrated in Figure 4.9. The maximum heat flux at the position of each mountain

is nearly the same for mountains from 1 to 4, while for mountains from 5 to 7, the maximum heat fluxes gradually increase since the heat flux does not return to its initial value after the maximum, especially for mountain 6 and 7, however, this effect has a little impact on the temperature at the top of the mountains, as shown in Figure 4.7.

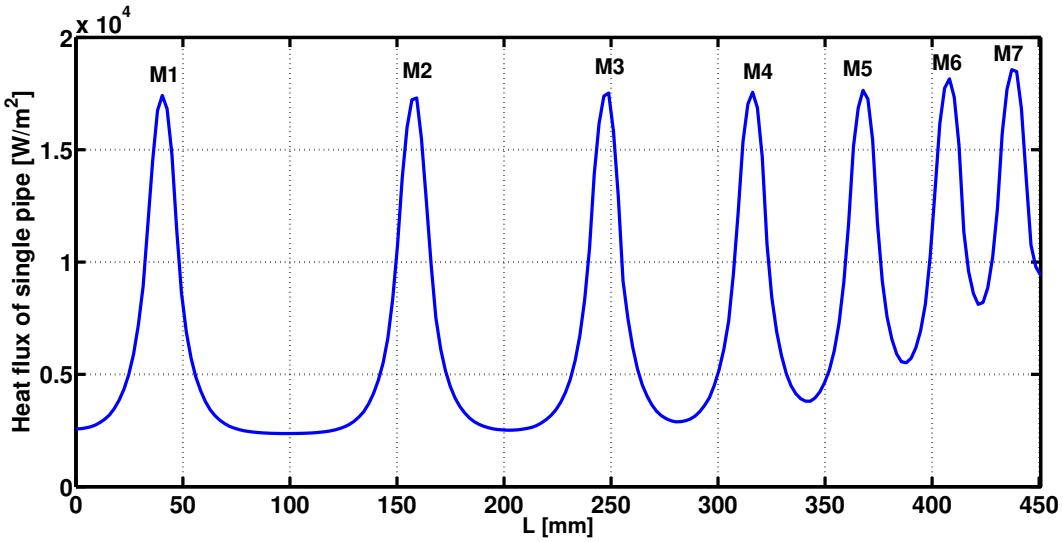

Figure 4.9: Heat flux throug the pipe for Layer 1 in the region with seven mountains

The temperature and heat flux distributions indicate that the presence of neighboring modules have a little influence on the temperature at top of the mountain, and that the carbon foam in between mountains does not give a significant contribution to the overall thermal performance and further reduction of material is feasible.

4.4 Optimization of the support structure

Several optimizations of the geometry and of the manufacture procedure of the Alpine stave are studied based on the above baseline model. The aims of the optimizations are to make the stave structure lighter, cheaper and robust, satisfying at the same time the imposed geometrical and thermal constraints. For example, the components of the structure must be able to stand a given heat load without failure, their dimensions are fixed and a given working range of temperature must be respected. Based on these criteria, few optimizations [81] of the local support structure are carried out assuming that the power density from each module is 0.5 W/cm^2, as required for Layer 2 and 3.

4.4.1 The base length of the foam in the mountain region

The optimization of the carbon foam geometry is carried out in order to minimize the passive material. Since the highest heat flux through the pipe occurs at the position of the mountains along the stave (Figure 4.9) and it was shown (Figure 4.7) that the presence of adjacent modules has a negligible effect, the temperature distribution of a single mountain is studied as a function of the length of the base of the carbon foam structure (see Figure 4.10 a)).

The parameter d_1 and d_2 are the distance between the edges of the structure and the base of the mountain: d_1 is the distance on the front side of the mountain (side closer to the beam interaction point) and d_2 is the distance on the rear of the mountain. The thermal performance

due to the variation of d_1 and d_2 are investigated. The length of the carbon foam underneath the mountain (d_0 = 12 mm) is kept constant.

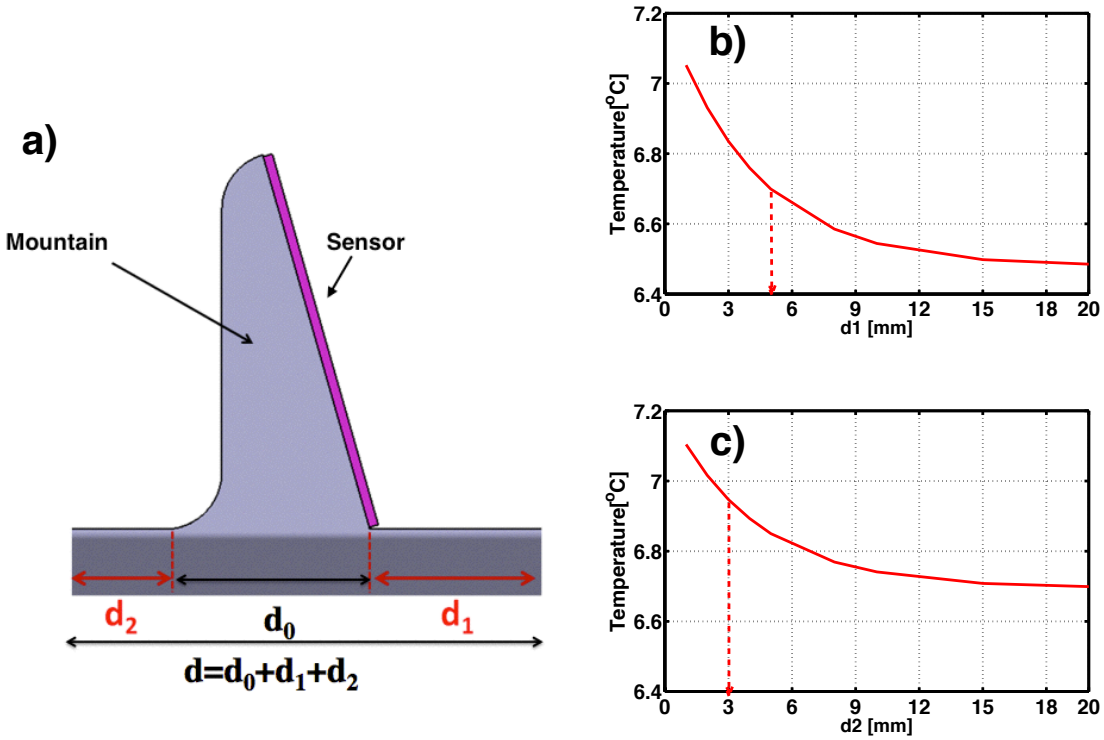

Figure 4.10: 3D model of a single "mountain" (a) and the results of the optimization of the base length of the foam d_1 (b) and d_2 (c).

As first step, d_2 is fixed at 20 mm and d_1 is varied from 1 to 118 mm (118 mm is the maximum distance between two mountains modules. Figure 4.10 b) illustrates the temperature variation at the top of the mountain as a function of the length of d_1 (up to 20 mm). A temperature variation of less than 0.5 °C is observed over the considered length. A value of d_1 = 5 mm is selected, as any lower value may induce a manufacture difficulty and mechanical weakness, while a longer value of d_1 would imply more material. In the second step, d_2 is varied from 1 to 118 mm with d_1 set to 5 mm. Figure 4.10 c) presents the temperature on the top of the mountain as function of d_2. The figure shows that again the temperature changes very little over the considered length. A value of 3 mm is selected for d_2.

This study verifies the expectation that the values of d_1 and d_2 have a small impact on the temperature at top of the mountain. With the final choice of d_1 = 5 mm and d_2 = 3 mm, a maximum temperature difference between the top of the mountain and the inner tube wall of 6.9 °C is found. With these choices a lot of carbon foam in between the mountains is cut out. This will reduce significantly the passive material.

4.4.2 Optimization of the structure at the base of the mountain

The optimization of the structure from the mechanical point of view is also considered. The stiffness of structure is assured mainly by a reinforced carbon fiber structure at the bottom of the mountain. Two shapes, V-shape and U-shape, are considered, as shown in Figure 4.11.

The mechanical simulation indicates that a U-shape carbon fiber provides a better stiffness than a V-shape. Moreover, the physics simulation showed that for a better particle tracking, an inclination of 72^o rather than 68^o of the module is preferred, therefore the thermal FEA is carried out again to check this new design. The length of carbon foam d_0 is now reduced from 12 to 11 mm. After these changes, the FEA shows that the temperature, $\Delta T_{support}$, is increased by about 1°C, reaching to 7.8°C (see Figure 4.12). This temperature will be taken as the reference value for the following optimization.

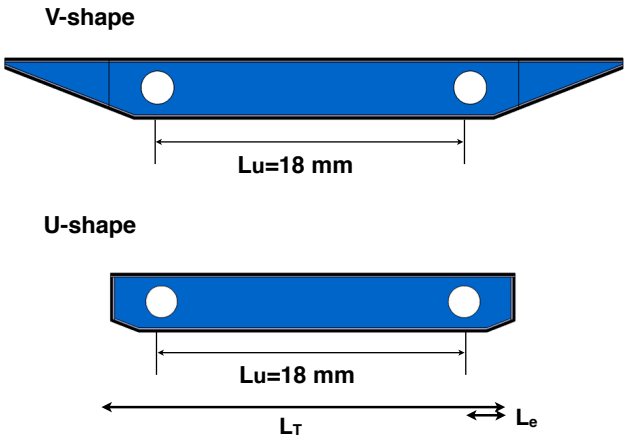

Figure 4.11: The structure profiles at the bottom of the mountain: V-shape (top) and U-shape (bottom).

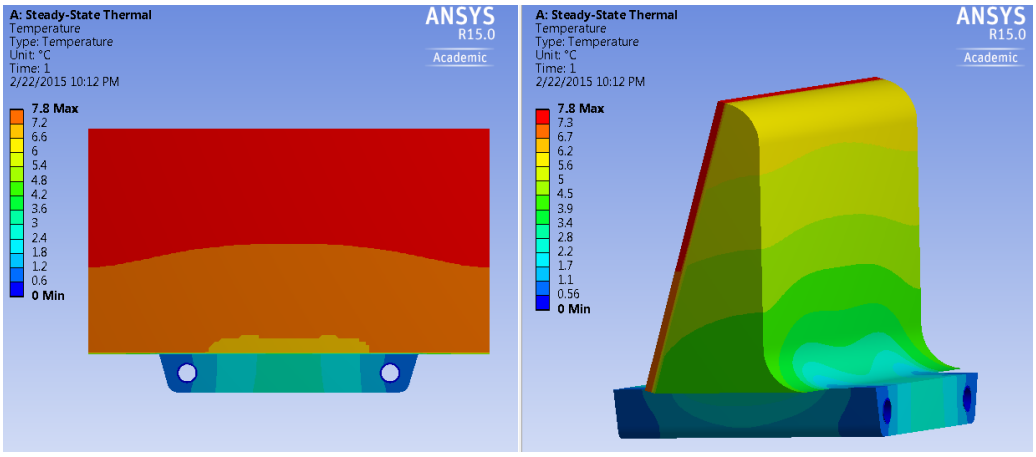

Figure 4.12: Temperature distribution on the sensor. The U-shape structure at the base of the mountain is used and an inclination of the sensor or 74 ^{o} is assumed.

4.4.3 Optimization of the distance between in-going and out-going pipes

The small amount of carbon foam on the external sides (L_e, in Figure 4.11) of the cooling pipes in the U-shape structure may be easily damaged during construction. One way to have more material on the external sides (keeping the constant total length (L_T)) is to reduce the distance L_u between the in-going and out-going cooling pipe. However, if the cooling tube is bent with a too small radius, the tube wall thickness at the bending becomes thinner and may cause a

break under high fluid pressure. This concern requires further study since a different value of L_u may result in different thermal performance.

The value of L_u is varied from 8 mm to 18 mm. The temperature difference (with respect to the tube wall) on top of the mountain as a function of L_u is shown in Figure 4.13. The effect is found to be small. The minimum of the curve is reached for $L_u \sim 14$ mm. A value of 16 mm is selected and verified to be feasible by a manufacture procedure and a pressure test up to 300 bar.

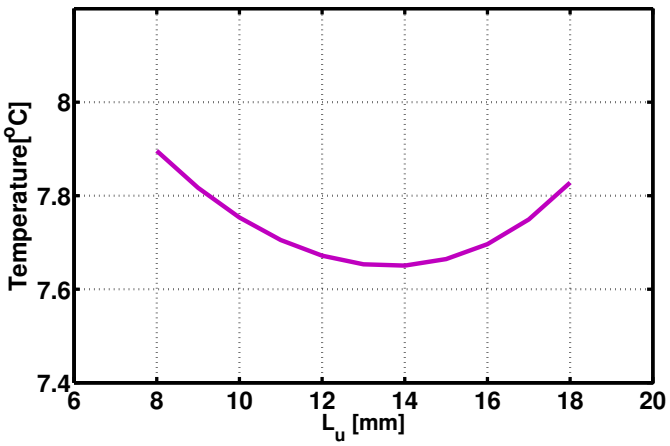

Figure 4.13: Optimization of the distance between the in-going and out-going pipe

4.4.4 Optimization of the foam cut

So far, the way of implementing the tube inside the carbon foam is not considered. When the carbon foam is cut and opened to insert the cooling pipe, extra glue is needed to seal the pipe and the carbon foam. Any extra material is not desirable, not only in order to reduce the amount of material, but also to optimize the thermal performance.

Three types of foam cuts are proposed, referred as vertical, horizontal, and groove cut, as shown in Figure 4.14. The dark gray parts in the Figures represent the surface along which the cut is performed. The vertical cut implies to cut the carbon foam both on mountain and on the base. The horizontal cut implies to cut the foam only at the base. This approach is

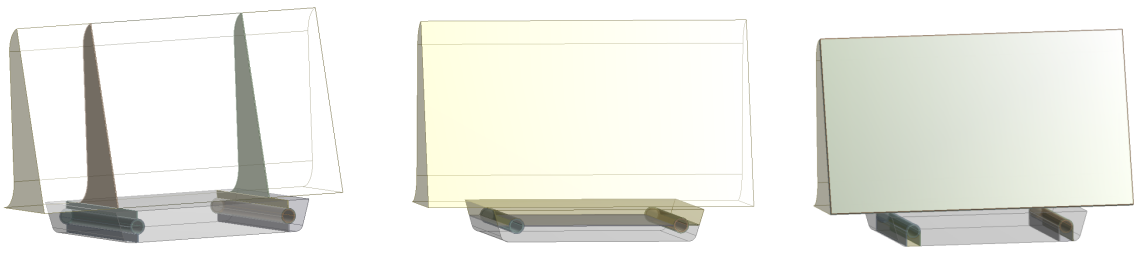

Figure 4.14: Vertical cut (left), horizontal cut (middle) and groove cut(right)

easier to realize, but the horizontal layer of glue may decrease the thermal performance due to the lower thermal conductivity of the glue compared to that of the carbon foam. The third method of implementing the cooling pipe in the stave is called groove cut. The cooling pipe is embedded directly in the carbon foam, after which the glue is applied to seal the empty parts in the structure.

In order to verify which method of cutting the foam has the minimal effect on the thermal performance, the temperature distribution at the top of the mountain is simulated and the results are listed in Table 4.5 assuming a glue thickness of 0.1 mm. The difference with respect to the ideal case of no foam cut is small, ranging from 0.1 °C to 0.4 °C . Even though the groove cut induces the highest temperature difference at the top of the mountain, this cut is selected to produce the mechanical prototype based on its simplicity to insert the cooling pipe.

Table 4.5: Temperature difference at the top of the mountain with different foam cuts assuming a glue thickness of 0.1 mm

Method	$\Delta T_{Support}$ [°C]
No foam cut	7.8
Vertical cut	7.9
Horizontal cut	8.1
Groove cut	8.2

The procedure of producing a full prototype of 1.2 m in length is illustrated in Figure 4.15. It proceeds in three steps. In step 1, the carbon foam is machined with barrel and mountain regions. As it is shown, there are empty space between mountains according to the optimization results. Step 2 is to groove the carbon foam at the bottom of the base support. In step 3, the pipe is glued and sealed with carbon fiber reinforcement plate to provide the mechanical stiffness. A picture of a mechanical prototype of the support structure produced

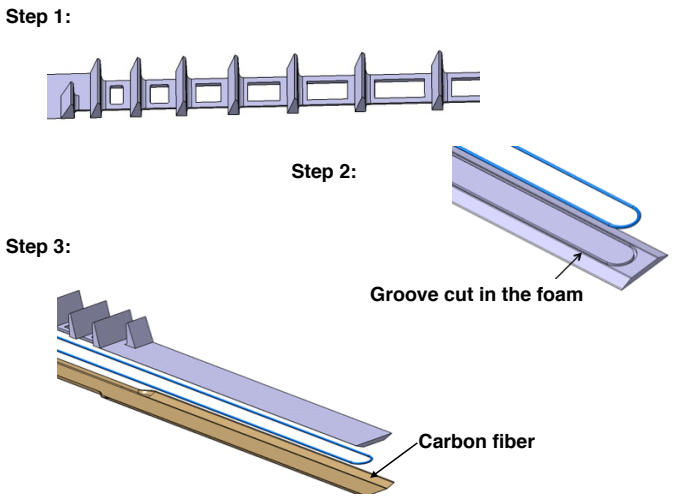

Figure 4.15: Manufacture procedure of the 1.2 m long mechanical prototype.

by the company "Composite Design, Groupe ORECA" in Switzerland is shown in Figure 4.16. This prototype is built to test the construction procedure and the mechanical properties of the support structure.

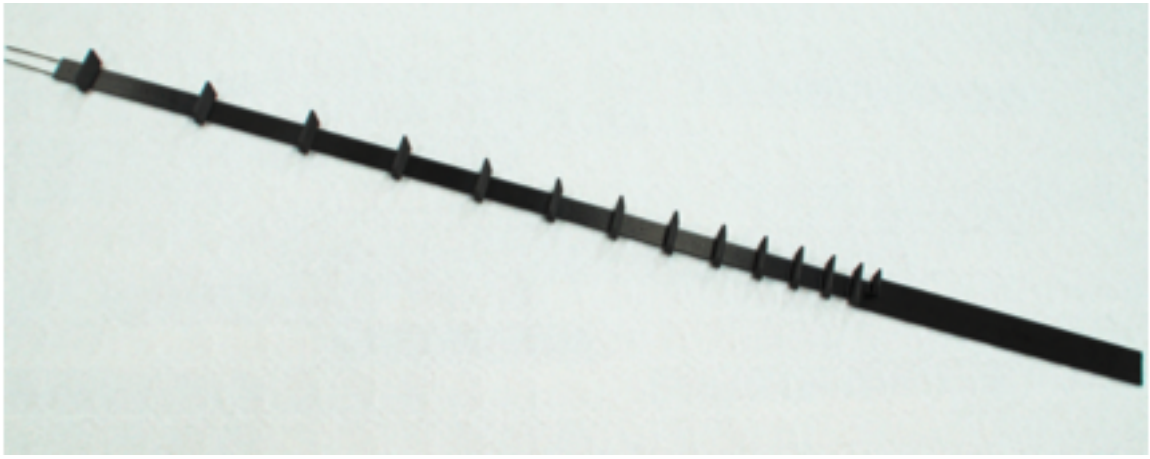

Figure 4.16: Picture of the mechanical prototype

4.5 Choice of materials

4.5.1 Temperature distribution study

The analysis presented in Section 4.4 is repeated assuming a power density of 0.7 W/cm^2 (Layer 0 and Layer 1) with the hypothesis that 80 % of it comes from the read-out chip and 20% from the sensors and the module flex.

Using the same materials as in the previous calculation, the temperature at top of the mountain with respect to the inner tube wall, $\Delta T_{Support}$ is 16.9 °C (see left plot of Figure 4.17). The maximum temperature difference across the silicon sensor ΔT_{sensor} is about 2 °C (see the right plot). From $\Delta T_{Support}$ and the power density, the thermal figure of merit of the local support structure is calculated to be 24 Kcm^2/W. This value is beyond the requirement (shown in Table 4.3), therefore the design must be modified. Since the previous result has shown that the previously considered effects related to the geometry are small, the next study is to consider a change in the materials in order to achieve the described thermal performance.

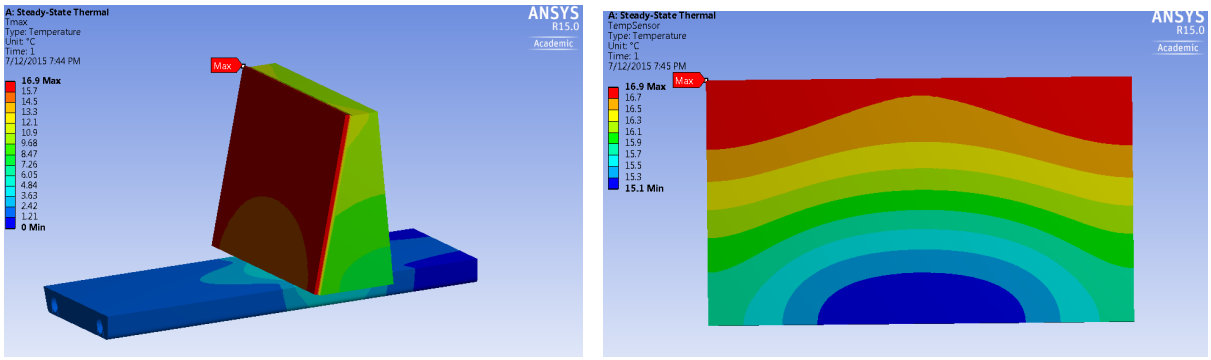

Figure 4.17: Temperature distribution on the local support structure(left) and on the silicon sensor (right) with power density of 0.7 W/cm^2.

The thermal conductivity of the materials, used in the stave controls the thermal performance. In order to evaluate the different contributions to the total thermal resistance from each material between the cooling pipe and the mountain, a geometry path along the heat flux propagation direction is considered and the temperature difference across each material is studied. The definition of the path is illustrated in Figure 4.6 with the red arrows. The path starts at the inner surface of the cooling tube, passing through the layer of glue to reach the

carbon foam. Afterwards, it crosses the glue layer on the mountain area, the face-plate (fp), the parylen (pl), the grease (gre), the chip and finally reaches the silicon sensor. The temperature distribution along this path for the initial choice of materials is presented in Figure 4.18. As seen, the main contribution to the total temperature variation along the path are the variations across the glue and the face-plate. The parylen is the third contributor to the total thermal resistance.

The above analysis indicates that the materials that may improve significantly the thermal response are the material of the face-plate and of the glue[1]. Before calculating the results using more appropriate materials, the effect of the thermal conductivity of the face-plate and the glue is investigated. In the study, first the thermal conductivity of the face-plate is changed, then the thermal conductivity of the glue. All the other materials are kept the same.

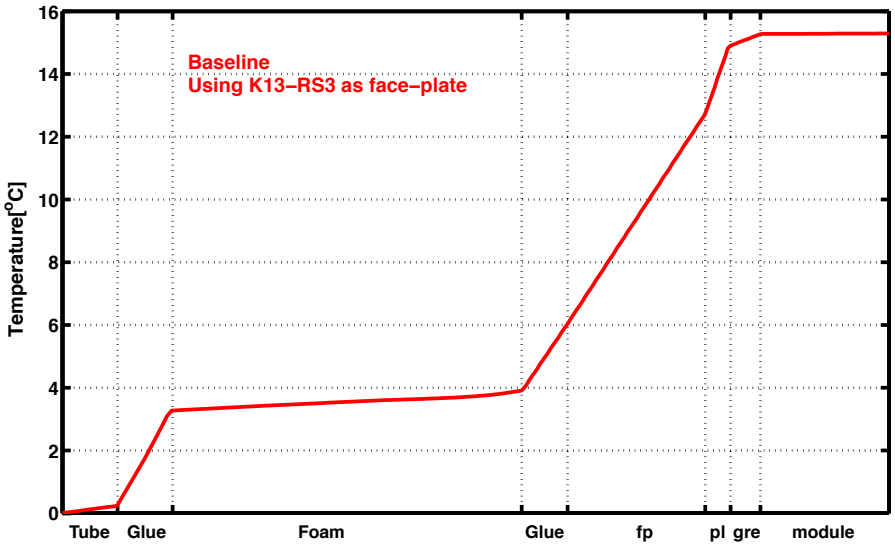

Figure 4.18: Temperature contribution along the thermal path.

4.5.2 Face-plate study

The thermal conductivity Kx ("in-plane" direction, along the mountain slope), Ky ("in-plane" direction, orthogonal to x) and Kz ("through-plane" direction) of the face-plate are treated as input parameters and investigated independently. The output observables are the maximum (Ts_{max}) and minimum (Ts_{min}) temperatures on the silicon sensor (top and bottom). These temperatures have to be interpreted as temperature difference with respect to the temperature of tube wall, as previously explained.

As most of the materials under investigation are carbon-graphite based, the heat conductivity in-plane can reach more than 1000 W/m·K, while the through-plane conductivity is normally lower, around 10 W/m·K. This will be the range considered for the parameter under study. When one of the three parameters, Kx, Ky and Kz, is studied the other two are kept fixed at the value shown in Table 4.4 (IBL based). The results are presented in Figure 4.19. The top left plot of the Figure shows that Ts_{max} decreases of 1 °C when Kx is increased to 1000

[1]It was also decided to remove the parylen layer using a different procedure to implement the electronic insulation, but this will not be discussed in this thesis

W/m·K. The plot on the top right of the Figure shows that the changes of Ky has little effects on the temperature of the sensors. The largest temperature variation is related to changes in Kz. When Kz goes from 0.5 W/m·k to 5 W/m·k, Ts_{max} decreases by almost 4°C. The conclusion is that a material which has a thermal conductivity in plane above 1000 W/m·K and through-plane above 5 W/m·K would be a better candidate for the face-plate.

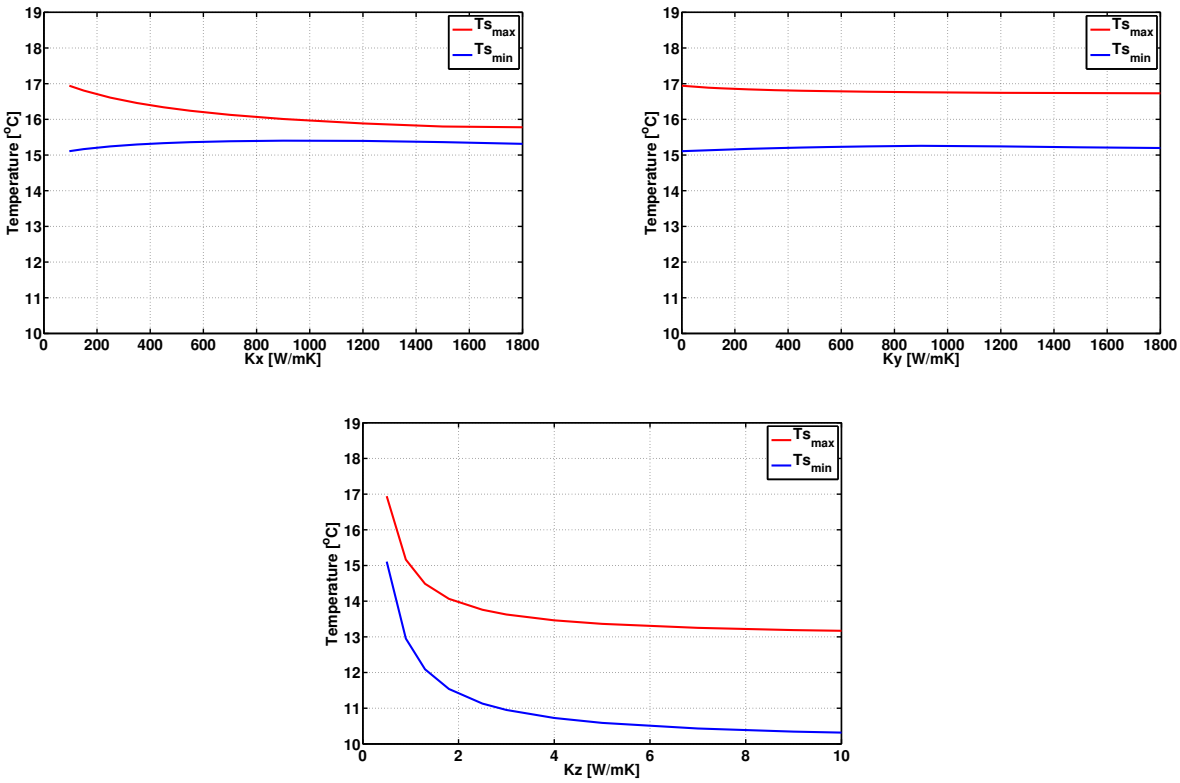

Figure 4.19: The maximum and minimum temperature on the sensor as function of the faceplate thermal conductivity, Ky (top left), Kx (top right) and Kz (bottom).

Two candidates, Thermal Pyrolytic Graphite (TPG) [82, 83] and ThermalGraph [84] are considered as new materials for the face-plate. TPG is a form of pyrolytic graphite manufactured from the thermal decomposition of hydrocarbon gas in a high temperature chemical vapor deposition reactor. ThermalGraph is manufactured from a naturally occurring allotrope of Carbon. It has not only a very high thermal conductivity but it is also flexible and is available in roll or sheets. These two materials have in-plane thermal conductivity over 1500 W/m·K, which is 10 times higher than that of the previously considered material for the face-plate, K13C/RS3. They can provide higher heat transfer efficiency from the top to the bottom of the mountain and a more uniform temperature across the sensors. In addition, the thermal conductivity "through-plane" is above 10 W/m·K, which is a better value for improving the thermal performance of the local support structure as shown in this study. The available minimum thickness of TPG is about 150 μm, while the thickness of ThermalGraph can varies from 30 μm to 300 μm.

4.5.3 Glue study

In this study, the thermal conductivity of the glue (K_{glue}) is the input parameter and its value is changed from 0.5 W/m·K to 10 W/m·K. The corresponding outputs are still Ts_{max} and Ts_{min}. The results are shown in Figure 4.20. When K_{glue} goes from 1.1 W/m·K to 5 W/m·K, the

sensor temperatures decrease by more than 3°C. Therefore, a thermal conductivity of the glue higher than 5 W/m·K also helps to increase the thermal performance.

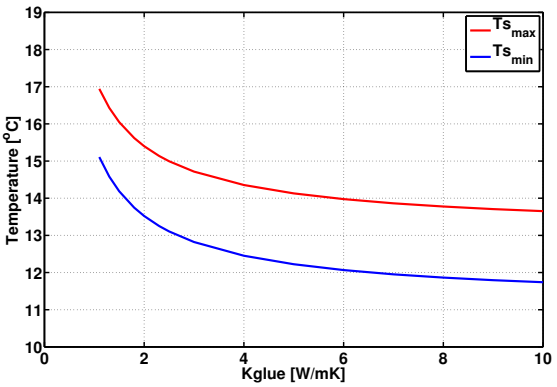

Figure 4.20: The maximum and minimum temperature on the sensor as function of the thermal conductivity of glue.

On the market, a new material based on carbon nano-tubes (CNT)[85] has suscitated attention for developing advanced thermal interface materials. It can provide a thermal conductivity above 5 W/m·K by uniformly dispersing the CNT on a resin material (epoxy). This type of material needs further development for our application and collaboration between the glue manufacturing company and the member of the Alpine stave project is foreseen.

4.5.4 Temperature distribution with new candidate materials

The simulation of the temperature distribution along the thermal path defined in Figure 4.6 is repeated by using the new materials. The results are shown in Figure 4.21 where the blue curve corresponds to the case where a layer of TPG with a thickness of 0.3 mm replaces the K13C/RS3 (Mod.1) and the other materials remain the same as in the baseline design. The geometry is not modified. Compared with the baseline design, the modified design shows that the temperature difference induced by face-plate is decreased by more than 5 °C. A different way of insulating the sensors from the face-plate is considered (called Mod.2) and therefore the parylen layer is removed. This modification reduces the temperature on the sensors by another 2 °C. In addition, a further modification (Mod.3) uses a glue with K_{glue} of 2.5 W/m·K. A new glue with increased thermal conductivity decreases the thermal resistance around the cooling pipe and behind the face-plate and therefore the module temperature is reduced by 2°C .

The value of $\Delta T_{Support}$ and $TFoM_{Support}$ for the four configurations (baseline, Mod. 1, Mod. 2 and Mod. 3) is calculated and listed in Table 4.6. If the new candidate materials are used, the value of $TFoM_{Support}$ can be reduced to 11 Kcm^2/W, which satisfies the thermal requirement for all the layers of the Pixel detector.

4.5.5 Uncertainties from the input parameters

In order to understand the effects of the experimental uncertainties arising from the input parameters on the temperature predictions, few factors have been studied. It is expected that the main uncertainties result from the knowledge of the thermal conductivity of the carbon foam (Kfoam) and from the thickness of the glue around the cooling pipe or behind the face-plate.

- The thermal property of the carbon foam depends on the intrinsic characteristic of its internal structure, the pores. In each production, the internal structure of the foam may

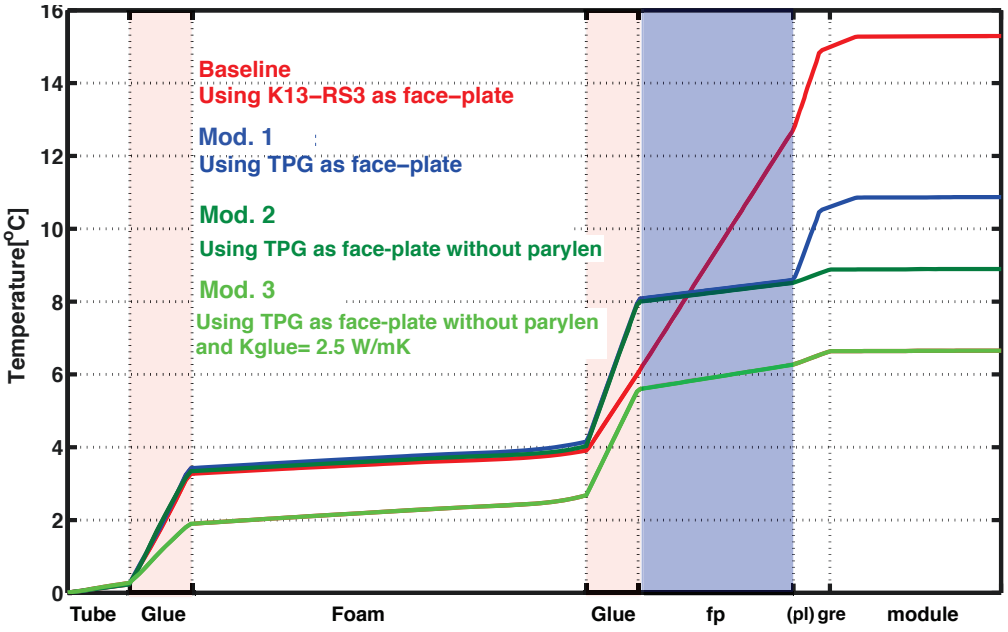

Figure 4.21: Temperature distributions along the thermal path represented in Figure 4.6 for different choice of materials.

Table 4.6: Temperature difference between the top of the mountain and the tube wall and the value of TFoM for different design configurations

Design	$\Delta T_{Support}$[°C]	$TFoM_{Support}$ [Kcm^2/W]
Baseline	16.9	24
Mod. 1	11.6	17
Mod. 2	9.9	14
Mod. 3	7.8	11

change as well as its density. As a result, the thermal conductivity changes. A variation of Kfoam of about 10 % is assumed.

- The thickness of the glue is chosen equal to 0.1 mm. In the production procedure, this thickness cannot be precisely controlled, and therefore significant uncertainties may be present. To investigate the impact of this uncertainty, the thicknesses of the glue layers are varied by 50 %. This results in a $\Delta T_{support}$ variation of ± 0.7 °C and of ± 0.3 °C for the layer around the tube wall and behind the face-plate, respectively.

In addition to the uncertainties mentioned above, the variation of the thickness of the grease and the face-plate are also considered but the results have a negligible effect. Finally, to evaluate the stability of the FEA calculation, the size of the meshed element is also varied. The results due to the variation of each parameter are listed in Table 4.7, the combined total uncertainty, (evaluated as the sum in quadratic of each contribution) is about ±1.1 °C.

Table 4.7: Estimated uncertainty on the result for the considered variations in the simulation

Parameters	Value		$\Delta(\Delta T_{Support})$ [°C]
Kfoam [W/m·K]	40	±5	∓0.7
Thickness of glue around pipe [mm]	0.10	±0.05	±0.7
Thickness of glue behind face-plate[mm]	0.10	±0.05	±0.3
Thickness of TPG [mm]	0.30	±0.02	±0.02
Thickness of grease [mm]	0.10	±0.02	±0.002
FEA element size [mm]	0.03	+0.06	−0.16
Total estimated uncertainty			± 1.1

4.6 Design of the evaporator

The Alpine stave uses a two-phase CO_2 cooling system to dissipate the heat generated by the sensors, readout chips and the flex. The optimization of the cooling pipe, which acts as an evaporator is detailed in this Section.

An evaporator in a two-phase cooling system uses the evaporation process of the coolant to efficiently remove the heat load. Since the evaporator in tracking detectors must be integrated within the local support structure in order to have an efficient cooling capability, it consists practically of a cooling pipe which is very often embedded inside the support structure. The cooling pipe of the Alpine Pixel detector is a circuit with a U-turn embedded inside the stave. It is required that the evaporator introduces a minimal amount of material. This requirement is satisfied by using pipes with the smallest diameter capable at the same time to maintain a uniform temperature across the modules.

As discussed in Chapter 3, the use of a long pipe with a small tube diameter may produce a high pressure drop and therefore a high temperature gradient along the path of the cooling circuit. In the following subsection, the CoBra program is used to study the operation parameters of the cooling system of the Alpine stave, like the tube diameter, the mass flow rate of the CO_2, the effect of the local heat flux and the fluid flow pattern inside the evaporator. The full stave is simulated (not only a single mountain).

4.6.1 Preliminary optimization of the tube diameter

The CoBra program described in Chapter 3 is used to optimize the size of the tube diameter of the cooling pipes of the Alpine staves taking into account the requirements presented in Table 4.3. The optimization is done with the following assumptions:

- The heat load is assumed uniformly distributed along the cooling pipe. A more precise distribution of the heat flux will be studied later as a further improvement to this assumption.
- Since the stave has a symmetry with respect to the median axis perpendicular to the flux direction, the heat flux from the modules and flex are evenly distributed between the in-going and out-going pipes.
- The temperature gradient along a two-phase cooling pipe is expected to be relatively small, therefore the heat-exchange between the in-going and out-going pipe sections is neglected.

The results of the calculations for the three layers are illustrated in Figure 4.22 and Figure 4.23. The mass flow rate is fixed at 2 g/s. For each plot, three temperature differences are plotted: ΔT_{dP} is the temperature difference between the CO_2 at the beginning of the in-going pipe and at the end of the out-going pipe, ΔT_{HTC} is the temperature difference between the inner tube wall and the local CO_2 evaporation temperature at the beginning of the in-going pipe. The sum of ΔT_{dP} and ΔT_{HTC}, ΔT_{Total}, represents a quantity which characterizes the intrinsic temperature gradient within a single stave. The volumetric heat transfer coefficient (HTC_{VOL}) is also plotted on the same plot. It is calculated by dividing the total dissipated power (shown in Table 4.2 and called heat load per stave) by ΔT_{Total} and by the total volume of CO_2 inside the pipe. It characterizes the cooling ability of the system for a given volume of coolant. It is the parameter to maximize in this study.

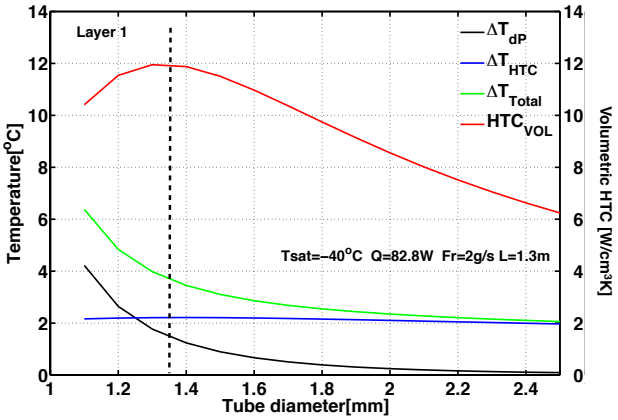

Figure 4.22: Results of the preliminary optimization of the tube diameter for Layer 1

Figure 4.22 shows that the maximum of the HTC_{VOL} is reached for a tube diameter of 1.3 mm for Layer 1. The same calculations are carried out for Layer 2 and 3. The optimal tube diameters are 1.6 mm and 1.9 mm, respectively. The above calculation provides a baseline result

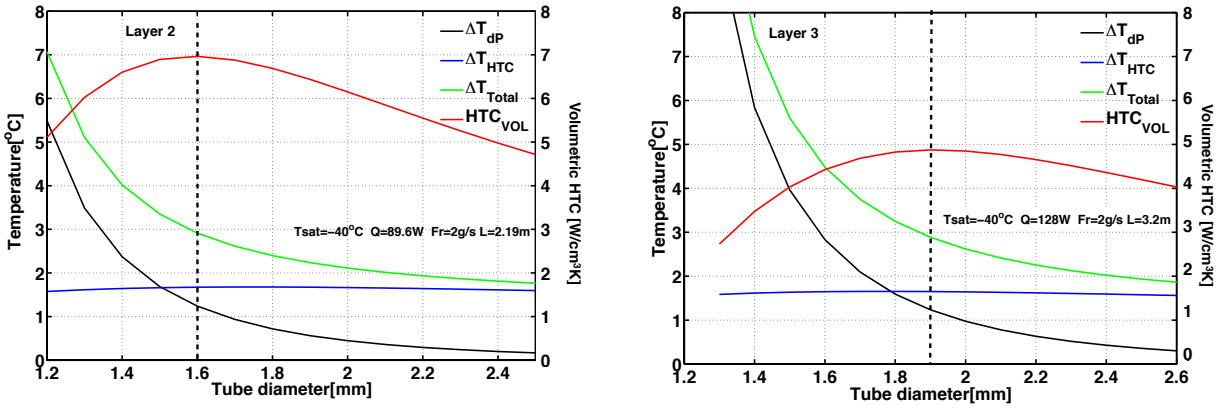

Figure 4.23: Results of the preliminary optimization of the tube diameter for Layer 2 and Layer 3.

for choosing the optimal tube diameter. In order to make a final decision, other aspects need to be taken into account, such as the complete material budget, the manufacture procedure, the resistance to the fluid pressure, etc. Since the use of different cooling pipe diameters in the

different pixel layers complicates the constructions, a diameter of 1.5 mm for Layer 1 and 2 is being considered at present. The tube diameter for Layer 3 is not yet decided.

4.6.2 Effect of the mass flow rate

In the above calculation, a fixed mass flow rate of 2 g/s is used. In two-phase evaporative systems, the flow rate mainly impact the vapor quality. This in turn affects the local heat transfer coefficient and the temperature drop across the flow path. A lower flow rate means lower heat transfer efficiency leading to higher temperature on the wall of the cooling pipe. On the other hand, a high flow rate may induce an excessive pressure drop in the pipe which does not guarantee a good temperature uniformity within the stave. Thus the effect of mass flow rate on the choice of optimal tube diameter is investigated.

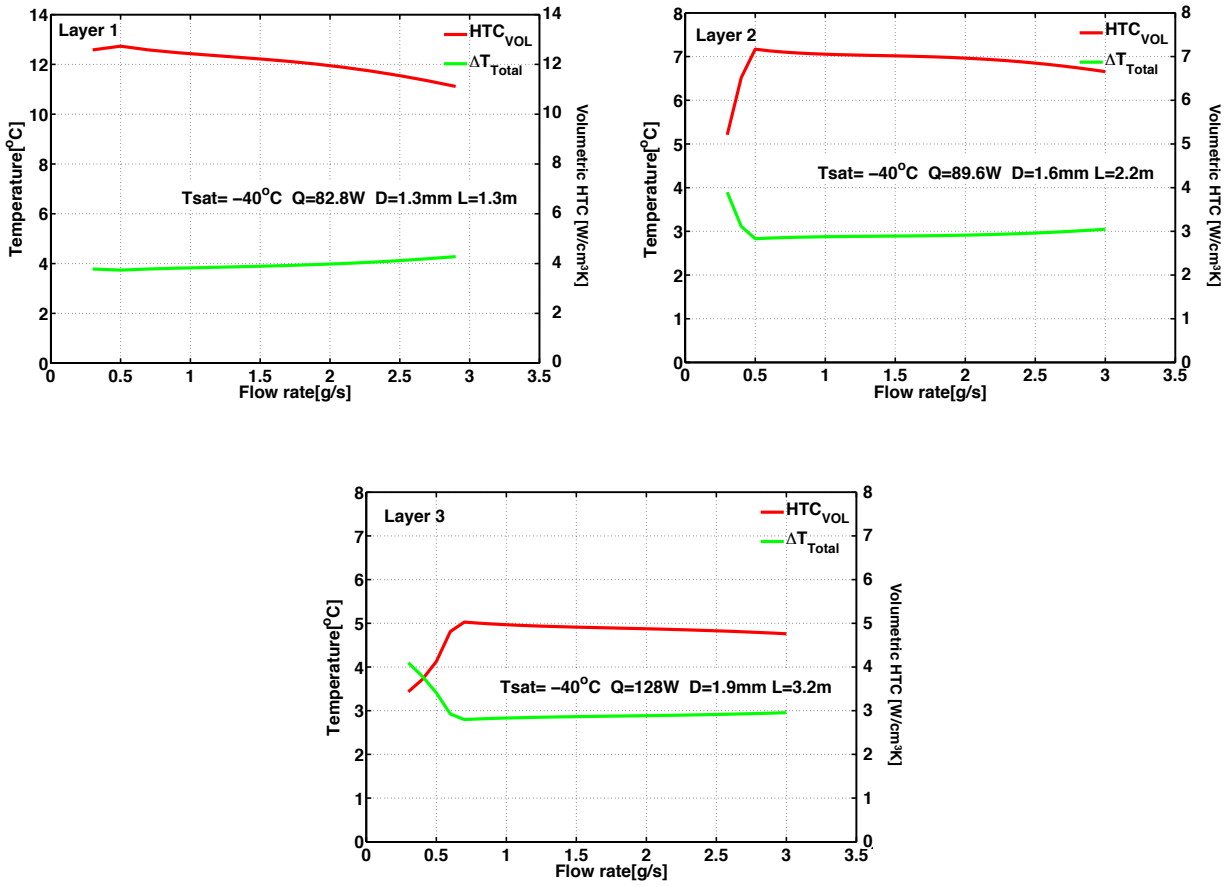

Figure 4.24: Volumetric heat transfer coefficient and temperature difference ΔT_{total} as function of the mass flow rate.

Figure 4.24 shows HTC_{VOL} and ΔT_{Total} as a function of the mass flow rate for Layer 1, 2 and 3 with the tube diameters as obtained by the optimization described in the previous section. The result for Layer 1 shows that the ΔT_{Total} changes very little when the mass flow rate varies from 0.3 g/s to 3 g/s. The changes of HTC_{VOL} is also small staying within 10%. This indicates that the preliminary optimal tube diameter is valid for a wide range of mass flow rate. The results for layer 2 and layer 3 show a similar trend after a flow rate of 0.5 g/s and 0.7 g/s respectively.

The variation of ΔT_{Total} as a function of flow rate can be understood when separating the behavior of the two components ΔT_{HTC} and ΔT_{dP}, as illustrated in Figure 4.25 using Layer 3

as an example. When the flow rate is increased, ΔT_{HTC} decreases due to the increase of CO_2 evaporative local heat transfer coefficient as described in Chapter 3. On the contrary, the ΔT_{dP} increases due to an increased pressure drop along the flow path. The combination of these two phenomena produces transition region (around $\approx$ 0.5 g/s for Layer 2 and $\approx$ 0.7 g/s for Layer 3, see Figure 4.24), where ΔT_{Total} reaches a minimum. In Layer 1 the minimum of ΔT_{Total} is reached at a lower value of the flow rate and therefore does not appear in the Figure.

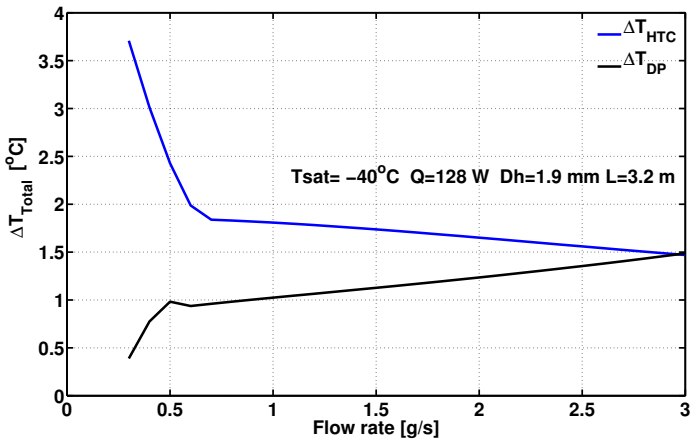

Figure 4.25: Temperature differences due to pressure drop and to the local heat transfer for Layer 3 as a function of the flow rate.

Based on the above analysis, a flow rate above 0.5 g/s will be considered for all pixel layers. Further investigation on the upper limit of the mass flow rate will be discussed later.

4.6.3 Effect of the local heat flux

The total heat load is assumed equally distributed along the cooling pipe in the above calculations. This is the case for the Alpine stave barrel region, but it is a rough simplification for the mountain region where the heat load comes from the discretely located modules along the stave. The effect of the local heat flux distribution is studied in this section.

Figure 4.26 (left) shows a heat flux through the pipe wall of 1.55 $\times 10^4$ W/m^2 as a function of length (L) along the flow direction according to the uniform distribution assumption. The right plot on the same figure shows the heat flux according to actual location of modules along the stave[2]. The heat flux through the pipe wall in the mountain region reaches up to 2.6$\times 10^4$ W/m^2. The heat flux in the barrel region shows a similar value as the uniform heat flux. The non instrumented regions in between the mountains show no heat flux (the heat load from the stave flex is neglected).

The variation of the heat flux along the pipe affects the local heat transfer process. To investigate in detail the two-phase system properties, the temperature and the pressure distribution are studied as function of the length along the flow direction. The two heat flux scenarios (uniform and non-uniform) are compared in Figure 4.27 for Layer 1. The top plot shows the results with a uniform heat flux, the bottom plot shows the results with discretely distributed heat flux in the mountain region where 2.3 W (see Table 4.1) of heat load per chip is applied. In this simulation a total length under the mountain is 20 mm (this value corresponds to d_1+d$_2$+d$_0$, see Figure 4.10).

[2]The behavior of the local heat flux through the pipe wall appears different in Figure 4.26 compared to Figure 4.9 since the former figure uses the CoBra program while the latter figure is done using FEA simulation.

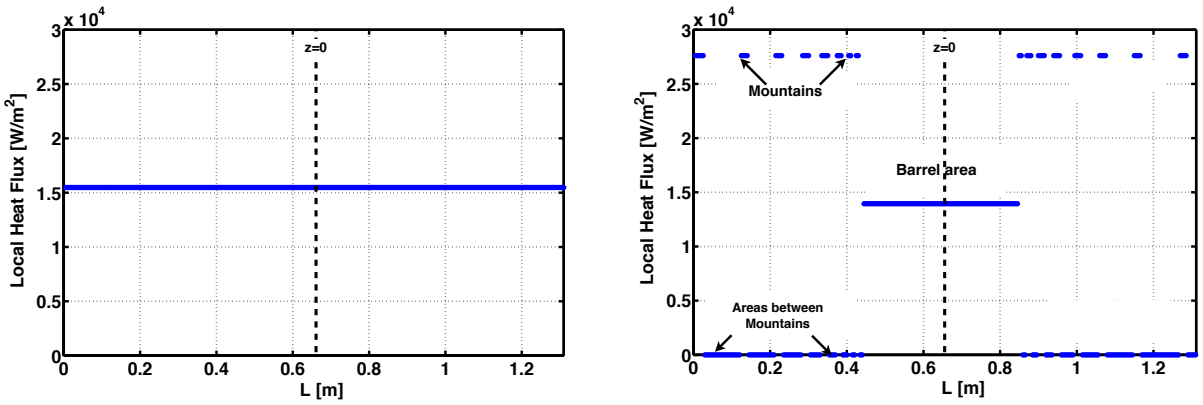

Figure 4.26: Uniform heat flux(left) and non uniform heat flux (right) along the cooling pipe for Layer1 using 1.3 mm tube diamter at -40 °C, with mass flow rate of 2g/s.

Few important features are observed:

- In both plots, starting from position at L=0 mm where the CO_2 in the liquid stave enters into the stave, the temperature of CO_2 and the tube wall gradually increase until the CO_2 enters into liquid-vapor two-phase when the saturation temperature is reached.

- After that the saturation temperature is reached and the CO_2 begins to evaporate, the temperature along the flow path begins to decrease due to the pressure drop. For the case of a uniform heat flux, with a mass flow rate of 2 g/s, the total induced pressure drop over a length of 1.3 m is about 0.6 bar when the outlet pressure is fixed as P_{sat}=10 bar. The non-uniform heat flux scenario produce a smaller pressure drop at 0.5 bar.

- The maximum local temperature difference (ΔT_{HTCMAX}) in the two-phase region with non-uniform heat flux is 3°C and is 1°C higher compared to the case of uniform heat flux. This shows that the temperature difference with uniform or non-uniform heat flux in the mountain is not very different even though the local heat flux (shown in Figure 4.26) in the latter case is almost two times higher. This is thanks to the high local HTC of evaporating CO_2.

- The advantage of a two-phase heat transfer process is visible comparing the temperature of the tube wall before and after that the CO_2 reaches the two-phase state. Shortly before the CO_2 reaches the two-phase, for the non-uniform heat flux case, on the second module, due to the low HTC of single phase heat transfer, the tube wall temperature is more than 1°C higher than the neighboring modules. To reduce such temperature gradient, a general approach is to have pre-boiled CO_2 flow prior to the entrance to the evaporator. The results corresponding to this case are shown in Figure 4.28. In this configuration, the pre-heating delivers 6 W to the CO_2 bringing the liquid into two-phase state at the entrance of the evaporator with a small vapor quality of 0.002. As seen, the temperature at the entrance of the pipe is reduced. According to the calculations, 6 W is the minimum pre-heating required for the three layers. A pre-heating less than 6 W will not be sufficient to bring CO_2 into two-phase state. In conclusion, to have a boiled CO_2 at the inlet of the stave is important to avoid a temperature peak on the first few modules at the entrance of the pipe.

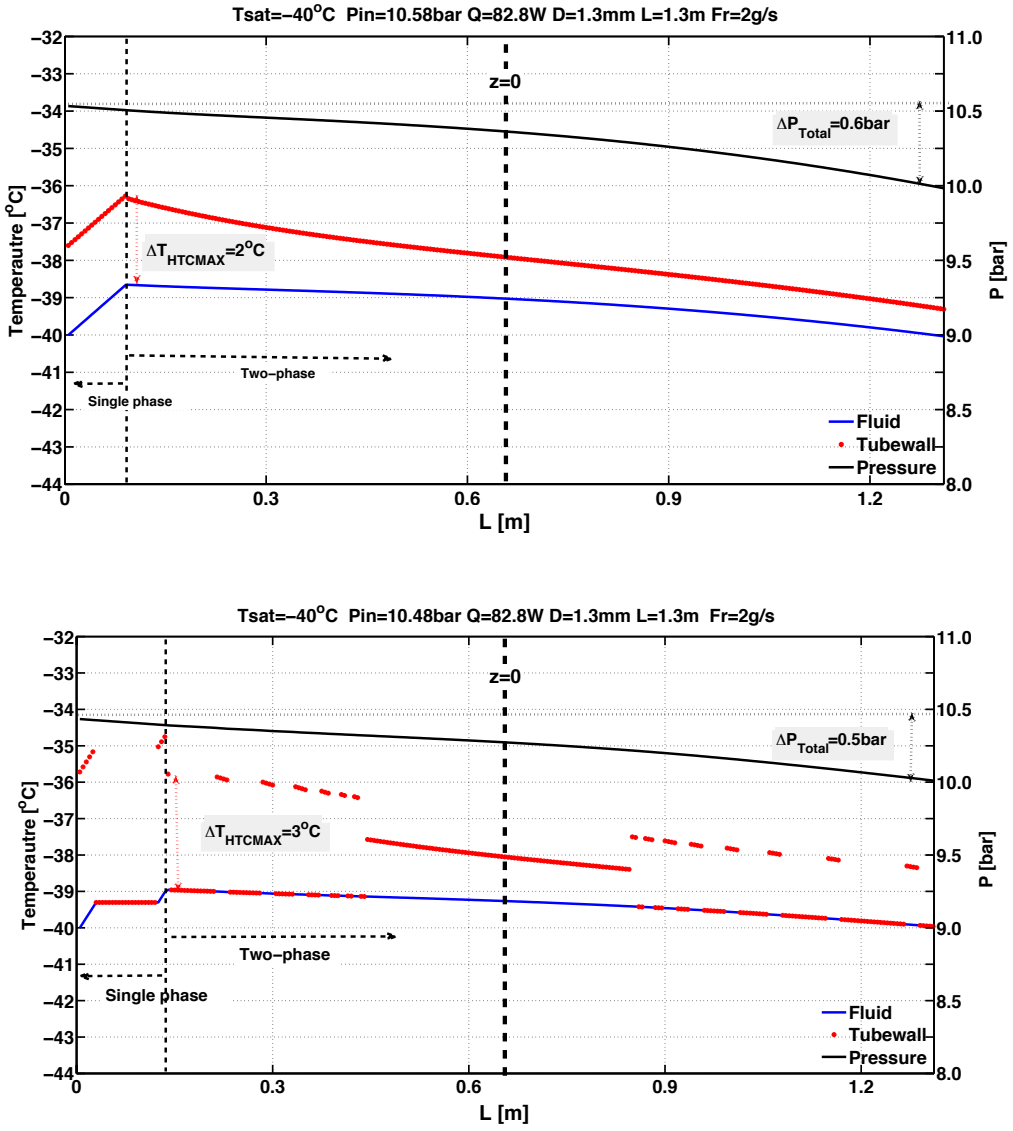

Figure 4.27: Temperature and pressure distribution along the cooling pipe of the stave of Layer 1 with 1.3 mm tube diameter under uniform heat flux (top) and non-uniform heat flux (bottom) at -40 °C with a flow rate of 2 g/s. The temperature of the fluid is represented in blue while the temperature of the tube wall is in red.

4.6.4 Flow pattern in the evaporator

The flow pattern is one of the key characteristic of a two-phase flow cooling system since it impacts its heat transfer capability. It is desired to stay within the Annular flow regime since this regime has the highest heat transfer coefficient compared to the other flow regimes. A safety margin is required to make sure that the system is far from the dry-out, the stratified or stratified-wavy flow regimes where the temperature of the tube wall is higher due to a low HTC. As described in detail in Chapter 2, for a given tube diameter, CO_2 working temperature, and under a given heat flux, different flow pattern are observed for different vapor qualities.

To understand quantitatively the optimal flow rate range, flow pattern maps are calculated for the three pixel layers assuming a saturation temperature of the cooling fluid of -40°C. The tube diameters for the three layers are selected according to the preliminary optimization. The results are presented in Figure 4.29. On the plots the blue dashed lines represent different

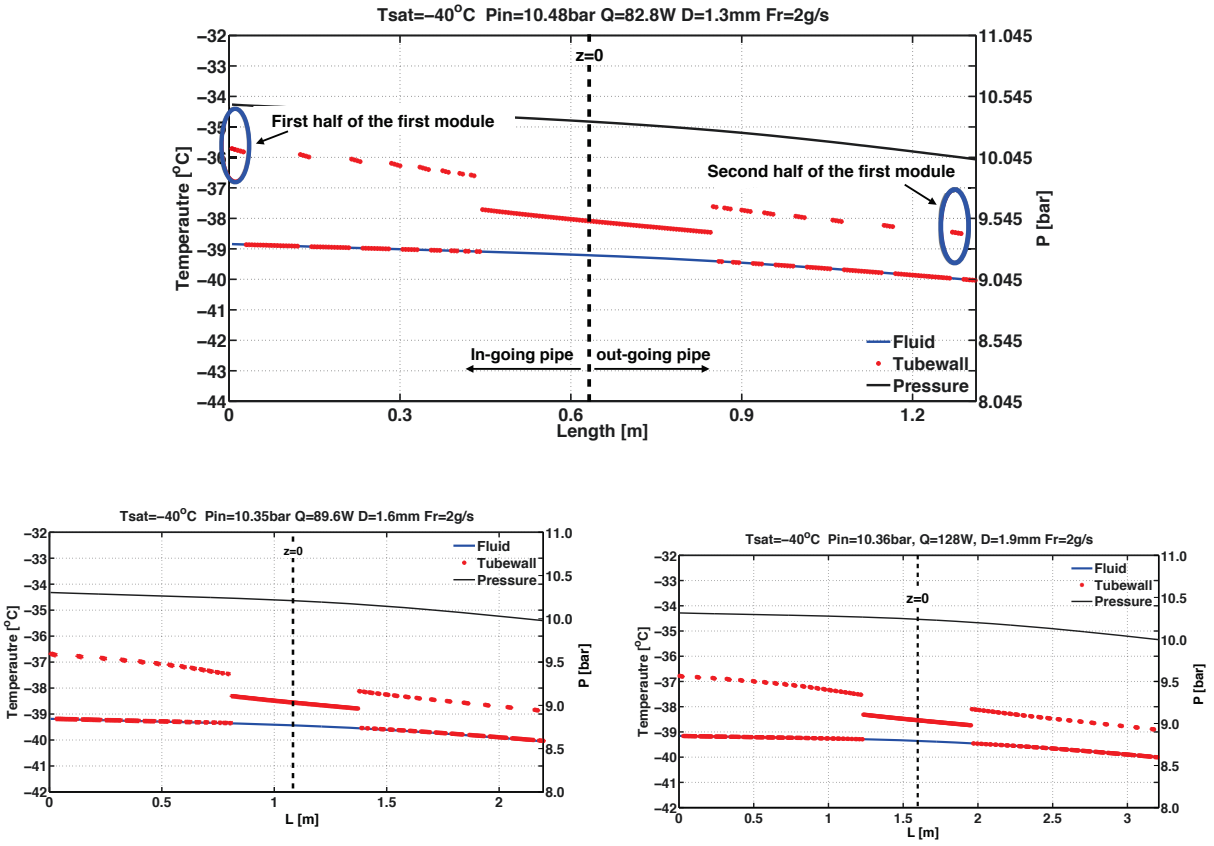

Figure 4.28: Temperature and pressure distribution along the flow direction for Layer 1 (top) Layer 2 (middle) and Layer 3 (bottom). 6W is used to preboil the CO_2 into two-phase state.

values of mass flow rate between 0.5 g/s to 3 g/s. These lines end when the coolant reaches the outlet of the cooling pipe.

For Layer 1, when the mass flow rate is 0.5 g/s, the vapor quality at the outlet of the cooling pipe is 0.35. Along the flow path, the flow patterns includes Intermittent and Annular flow. Increasing the mass flow rate, the outlet vapor quality decreases and as a result the annular flow regime constitute a smaller fraction. When the flow rate is above 2.0 g/s, the outlet vapor quality of the cooling pipe is less than 0.1, the coolant stays in Bubble flow regime and does not enter into the Annular regime. In this case, the cooling efficiency of the evaporator is not optimal. A complete investigation of the three layers shows that the flow rate should be within 0.5 g/s to 2 g/s in order to maintain an optimal heat transfer efficiency.

It is worth to point out that in the final cooling loop, for simplicity of operation, the flow rate of each stave cannot be adjusted individually. Instead, the mass distribution of the fluid from a main cooling pipe into sub-branches needs to be studied in detail and carefully chosen in order to make sure that the flow rate requirement for each branch is satisfied. As discussed in Chapter 3, capillary tubes with optimized dimension should be deployed upstream of the inlet of the evaporator to uniformly distribute the mass flow rate.

4.7 Temperature uniformity on the sensors

As mentioned in Section 4.6.1, the heat exchange between the in-going and out-going part of the cooling pipe is neglected. The impact of this assumption on the temperature uniformity within a single module is investigated using the FEA simulation. It is expected that the difference

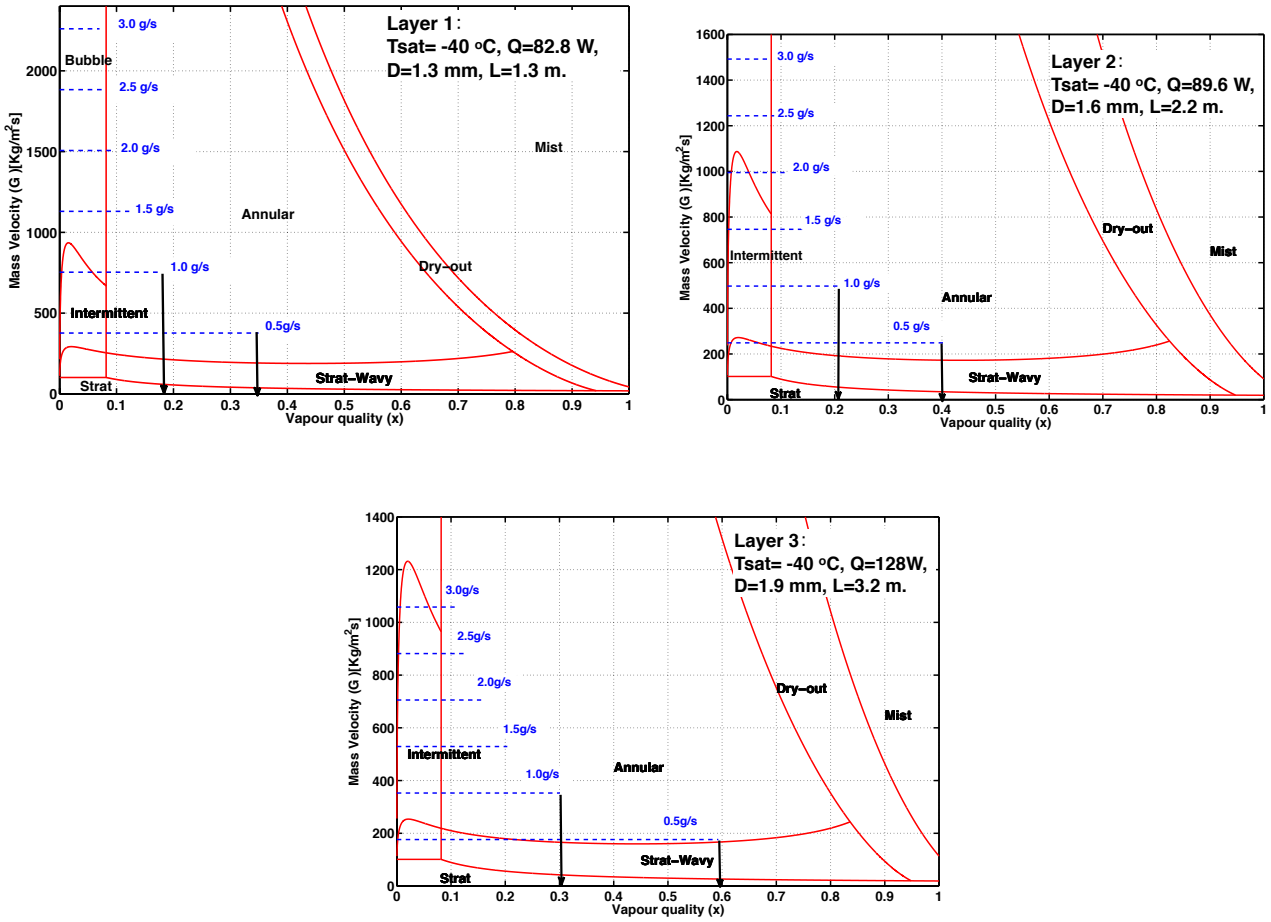

Figure 4.29: Flow pattern map of Layer 1, 2 and 3 for a saturation temperature of -40 °C . The tube diameters are 1.3 mm, 1.6 mm and 1.9 mm, respectively.

between the temperature of the fluid flowing in the in-going and out-going pipe is maximum in correspondence of the first mountain.

In Figure 4.28 the first plot, the two regions highlighted by the blue circles indicates the temperature of the tube wall in correspondence of the first mountain. The circle on the left corresponds to the temperature of the wall of the in-going pipe, the circle on the right corresponds to the temperature of the wall of the out-going pipe. As it is shown this temperature difference is ~ 3 °C .

In order to study the temperature uniformity within the first sensor, various temperature difference between in-going and out-going pipe internal wall is applied using FEA simulation. The layout with TPG as face-plate, with parylen layer moved out and with thermal conductivity of the glue equal to 1.1 W/m·K is studied. The left plot shows that the ΔT_{sensor} slowly increases when the temperature difference between the fluid in the in-going and out-going pipe increases. Compared to the case of no temperature difference between the in-going and out-going cooling pipes, a 3°C temperature difference increases the sensor temperature non-uniformity of the temperature distribution at the sensor by 1.2 °C. The result of FEA under 3°C of temperature difference between the in-going and out-going pipe is shown in Figure 4.30 (right).

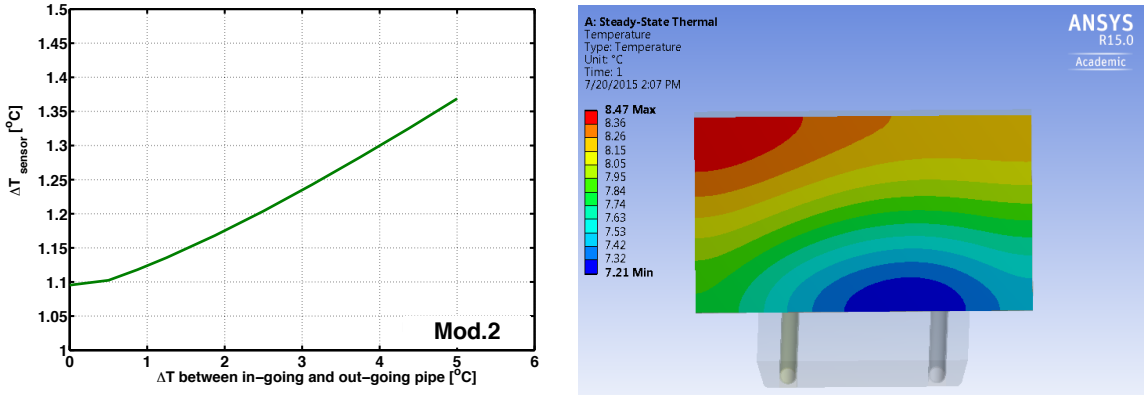

Figure 4.30: Maximum temperature difference within a silicon sensor as function of the temperature difference between the in-going and out-going pipe wall. The configuration of Mod. 2 described in Figure 4.21 is used.

4.8 Summary

The Alpine layout has mountain-like structure which represents a mechanical and thermal engineering challenge. A baseline stave structure is proposed and developed. The local support structure and the evaporator of the Alpine Detector for the Pixel detector is developed concentrating on the thermal performance using Finite Element Analysis and a numerical two-phase heat transfer model. In accordance to the latest power density of the detector module design, material investigations had been carried out. Optimization of the local support structure as well as substitution of key component materials are achieved based on this study. Two-phase CO_2 cooling system using the tube embedded in the support structure as the evaporator is used to efficiently remove the heat generated by the detector. Operational parameter of the system, as well as its detailed thermal properties and behavior are studied aiming to optimize the system performance.

Chapter 5

Alpine prototype thermal performance

Several prototypes based on the design described in the previous Chapter were built to verify the design parameters and the thermal performance under actual thermal load and to understand the production feasibility and limitations. The different prototypes are described in Section 5.1 and the evaluation procedure of the thermal performance of the prototypes is expressed in Section 5.2. Section 5.3 summarizes the modeling method for the prototypes. The predictions provide a description of the thermal performance according to the specifications. A CO_2 evaporative cooling system described in Section 5.4 is deployed to carry out the thermal measurements. Section 5.5 presents the measurements results. The comparisons with predictions are presented in Section 5.6. An analysis of the possible uncertainties is performed to understand the main factors affecting the significance of the comparison. Section 5.7 discusses effects which may occur during the production process as well as material effects which have an impact on the thermal performance of the prototypes.

5.1 Alpine prototype

Two types of Alpine prototype were produced. The first type, named as "Proof-of-Concept prototype (PoC)", is produced and tested to prove the concept of the Alpine design and the advantage of using the evaporative CO_2 as cooling system. The measurement of the PoC prototype response is conducted in parallel with the optimization of the design of the Alpine stave. The second type of prototype is manufactured according to the latest geometry and material specifications and is named as "Functional-Demonstration (FD) " prototype. It is used to demonstrate the actual thermal performance of the local support structure in the mountain region of the Alpine stave.

5.1.1 Proof-of-Concept prototype

The PoC prototype is produced by the Institute fur Verbundwerkstoffe (IVW), in Germany. This company has produced the IBL staves for the ATLAS experiment and accumulated a lot of technological knowledge and experience on the stave assembly.

Figure 5.1 a) illustrates the assembling procedure of the PoC prototype. As shown, there are two "mountains" and one barrel region. The carbon foam is composed of two symmetric structures ("Foam 1" and "Foam 2") with a groove for the insertion of a single cooling pipe with a inner diameter D=1.5 mm. The brown regions indicated as "FP1", "FP2", and "FP3" are the face-plate (FP) using carbon-fiber composite as material. The face-plates (FP3 and $FP3_{bis}$) behind the mountains (far from the beam interaction point) are continuous pieces. Their function is to provide stiffness and prevent the stave from mechanical damage. At the

bottom of the carbon foam, there is the main stiffness support structure called Omega. The details of the arrangement of each layer and their material properties are the same as those shown in Figure 4.6 and Table 4.4. The production procedure of this prototype follows the one used for the final IBL stave [10]. Figure 5.1 b) shows the dimensions of the PoC prototype. It is 120 mm long and 19 mm wide. The length of the barrel region is 41 mm and the length of mountain 1 (M1) and of mountain 2 (M2) along the inclined face is 21 mm. The angle of the mountains with respect to the horizontal plane is 68^o.

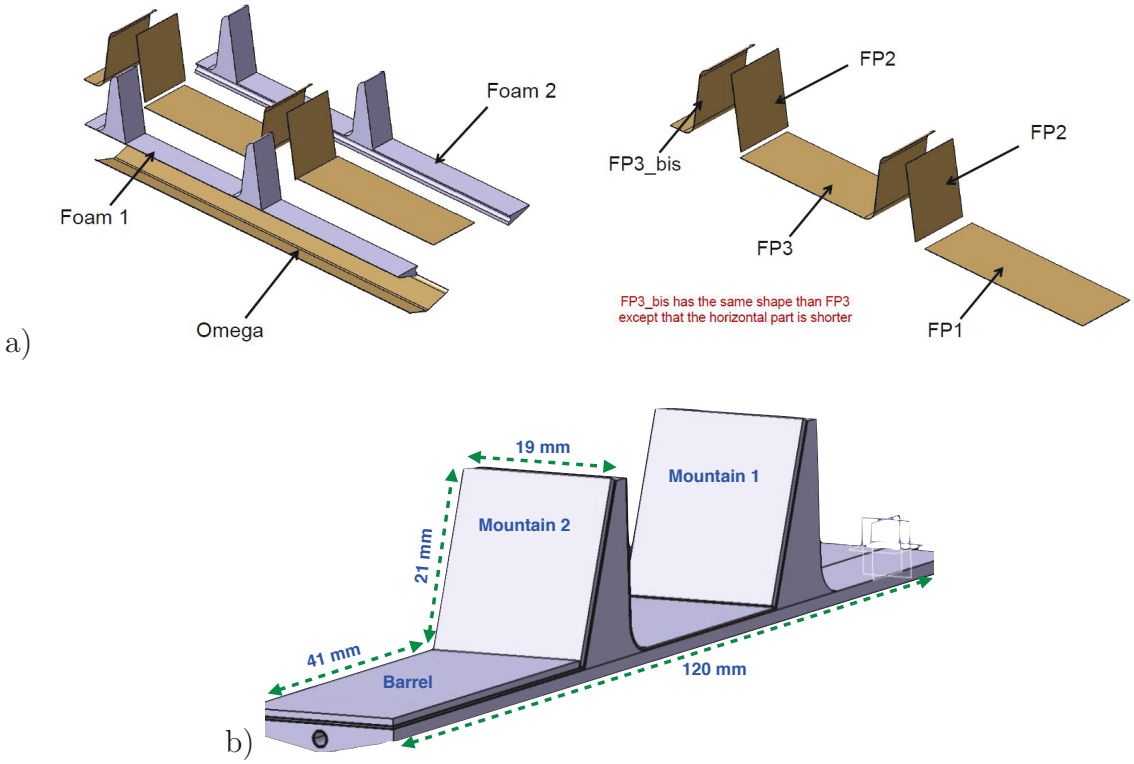

Figure 5.1: a) Illustration of the Proof-of-Concept prototype production procedure. b) Dimentions of the PoC prototype

5.1.2 Functional-Demonstration prototype

FD prototypes are built at the Laboratoire de Physique Subatomique et de Cosmologie (LPSC), in Grenoble (France), according to the optimized design described in Chapter 4. Two FD prototypes are built with different face-plate materials: one uses ThermalGraph (AMEC Thermasol) while the other one uses TPG (MOMENTIVE). The face-plates are used to implement the modules. In FD prototypes, the parylen layer for electronic insulation is removed, two cooling pipes are inserted into the carbon foam and the carbon foam at the external sides of the cooling pipe is partially removed as described in Section 4.4.2. The glue, Stycast 2850FT, is still used as a new glue with higher thermal conductance is not yet available. For sake of simplicity, the FD prototypes have only one mountain.

The two FD prototypes are shown in Figure 5.2. In the "TPG prototype", the TPG material is present only on the mountain region. The high mechanical flexibility of ThermalGraph makes possible to shape it into specific structures and therefore the ThermalGraph material is extended to both the front and the rear of the mountain region.

The dimensions of the two FD prototypes are identical and are presented in Figure 5.3. The base in carbon foam has a width of 22.7 mm and a length of 45 mm. The mountain area (21

Figure 5.2: Pictures of the FD prototypes: The ThermalGraph prototype (left) and the TPG prototype (right).

mm× 36.2 mm) is almost a factor two times wider than in the PoC prototype. The angle of the mountain with respect to the horizontal plane is 72^o. The inner diameter of the cooling pipes is 1.5 mm.

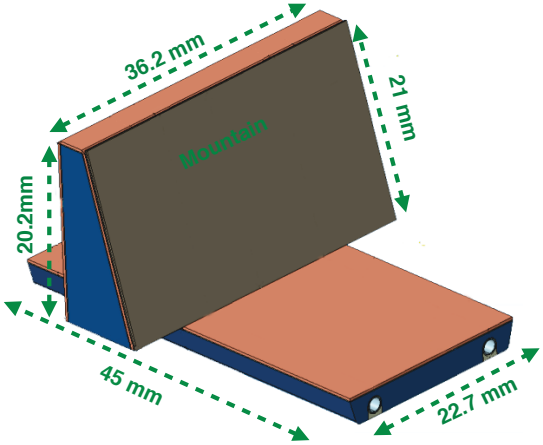

Figure 5.3: Dimensions of the Functional-Demonstration prototype

The production procedure of the FD prototypes is described below.

- A carbon foam is machined according to the shape shown in Figure 5.3. Two longitudinal cavities are grooved on the bottom of the carbon foam in order to embed the cooling pipes.
- A layer of Stycast glue with a thickness of 0.1 mm is applied on the carbon foam and the face-plate is glued to it. The thickness of the glue is controlled by a mask frame and has an estimated uncertainty of 0.05 mm.
- Stycast glue is applied to the surface of the cooling pipe by rotating the pipes inside a cavity filled with glue. The pipes are then inserted in the cavity of FD prototypes and pressed in manually. Since during these processes the thickness of Stycast glue is not

precisely controlled, there may be a non-uniform distribution of glue around and along the tube surface. The thickness of the glue is estimated to be on average of 0.20 mm with an uncertainty of 0.05 mm.

- The cavity is sealed with Stycast glue and prototypes are reinforced with a carbon fiber composite.

Table 5.1 presents a list of the main materials of the FD prototypes with their thickness. The thermal conductivity shown in this Table are based on the manufacture specifications. It is worth to notice that the thermal conductivity of the carbon foam in the Table is different from the value found in the data sheet of the material (40 W/m·K). The impact of this difference will be treated as systematic uncertainty on the result ($\Delta T_{Support}$).

Table 5.1: Thermal conductivity of the materials and thickness of the layers used in the FD prototype

Materials	Thermal conductivity [W/m·K]	Thickness [mm]
Kfoam(K9)	28	
Face-plate (ThermalGraph)	1500(Kx)/1500(Ky)/10(Kz)	0.03
Face-plate (TPG)	1500(Kx)/1500(Ky)/10(Kz)	0.3

5.2 Thermal performance evaluation procedure

The thermal performance of the support structure together with the temperature provided by the cooling system determines the sensor temperature (T_{Sensor}) which influence the performance of the physics measurements and the detector life time. Therefore, in this Chapter, T_{Sensor} is used as one of the measurement variables for evaluating the thermal performance of the prototypes.

For a given type of pixel sensor with specific power consumption, the sensor temperature is determined mainly by two factors: the thermal conductance of the local support structure and the thermal convective properties of the evaporated CO_2 . These two factors can be quantified by two temperature differences: $\Delta T_{Support}$ indicating the temperature difference between the sensors (T_{Sensor}) and the inner wall of the cooling pipe (T_{wall}), and ΔT_{CO2} indicating the temperature difference between T_{wall} and the CO_2 fluid (T_{CO2}). Figure 5.4 illustrates these two components, $\Delta T_{Support}$ and ΔT_{CO2}.

The thermal response is further characterized by the total thermal figure of merit, $TFoM_{total}$. This quantifies the thermal performance of the entire system which includes the mechanical support structure and the cooling system. It is defined as (see also equation 1.3):

$$TFoM_{total} = \frac{\Delta T}{\dot{Q}/A_{Sensor}} = \frac{T_{Sensor} - T_{CO2}}{\dot{Q}/A_{Sensor}} \tag{5.1}$$

where A_{Sensor} is the area of the sensor, $\dot{Q}$ is the power dissipated by the module and $\dot{Q}/A_{Sensor}$ is the module's power density. The total $TFoM_{total}$ can be also written (see Figure 5.4) as the sum of two terms :

$$TFoM_{total} = TFoM_{CO2} + TFoM_{Support} = \frac{\Delta T_{CO_2}}{\dot{Q}/A_{Sensor}} + \frac{\Delta T_{Support}}{\dot{Q}/A_{Sensor}} \tag{5.2}$$

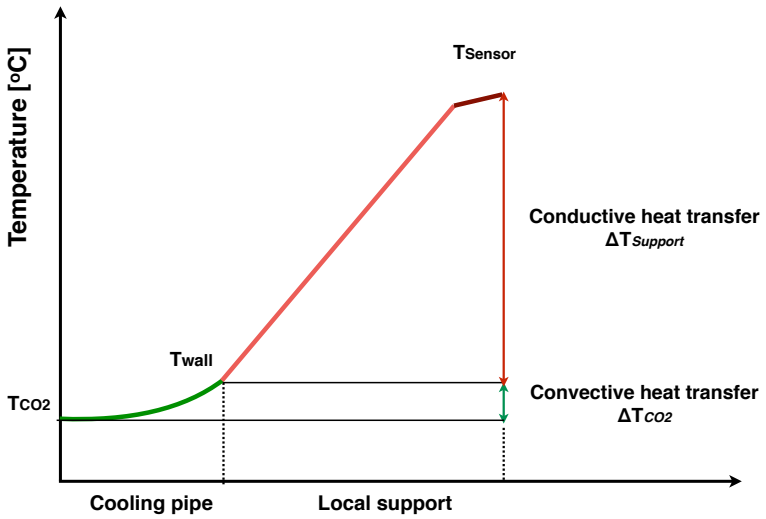

Figure 5.4: Illustration of measurement method.

The first term $TFoM_{CO2}$ depends on the CO_2 evaporation temperature, the tube diameter, the length of the cooling pipe and the mass flow rate. The final $TFoM_{CO2}$ can only be accessed with a full length prototype foreseen to be built in the near future. For this reason, the main focus of the measurement presented in this thesis is on the measurement of the second contribution, $TFoM_{Support}$. The measurement will be compared with the results from the FEA simulation to identify potential design aspects which need further improvements. In the following, the modeling of the Alpine prototype leading to the predictions of the thermal response and the measurements will be described.

5.3 Modeling the Alpine prototype thermal performance

The CoBra program developed in Chapter 3 and the modeling with FEA in Chapter 4 are combined to provide a description of the thermal performance of the Alpine prototypes. FEA is used to predict the temperature difference due to the thermal conduction in the local support structure, $\Delta T_{Support}$; the CoBra program is used to predict the ΔT_{CO_2} related to heat transfer of the fluid CO_2 . The combination of the information from the two program are realized following an iterative process, as described below.

- Step 0: Input to the FEA the geometry description, the thermal conductivity of the material and the heat load.
- Step 1: Calculate the temperature at given locations of the sensors assuming a constant temperature on the inner tube wall (T_{wall}=0); calculate the heat flux through the wall of the cooling pipe ($HFLX_{wall}$) from FEA.
- Step 2: Use the $HFLX_{wall}$ from Step 1 and the CoBra program to calculate the temperature along the tube wall (T_{wall}) according to the input parameters: the CO_2 saturation temperature (T_{CO2}), mass flow rate (Fr) and the vapor quality at the inlet of the cooling pipe (x_{inlet});
- Step 3: Use the T_{wall} from Step 2 as the new temperature of the tube wall for the FEA calculation and get the temperature at given locations on the sensors and update

HFLX$_{wall}$.

- Repeat Step 2 and Step 3 until the process converges, i.e. the results of T_{wall} from two consecutive iterations differs by less than 0.1 °C.
- Get the temperature difference of $\Delta T_{TopCO2} = T_{Sensor} - T_{CO2}$.

In the following the $\Delta T_{Support}$ and ΔT_{CO2} are discussed individually in order to understand their effects separately.

5.3.1 Prediction of $\Delta T_{Support}$

The prediction of $\Delta T_{Support}$ requires the knowledge of the heat load applied on the prototype and the thermal conductivity of the materials. A power density of 0.7 W/cm^2 (as for Layer 0 and Layer 1) is used in the simulation. The material properties and dimensions are set to be the same as the manufacture specifications. Uncertainties on the material properties are treated as systematic errors. The imperfect knowledge of the thermal resistance at the interfaces between different materials related to the manufacture procedure will be discussed at the end of the Chapter. In the following, the predictions of $\Delta T_{Support}$ for the PoC and FD prototypes are presented.

Proof-of-Concept prototype

Figure 5.5 (left) presents the predicted results of $\Delta T_{Support}$ (blue labels) [1] for the PoC prototype in three locations: on top of the two mountains and in the barrel region. The assumed power density corresponds to a heat load of 2.8 W on the mountains and 5.6 W in the barrel region. At the same power density, the temperatures on M1 and M2 are 2°C and 4 °C higher than in the barrel region, respectively. The highest temperature is reached on the M2 which is adjacent to the barrel region.

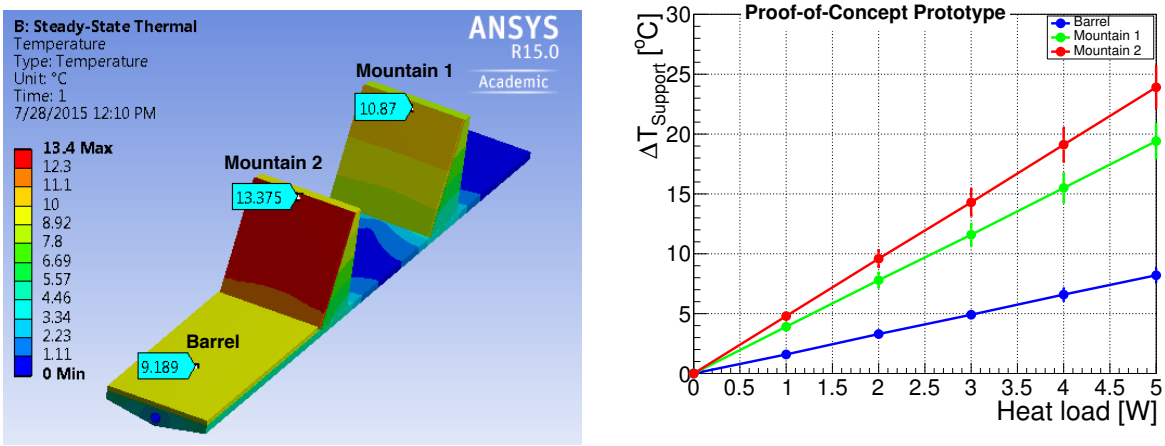

Figure 5.5: Simulated temperatures in the barrel region and on the top of the mountains of the Proof-of-Concept prototype with a power density 0.7 W/m^2(left). Simulated $\Delta T_{Support}$ on top of the mountains and barrel region as a function of heat load (right).

The predictions of $\Delta T_{Support}$ at the three locations as a function of heat load are shown in Figure 5.5 (right) by red (M2), green (M1) and blue (Barrel) lines. The error bars indicate the

[1] $\Delta T_{Support}$ is the difference between the highest temperature on top of the mountains (or in the barrel region) and the temperature of the inner tube wall, T_{wall}.

uncertainty deriving from the imperfect knowledge of the geometry and the thermal properties of the material of the prototype, among which the thickness of the glue and the thermal conductivity of the carbon foam give major contributions. As this prototype is manufactured by the company IVW which has gained expertise from building the IBL detector staves, the uncertainties on the thickness of various layers are assumed to be relatively small. Since the thermal conductivity of the carbon foam (K9) being used to produce the PoC prototype is unknown, the value shown in a data-sheet of the carbon foam (K9) of 40 W/m·K is used and an uncertainty of 25% on this parameter is considered. The uncertainties assigned to the various parameters and the effect on $\Delta T_{Support}$ are listed in Table 5.2.

Table 5.2: Uncertainty on the $\Delta T_{Support}$ calculation for mountain 1 of PoC prototype deriving from the imperfect knowledge of the geometrical and thermal parameters

Parameters	Value		$\Delta(\Delta T_{Support})$ [%]
Kfoam [W/m·K]	40	±10	∓6%
Thickness of glue around pipe [mm]	0.10	±0.02	±4%
Thickness of glue behind face-plate [mm]	0.10	±0.02	±2%
Thickness of face-plate [mm]	0.15	±0.02	±0.1%
Thickness of grease [mm]	0.10	±0.05	±0.1%
Total uncertainties			±7.5%

Functional-Demonstration prototype

The model of the stave is modified to describe the FD prototype. The thickness and the thermal conductivity are set to the values shown in Table 5.1. The top plots in Figure 5.6 present the predicted $\Delta T_{Support}$[2] for the ThermalGraph and TPG prototypes with a heat load of 5.3 W based on the assumed power density. The two FD prototypes show very similar results, in particular that $\Delta T_{Support}$ of the ThermalGraph and TPG prototypes are 13.5 °C and 13.8 °C, respectively.

The prediction of $\Delta T_{Support}$ as a function of heat load for the two FD prototypes are presented in the bottom plots. The uncertainties on these results are evaluated. Table 5.3 lists each contribution to the uncertainty on $\Delta T_{Support}$. The carbon foam has an average thermal conductivity of 28 W/m·K. A variation of ±4 W/m·K is considered. According to the FD prototype manufacture technology described in Section 5.1.2, an uncertainty of the thickness of the glue layer around the cooling pipe and behind the face-plate is taken into account.

5.3.2 Prediction of ΔT_{CO2}

The prediction of ΔT_{CO2} requires to know the heat flux through the wall of the cooling pipe (HFLX_{wall}), the evaporation temperature of CO_2 (T_{CO2}), the vapor quality at the inlet of the cooling pipe (x_{inlet}) and the mass flow rate (Fr). As mentioned, HFLX_{wall} is obtained from the FEA result.

As an example, a prediction of ΔT_{CO2} is presented here. In Figure 5.7 (left), the heat fluxes from the FEA of the ThermalGraph and TPG prototypes with 5.3 W applied on the mountain

[2] $\Delta T_{Support}$ is the difference between temperature on top of the mountain (where the temperature is the highest) and the temperature of the inner tube wall.

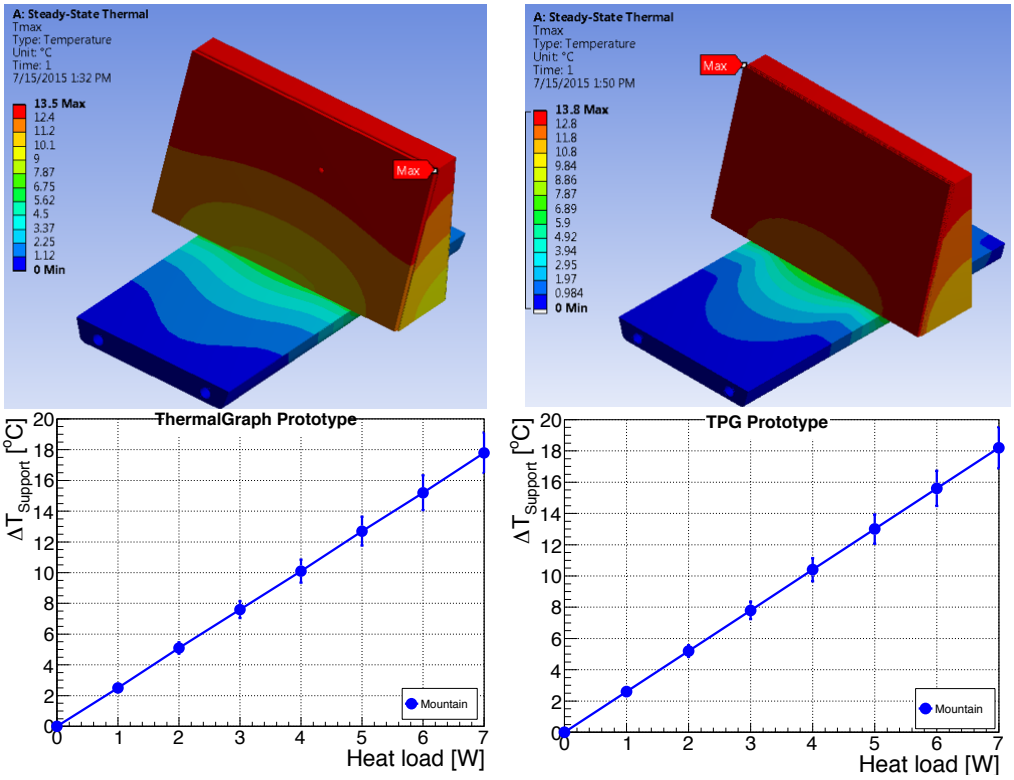

Figure 5.6: Simulated $\Delta T_{Support}$ of the ThermalGraph and TPG prototypes with power density 0.7 W/m^2 (5.3 W on the mountain) (top plots). Simulated $\Delta T_{Support}$ for the ThermalGraph and TPG prototypes as a function of heat load (bottom plots).

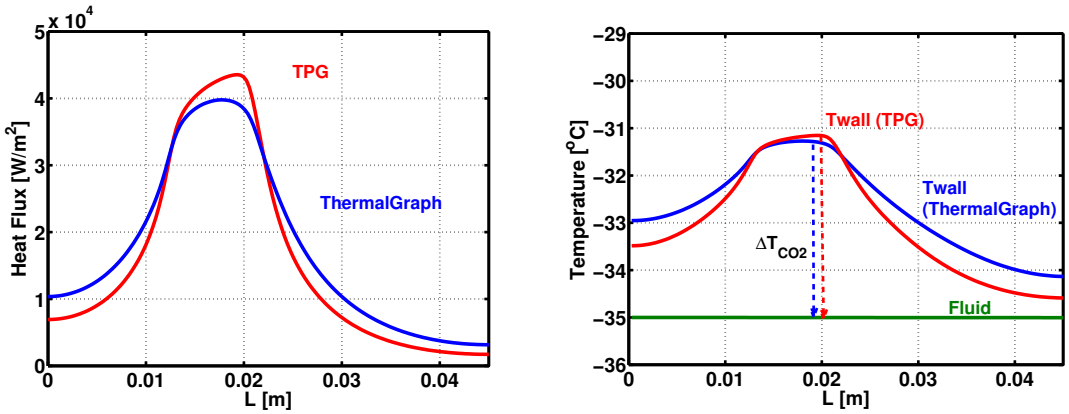

Figure 5.7: Heat fluxes through the wall of the cooling pipe of the FD prototypes along the flow direction (left). Temperature distributions of the CO_2 fluid and tube wall along the flow direction of the prototypes (right).

are shown. The CO_2 flows from the rear of the mountain to the front of the mountain. Based on these heat fluxes distributions, the temperature distributions of the inner tube wall along the flow direction are calculated and shown in the right plot of Figure 5.7 assuming that T_{CO2}=-35.0 °C, Fr=1.0 g/s and x_{inlet}=0.01. The maximum temperature of the tube wall is reached when the CO_2 flows underneath the mountain where the maximum heat flux occurs. The temperature difference between the maximum temperature on the tube wall and the evaporation temperature illustrating by the blue and red dashed line are defined as ΔT_{CO2}. Different conditions of the CO_2 fluid leads to different ΔT_{CO2}. In order to understand the predicted results, the variation

Table 5.3: Uncertainty on the $\Delta T_{Support}$ calculation for the ThermalGraph prototype deriving from the imperfect knowledge of the geometrical and thermal parameters

Parameters	Value		$\Delta(\Delta T_{Support})$ [%]
Kfoam [W/m·K]	28	±4	∓5%
Thickness of glue around pipe [mm]	0.20	±0.05	±5%
Thickness of glue behind face-plate [mm]	0.10	±0.05	±2%
Thickness of face-plate (ThermalGraph) [mm]	0.03	±0.01	±0.1%
Thickness of grease [mm]	0.10	±0.05	±0.1%
Total uncertainties			±7.3%

of ΔT_{CO2} for ThermalGraph prototype under different conditions are evaluated.

Evaporation temperature. The evaporation temperature (T_{CO2}) affects the evaporation heat transfer performance. The ΔT_{CO2} for different T_{CO2} are evaluated as a function of heat load and shown in Figure 5.8, assuming Fr=1.0 g/s and x_{inlet}=0.01. For a given heat load, ΔT_{CO2} decreases when T_{CO2} increases, but this effect is small. This effect is interpreted as due to the fact that at a higher T_{CO2}, the local HTC is higher and therefore ΔT_{CO2} is reduced.

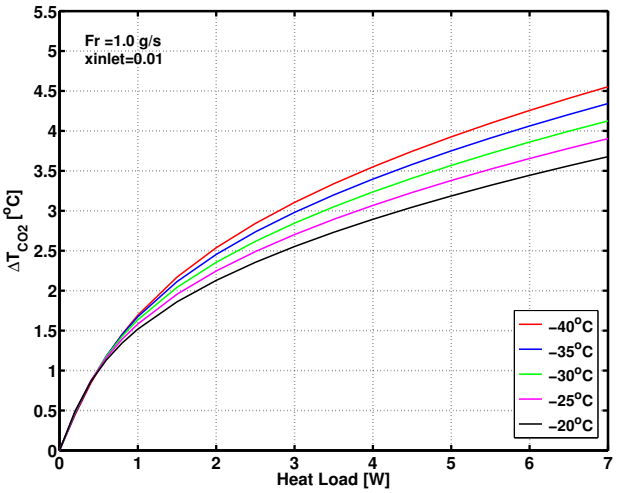

Figure 5.8: ΔT_{CO2} as a function of heat load with different evaporation temperature for Fr=1.0 g/s and x_{inlet}=0.01.

Mass flow rate. The mass flow rate (Fr) impacts mainly the convective evaporating heat transfer coefficient. Figure 5.9 shows ΔT_{CO_2} as a function of heat load for different mass flow rate from 0.5 g/s to 2.5 g/s under the conditions of T_{CO2}=-35.0 °C and x_{inlet}=0.01. When the heat loads are equal to 1 W, the differences of ΔT_{CO_2} between the maximum and minimum Fr considered are of the order of 1 °C. This difference becomes less and less significant when the heat load increases.

Inlet vapor quality. The inlet vapor quality (x_{inlet}) determines the local flow pattern of CO_2 and hence also the local HTC. The prediction of ΔT_{CO_2} as a function of heat load with

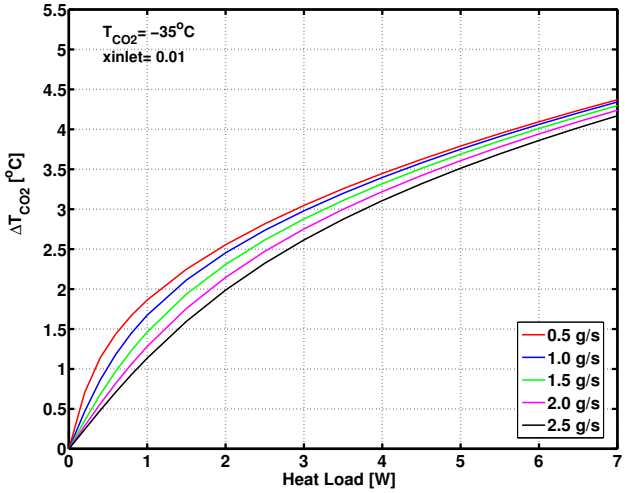

Figure 5.9: ΔT_{CO2} as a function of heat load with different mass flow rate for T_{CO2}= -35.0 °C and x_{inlet}=0.01.

various x_{inlet} is shown in Figure 5.10 assuming T_{CO2} = -35.0 °C and Fr = 1.0 g/s. At a given heat load, a lower inlet vapor quality induces a higher ΔT_{CO_2} due to a lower local HTC. For a wide range of variation of x_{inlet} from 0.01 to 0.4, the variation of ΔT_{CO2} is about 1.5 °C when the heat load is 5 W.

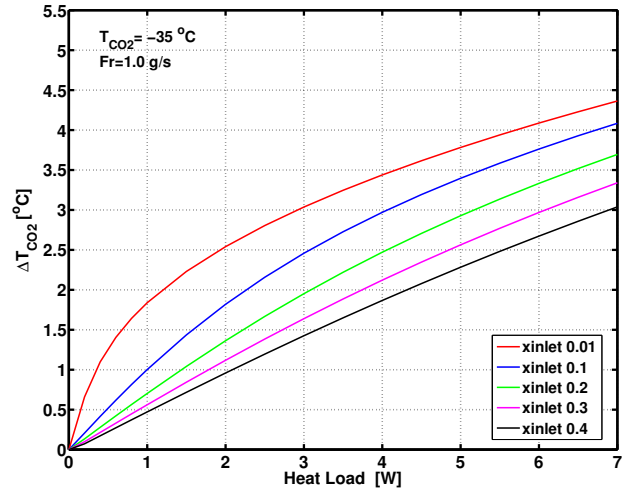

Figure 5.10: ΔT_{CO2} as a function of heat load with different inlet vapor quality for T_{CO2}= -35.0 °C and Fr=1 g/s.

Uncertainties on the predictions of ΔT_{CO2} for the PoC prototype

The PoC prototype was tested using the original CO_2 cooling system which will be described later in the Section 5.4.1. The variables which influence the prediction of ΔT_{CO2} are T_{CO2}, Fr, $\dot{Q}$ and x_{inlet}.

- The uncertainty on T_{CO2} is 0.3 °C. The value of T_{CO2} and its uncertainty are discussed in Section 5.5.1 based on the measurements of PoC prototype.

- In the original CO_2 cooling system, the mass flow rate is not measured directly but is estimated from the adjustment level of the needle valve. This quantity is estimated to be 1.0 ± 0.5 g/s.

- $\dot{Q}$ is read out directly from the voltage and current display on the power supply, which has a 0.1% relative uncertainty.

- x_{inlet} is obtained from the pressure-enthalpy diagram. The determination of the exact isothermal line depends on the environment temperature which is at 21 °C ± 1°C. This leads to an estimated uncertainty on x_{inlet} of ±0.03.

The effect of the discussed uncertainty on ΔT_{CO2} is shown in Table 5.4. The total uncertainty estimated as the sum in quadratic is 1.0 °C.

Table 5.4: Uncertainty on ΔT_{CO2} for the M1 of the PoC prototype

Parameters	Value		$\Delta(\Delta T_{CO2})$ [°C]
CO_2 temperature [°C]	-40.5	±0.3	±0.05
Flow rate [g/s]	1.0	±0.5	±1.0
Inlet vapor quality	0.43	±0.03	∓0.1
Total uncertainties[°C]			±1.0

Uncertainties on the predictions of ΔT_{CO2} for the ThermalGraph

The ThermalGraph prototype is tested using the upgraded CO_2 cooling system. Like the analysis done for the PoC prototype, the variables related to the prediction of ΔT_{CO2} are still T_{CO2}, Fr, $\dot{Q}$ and x_{inlet}.

- The uncertainty of T_{CO2} is evaluated as 1.3 °C as discussed in the measurement uncertainty of the ThermalGraph prototype in Section 5.5.2.

- In the upgraded CO_2 cooling system, the mass flow rate is measured directly by the flow meter. The systematic error from the measurement is ±0.01 g/s.

- $\dot{Q}$ is read out directly from the voltage and current reading from the power supply, which amount to a 0.1% relative uncertainty.

- In the upgraded system with the pre-cooler installed, the inlet vapor quality is determined by the effect of heat exchange inside the pre-cooler. There is no direct measurement on x_{inlet}, therefore it is again obtained from the pressure-enthalpy diagram and is estimated to be 0.10 ± 0.05. This uncertainty of 50% derives from the fact that the temperature of the hot fluid after entering the pre-cooler is not measured.

Table 5.5 lists each systematic uncertainty contribution to the ΔT_{CO_2} of the ThermalGraph prototype.

Table 5.5: Uncertainties on ΔT_{CO2} for the ThermalGraph prototype

Parameters	Value		$\Delta(\Delta T_{CO2})$ [°C]
CO_2 temperature [°C]	-35.0	±1.3	±0.2
Flow rate [g/s]	0.66	±0.01	±0.008
Inlet vapor quality	0.1	±0.05	∓0.3
Total uncertainties [°C]			±0.4

5.4 Measurement setup

5.4.1 CO_2 cooling system

A CO_2 cooling system is available in the laboratory to test the Alpine prototypes. This cooling system is an open loop system, where the cooling media is released into the atmosphere after flowing through the test sample. A schema and a picture of the system are presented in Figure 5.11. It consists mainly of a liquid CO_2 bottle, a filter, a needle valve as mass flow rate regulator, a test section for connecting the detector unit, a post-heat exchanger embedded in a thermal bath, a relief valve as pressure regulator and two absolute pressure transducers. The Figure also shows the measurement (red), the command (blue) and the electric power (green) lines. The CO_2 flows according to the following sequence:

- The CO_2 in the saturated liquid phase is released from bottle and flows through a filter which is necessary to remove dust particles,
- The saturated liquid CO_2 flows through a needle valve which regulates the mass flow rate. The fluid undergoes a pressure drop and the CO_2 starts to evaporate immediately,
- The CO_2 enters into the test sample,
- After that the CO_2 has passed through the test sample, it enters into a post-heat exchanger immersed in a water thermal bath at a temperature of 40 °C, the CO_2 is warmed up and evaporates completely.
- The CO_2 in a vapor state flows through the relief valve (pressure regulator) and is released safely into the atmosphere. The adjustment level of the pressure regulation valve determines the pressure in the test unit section and therefore the CO_2 evaporation temperature.

Figure 5.12 presents a diagram of the pressure versus the specific enthalpy of the CO_2 fluid, which is used to describe the behavior of the CO_2 in the cooling system. In this diagram, the iso-thermal lines (T), the vapor quality lines (x) and the density lines (r) of the CO_2 are represented. In the following the relevant thermodynamic processes taking place in the cooling system are explained assuming that the CO_2 evaporation temperature is set to -40 °C. These processes are represented in Figure 5.12 by the red and green lines.

- Process 1-2. The CO_2 initially in the state of saturated liquid at a temperature of 20 °C gets into a liquid-gas two-phase state after a pressure drop induced by the flow and pressure regulators. When the CO_2 temperature reaches -40°C, its vapor quality is ≈ 0.45.

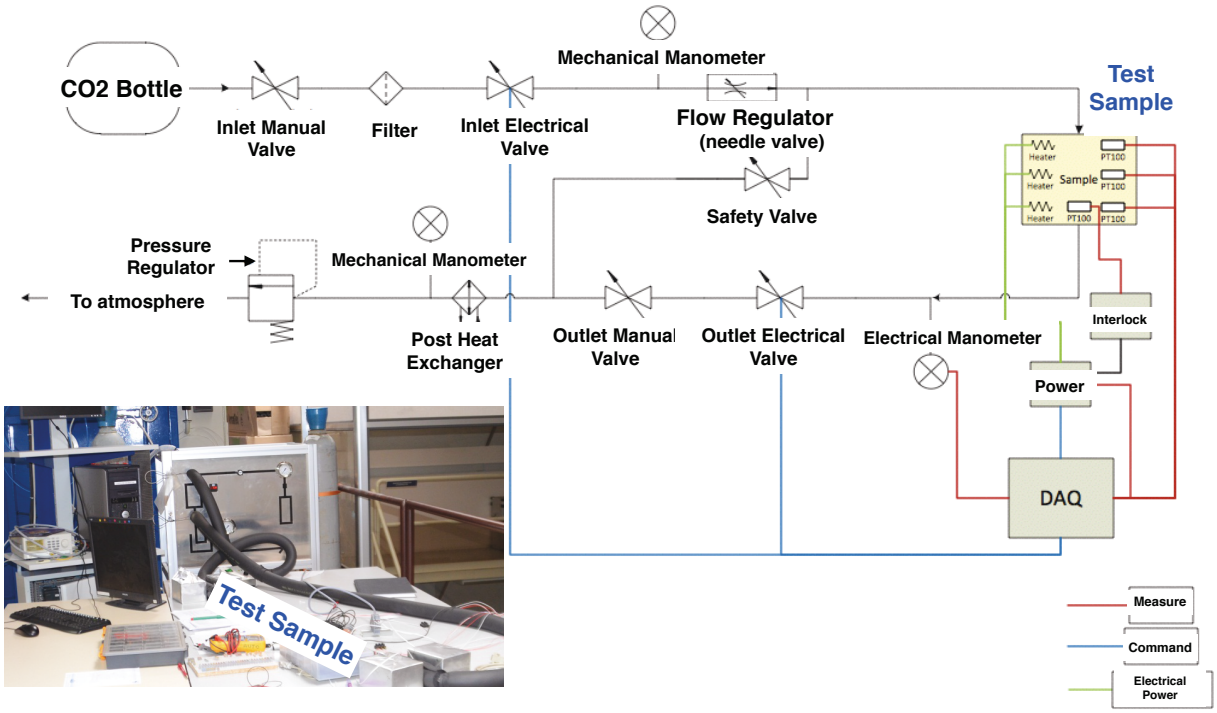

Figure 5.11: Schematic view and photo of the CO_2 cooling system used for the tests of the Alpine prototypes.

- Process 2-3. The two-phase CO_2 flows through the test sample where the heat load is applied. As a result, the specific enthalpy of the CO_2 increases.

- Process 3-4. After the test unit, the CO_2 is heated up at constant pressure and evaporates completely and is released into the atmosphere.

The work performed in the context of this thesis showed that it is necessary to upgrade the existing cooling system so that it can be used to test the full stave prototype in the future. The improvement concerned the increase of the cooling capacity with an installation of a pre-cooler and of a mass flow meter to perform measurements of the flow rate, as it will be explained in the following. In the original system, as shown in the pressure-enthalpy diagram of Figure 5.12, the CO_2 entering in the test unit is already at a vapor quality of ≈ 0.45. Figure 5.13 shows in the general case of a full stave the temperature of the fluid (green) and of the tube wall (blue) along a 2 m long cooling path for a power input of 110 W which is in the ballpark of the power input per stave according to Table 4.2. With an inlet vapor quality of x_{inlet} $\approx$0.45, the CO_2 reaches the dry-out regime at the outlet of the cooling pipe and the tube wall increases abruptly. This condition is not desirable as discussed in Chapter 4. A way of increasing the cooling capacity of the system is to cool down the CO_2 before entering the test sample. A simple and efficient pre-cooler consists in a concentric heat exchanger [86] is made of two cooling pipes as described in Section 1.7. The CO_2 at the exit of the test unit at -40°C flows through the inner pipe of the concentric exchanger to pre-cool the fluid from the bottle, which circulates in the external pipe of the heat exchanger. The thermodynamic processes of the upgraded cooling system proceed in a slightly different way than before. The new thermodynamic process are illustrated by the lines on a pressure-enthalpy diagram in Figure 5.14.

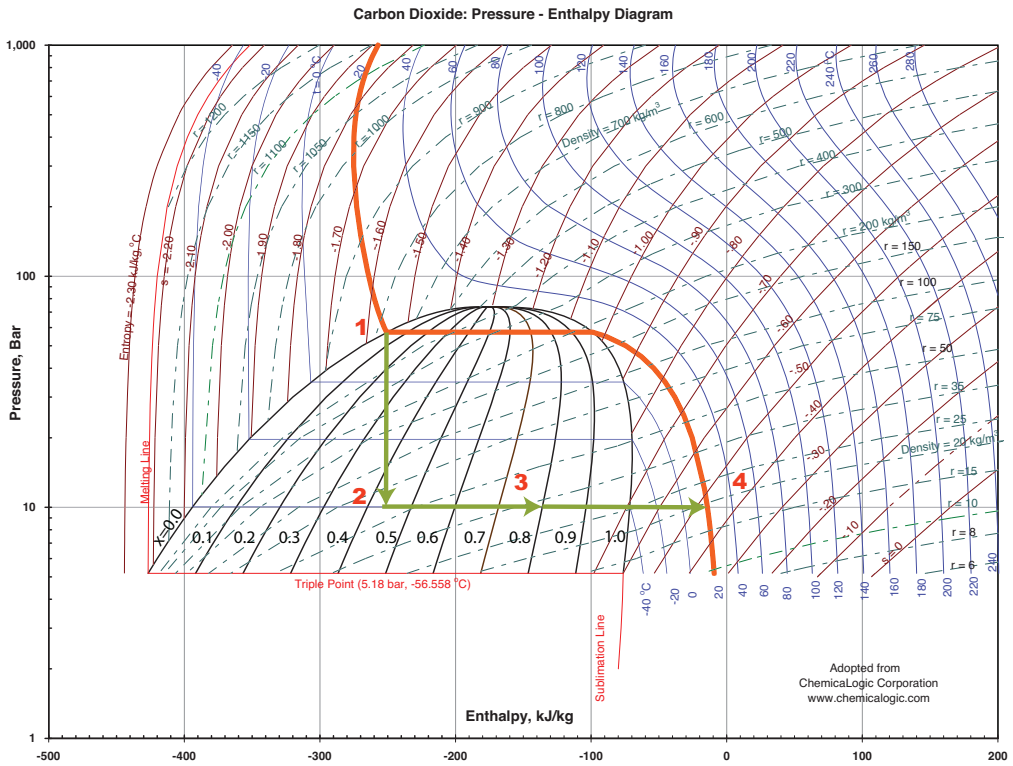

Figure 5.12: An illustration of the thermodynamic process occuring in the CO_2 cooling system at an evaporation temperature of -40 °C. The isothermal line T_{CO2}=20°C is shown in red.

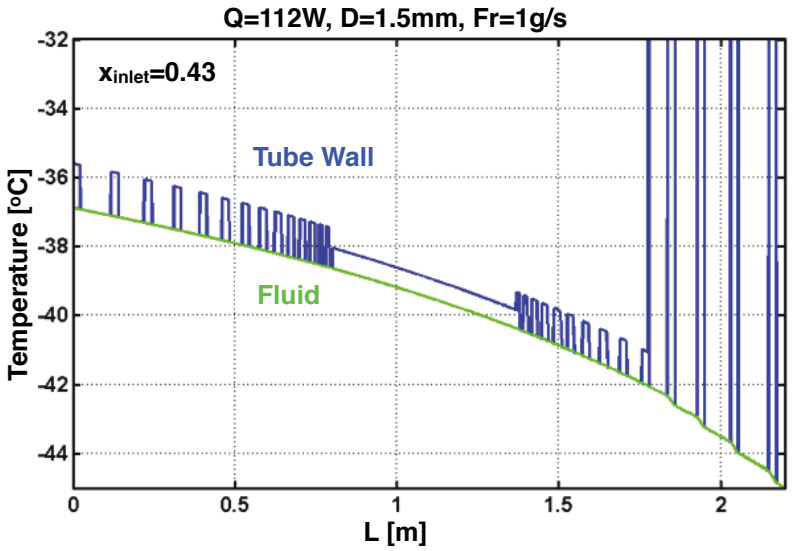

Figure 5.13: Temperature of the cooliing fluid and of the tube wall.

- Process 1-1': The saturated liquid CO_2 at a temperature of 20 °C flows out of the bottle and goes through the external line of the pre-cooler. It exchanges an amount of heat at constant pressure, equal to the variation of the specific enthalpy of the fluid ($Q = \Delta h$") and is cooled down to -40 °C. The exact value of "Δh" depends on the configuration of the heat exchange and the mass flow rate.

- Process 1' - 2: The liquid CO_2 at a temperature of -40 °C gets into a saturation state after flowing through the flow and pressure regulators given that its pressure is mainly

adjusted by the pressure regulator. The exact vapor quality at the end of this process depends on Δh and hence on the configuration of the heat exchanger and the mass flow rate.

- Process 2 - 3: The two-phase CO_2 flows through the test sample at constant pressure to absorb the heat.
- Process 3 - 3': The CO_2 in a two-phase state flows through the internal line of the pre-cooler to cool down the CO_2 which comes out of the bottle. (This is the reversal of the process of 1-1').
- Process 3' - 4: The CO_2 is heated up by a water bath and vented into the atmosphere.

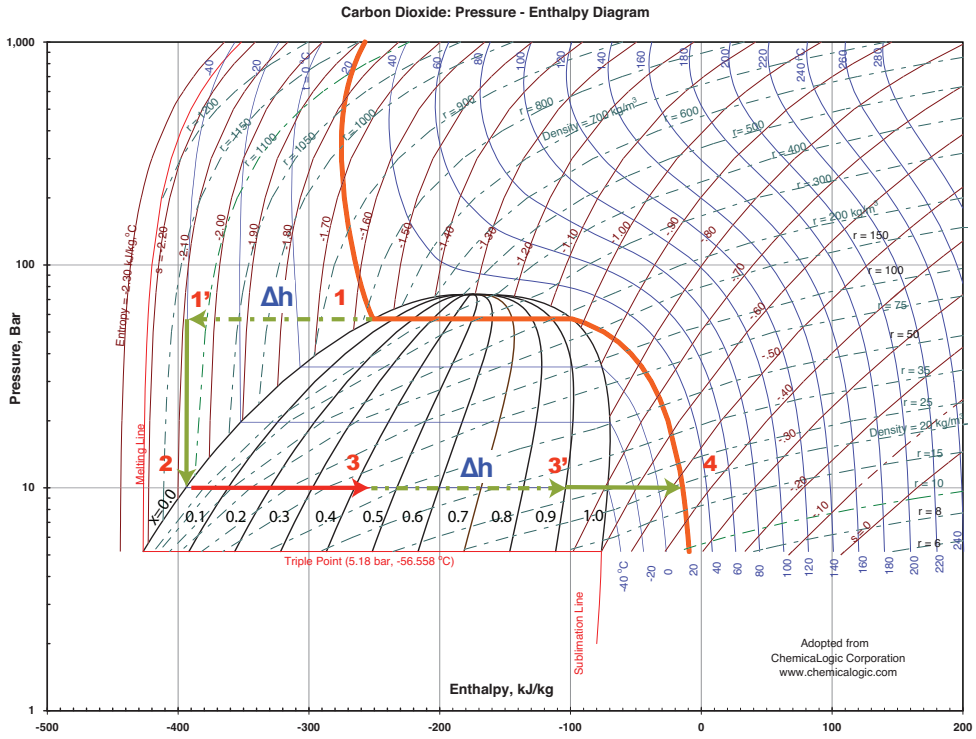

Figure 5.14: The flow process of the upgraded CO_2 cooling system indicating the process when fluid flows through a pre-cooler.

Together with the pre-cooler, a Corioli (RHE 15 and RHE07) flow meter was installed to measure the mass flow rate on the cooling line between the inlet manual valve and the filter.

5.4.2 Measurement preparation

The prototypes are connected to the CO_2 cooling system via stainless steel and flexible transportation lines. Heaters are mounted on each prototype to simulate the power generated by the modules. Thermal grease is applied, following a delicate procedure based on the experience of IBL modules [26] between the surface of the prototype and the heater to reduce the contact resistance. Temperature sensors are then mounted at various locations.

The detailed procedure of mounting the heaters on the PoC prototype is described in the following and shown in Figure 5.15:

Figure 5.15: Illustration of implementing the heaters and the temperature probes for the PoC prototype. a) shows the procedure at the mountain region and b) shows the procedure at the barrel region

- Spray a fine layer of glue (UHU) with a thickness of 0.1 mm on a metal frame mask, and then wait for about 20 minutes. The purpose of the procedure is to glue the frame mask temporarily on the face-plate to deliminate the area of the thermal grease. Its role is to assure a good thermal contact between the support structure and the heater.
- Put the side of the mask with the UHU glue on the prototype. (mountains or the barrel region).
- Put the thermal grease on the edge of the mask and smear it along the face-plate of the prototype; Once the thermal grease is in place, the mask is removed and cleaned for re-utilization;
- Apply the glue (Araldite) on the remaining surface area of the face-plate to glue the heater on it.

A power supply with an accuracy of 0.1% is used to provide power to the heaters. The temperature sensors PT100 are placed on the prototype. They are calibrated before each measurement and have an accuracy of 0.3 °C. Figure 5.16 illustrates the locations of the temperature sensors on the prototypes. For the PoC prototype (left), three sensors are located on the top of the two heaters and in the barrel region. FD prototypes have five temperature sensors on the top, the bottom of the heater, as well as on the cooling pipe, at the locations of the inlet, the outlet and the middle of the length of the pipe. Since the thermal measurements are at low temperatures between -20 °C and -40 °C, in order to reduce the heat exchange between the prototype and the environment, the prototypes are thermally insulated inside a box made of insulation material (Kaiflex, thermal conductivity 0.0031 W/m·K at -30 °C).

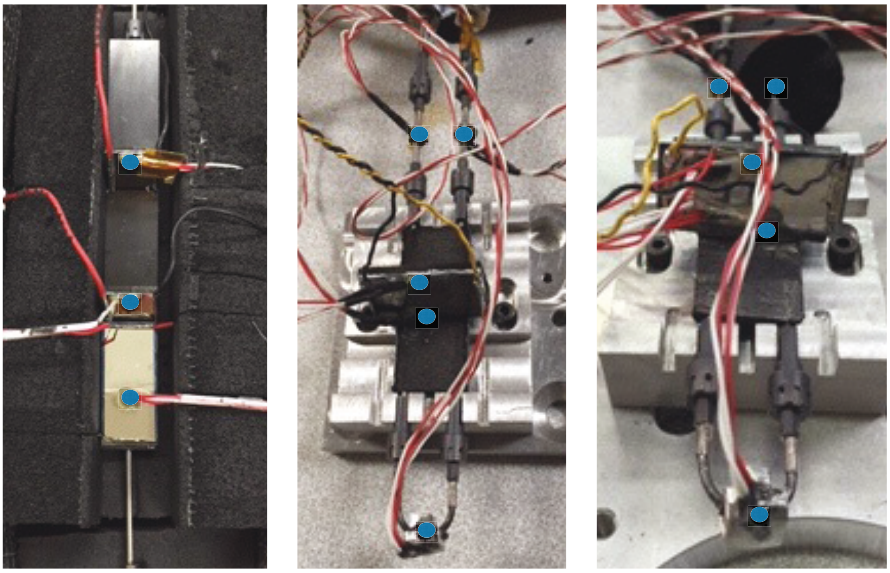

Figure 5.16: Illustration of the locations of the temperature probes on the PoC (left) ThermalGraph (middle) and TPG (right) prototypes.

5.4.3 Measurement condition

The thermal response of the prototypes are measured under a wide range of conditions simulating different operation scenarios. Measurements are performed using several heat loads according to the power density requirements listed in Chapter 4 and the surface area where the heater is located. Table 5.6 lists the values of the heat load considered to be applied on the mountain area of the prototype. The thermal response is also measured with different mass flow rate at a constant $\dot{Q}$ applied and at constant T_{CO2}. In addition, the measurement are carried out varying the CO_2 evaporation temperature in the range between -40 °C and -20 °C. As

Table 5.6: Required heat load for the Alpine prototypes thermal measurement

Prototype	Power density [W/cm^2]	Mountain area [cm^2]	Heat load [W]
PoC	0.5/0.7	1.9×2.1	2.0/2.8
FD	0.5/0.7	3.6×2.1	3.8/5.3

the power consumption for the final detector modules are not yet fully established, and varies among different layers, the thermal response of the prototypes under different heat load conditions is the most important measurement and is carried out for every prototype. The effects of the value of the mass flow rate and of the CO_2 evaporation temperature are investigated using only the ThermalGraph prototype and the behavior is assumed to be applicable to the others.

5.5 Measurement results

The measurement results for the PoC prototype and the ThermalGraph prototype are presented in this Section. The TPG prototype measurement result will not be discussed since they are still going on.

5.5.1 Proof-of-Concept prototype

The measurements for PoC prototype was carried out using the original CO_2 cooling system without pre-cooler and mass flow meter. The main purpose of this measurement is to verify the feasibility of the Alpine design.

Different heat loads are applied on barrel and mountain regions in three steps. The measurement results are presented in Figure 5.17 (left). This Figure shows the temperatures response in the barrel region and at the top of mountains (M1 and M2) as function of time when different heat loads are applied. In the time intervals Δt = 400 - 650 s and Δt = 1000 - 1300 s, there is no heat load applied. The dip at about 1350 s corresponds to a heat load adjustment. The temperature during this period was not at equilibrium, thus, the result is discarded.

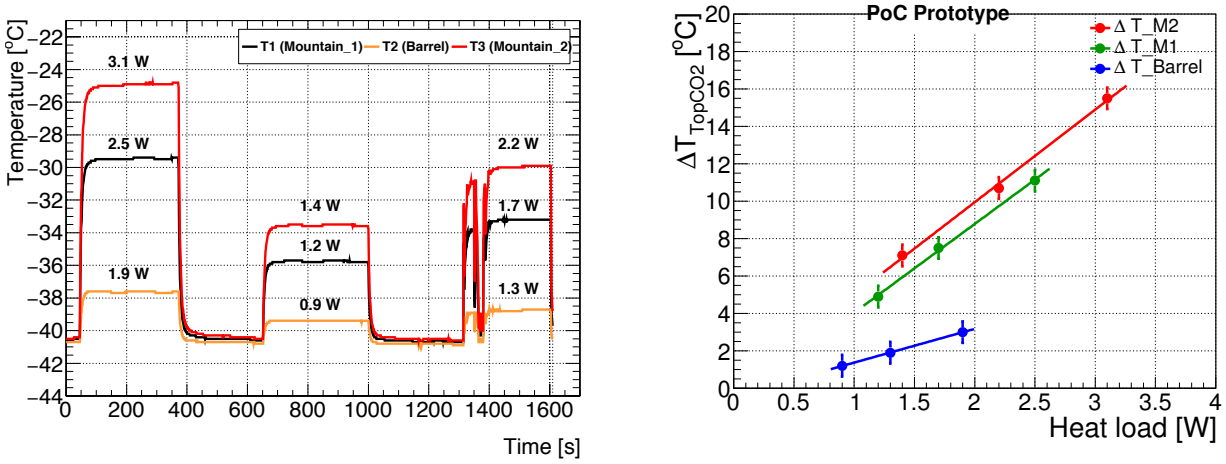

Figure 5.17: Measured temperature of Proof-of-Concept prototype with various heat load as function of time(left). Measured temperature difference ΔT_{TopCO2} of Proof-of Concept prototype with various heat load.

In this setup, there are no temperature sensor on the cooling pipe to measure the temperatures of the external wall of the cooling pipe (related to the CO_2 evaporation temperature). It is assumed that under zero heat load, when the whole structure reaches thermal equilibrium, the three sensors mounted on the structure have the same temperature as the CO_2 inside the cooling pipe. The temperature measurements show that during the time interval when no heat load is applied, the difference between the temperature probes, corresponds to their measurement accuracy (0.3 °C). This result indicates that the whole structure reached the thermal equilibrium. The temperature of the CO_2 is estimated to be -40.5 °C. At this temperature, a vapor quality of $x_{inlet} \approx 0.45$ is estimated from the pressure-enthalpy diagram in Figure 5.12.

Table 5.7 summarizes the temperatures on the top of the mountains and in the barrel region for various heat loads. These results satisfy the requirements since when the highest heat load is applied (3.1 W), the highest temperature (top of M2) is below -20 °C, a value which avoids thermal run-away for the Pixel Detector. The difference between the temperature on top of the heater (T_{Top}) and the temperature of CO_2 (T_{CO2}), ΔT_{TopCO2} for M1, M2 and barrel region are shown in Figure 5.17 (right) as a function of the heat load. This quantity has the same increasing rate as function of the heat load on M1 and M2. In addition, ΔT_{TopCO2} of M2 is higher than that of M1 due to the fact that M2 is closer to the barrel region where a heat load is applied.

Table 5.7: Temperature measurements on top of the mountains and on the barrel of the PoC prototype for various heat loads with a CO_2 evaporation temperature of -40.5 °C. Uncertainties on the temperature measurements is ±0.3 °C. The values of heat loads quoted in the Table are those readings generated on the power generator display. The uncertainty on the power measurement is estimated to be ±0.1 % of the readings.

$\dot{Q}_{M1}$[W]	T[°C]	$\dot{Q}_{M2}$[W]	T[°C]	$\dot{Q}_{Barrel}$[W])	T[°C].
1.2	-35.7	1.4	-33.5	0.9	-39.4
1.7	-33.1	2.2	-29.9	1.3	-38.7
2.5	-29.5	3.1	-25.1	1.9	-37.6

Uncertainty on the ΔT_{TopCO2} measurements

The uncertainty on ΔT_{TopCO2} results from the estimation of the CO_2 temperature (T_{CO2}) and the measurement of the temperature on the heaters (T_{Top}) when the heat load is applied.

In this setup, the T_{CO2} is taken as the average temperature when no heat load is applied, and the corresponding uncertainty is estimated to be 0.3 °C. This is the maximum difference among the probe responses when no heat load is applied. The uncertainty on T_{Top} is estimated to be equal to the accuracy of the temperature probes (0.3°C). The effect of the heat exchange with the environment is not taken into account since the temperature sensors show the same value within its accuracy when no heat load is applied. The total systematic uncertainty on the measurement of ΔT_{TopCO2}, evaluated as the sum of the considered uncertainties, is 0.6 °C.

5.5.2 ThermalGraph prototype

The measurements of the ThermalGraph prototype were carried out using the upgraded CO_2 cooling system with the pre-cooler and the mass flow meter.

Thermal response for different heat load

Similarly to the measurement procedure followed for the PoC prototype, heat loads of 5.2 W, 4.7 W, 3.7 W, 2.1 W are applied in sequence to the prototype. The CO_2 mass flow rate is 0.66 g/s. The results are presented in Figure 5.18 (left). The vertical black dashed line on the Figure indicates the moment when the thermal equilibrium is reached after some experimental adjustments. The temperatures of the pipe wall at the inlet (green), outlet (blue) and at the middle of the flow path (black) as function of the time are shown. The evaporation temperature of CO_2, T_{CO2}, is estimated as the average temperature of these three values after that the thermal equilibrium is reached. It is observed that the maximum difference among these values is 1.3°C and does not vary with the applied heat load. This difference is not fully understood and maybe due to an effect of heat exchange with the environment, as it will be discussed later. In Figure 5.18, the temperatures on top (T_{Top}, dark red) and bottom of the mountain (T_{Bottom}, orange) are also shown. The temperatures difference, ΔT_{TopCO2}, as a function of the heat load are presented in the right panel of Figure 5.18. This result will be compared with the prediction.

Thermal response for different CO_2 saturation temperature

The evaporation temperature T_{CO2} is set to -35.0 °C, -23 °C and -25 °C to evaluate the thermal response of the ThermalGraph prototype, at a mass flow rate of 0.6 g/s and under a heat load

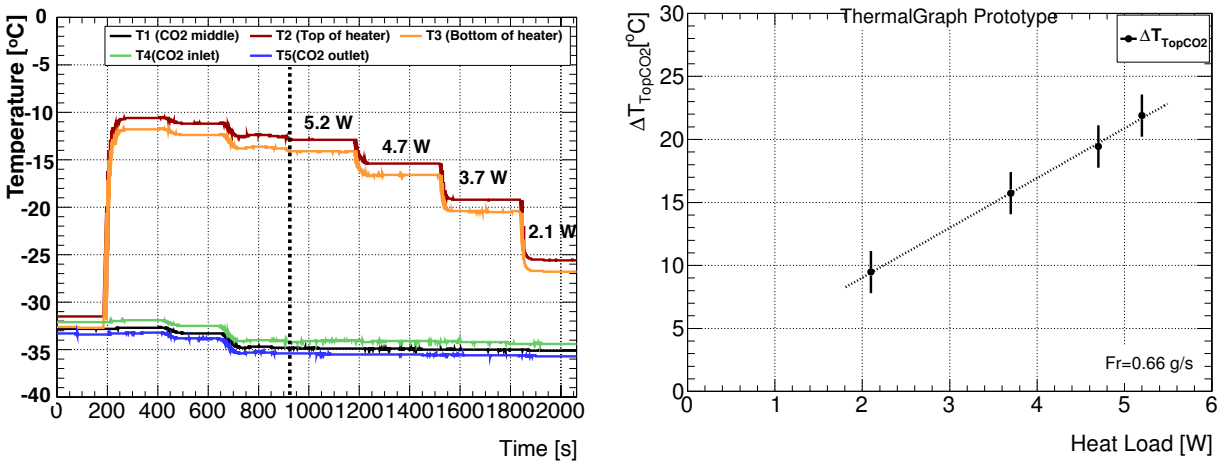

Figure 5.18: Measured temperatures of ThermalGraph prototype with various heat load as function of time (left). Measured temperature difference of ThermalGraph prototype as a function of heat load (right).

of 4.7 W. The left plot in Figure 5.19 shows the temperature response as a function of the time. The right plot shows the temperature on the top of the heater (T_{Top}) as well as ΔT_{TopCO_2} as a function of T_{CO2}. As seen, ΔT_{TopCO_2} changes very little. This result confirms the expectations shown in Figure 5.8 that the temperature difference due to the CO_2 heat transfer does not depend on T_{CO2}. As consequence, ΔT_{TopCO_2} does not strongly depend on T_{CO2}.

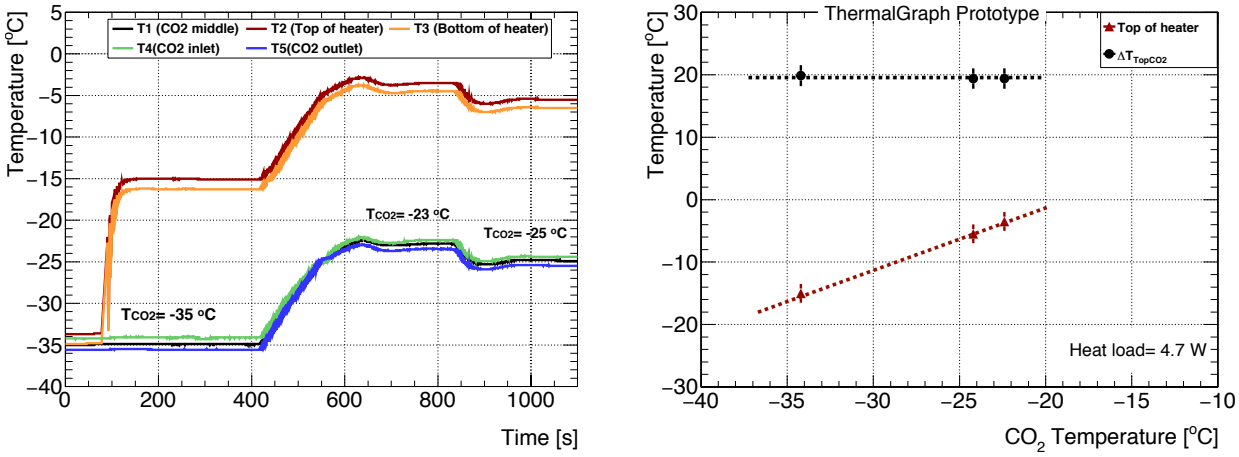

Figure 5.19: Measured temperatures of the ThermalGraph prototype with various evaporation temperature as function of time (left). Measured temperature and temperature differences of ThermalGraph prototype as a function of the evaporation temperature (right).

Thermal response for different CO_2 mass flow rate

The thermal response for different CO_2 mass flow rate (Fr) is measured by changing the Fr from 0.6 g/s to 1.2 g/s at a constant heat load of 3.7 W. The CO_2 saturation temperature increases when the flow rate increases since the temperature of the cooling fluid is controlled by the flow regulator and there is only a small pressure drop across it. As a result, the temperature of the cooling pipe increases, as shown in Figure 5.20 (left). Figure 5.20 (right) shows T_{Top} and T_{CO2}, as well as the temperature difference between the top of heater and the CO_2 fluid

ΔT_{TopCO_2} as a function of the measured flow rate. As shown, although T_{CO2} and T_{Top} slightly increase as the Fr changes, ΔT_{TopCO_2} remains practically constant. This observation confirms the prediction shown in Figure 5.9 that the temperature difference due to the CO_2 heat transfer does not depend on the mass flow rate in the considered range, as a result, ΔT_{TopCO_2} remains stable.

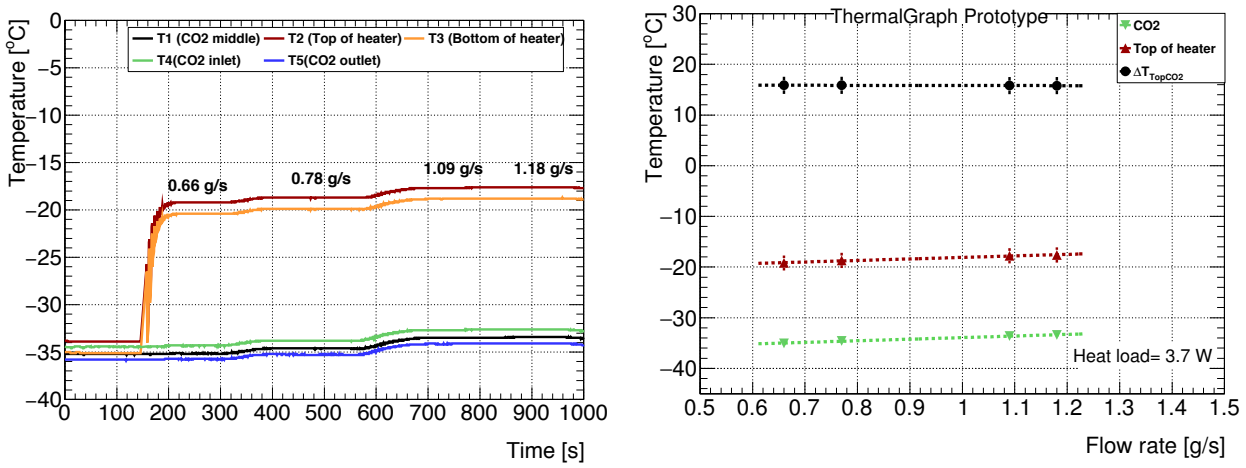

Figure 5.20: Measured temperature of the ThermalGraph prototype with various mass flow rate as function of time (left). Measured temperature and temperature difference of ThermalGraph prototype as function of mass flow rate (right).

Uncertainty on the ΔT_{TopCO2} measurements

The uncertainty on the measurement of ΔT_{TopCO2} derives from the knowledge of the T_{CO2} and of T_{Top} when the heat load is applied. In this setup, T_{CO2} is taken as the average temperature of three measurements on the tube wall (inlet, middle and outlet) where no heat load is applied. The uncertainty on this quantity is estimated to be 1.3 °C, the maximum difference among the three measurements. The uncertainty on T_{Top} is estimated to be equal to the accuracy of the temperature probes (0.3 °C).

When no heat load is applied the temperature on top of the heater is 1.2 °C higher than the temperature at the bottom. This difference is interpreted as due to a heat leak effect inside the insulation box and confirms the tentative explanation.

The total uncertainty on the measurement of ΔT_{TopCO2} is evaluated to be 1.6 °C, which is the sum of the uncertainty on T_{CO2} and T_{Top}.

5.6 Comparisons and thermal performance of prototypes

In this section, the prediction of the temperature difference ΔT_{TopCO2} are compared with measurements. The uncertainty on the measurements as well as on the predictions are accounted in the comparison. Finally, the thermal performance of the support structure of the two prototypes is assessed in terms of the figure of merit $TFoM_{Support}$.

5.6.1 PoC prototype

The predicted ΔT_{TopCO2} is calculated according to the procedure described in Section 5.3. Figure 5.21 shows for the PoC prototype the predicted heat fluxes through the cooling pipe wall

as a function of the flow direction for the several heat loads which are used in the measurements. The temperatures of the fluid and of the inner tube wall as a function of the flow direction are

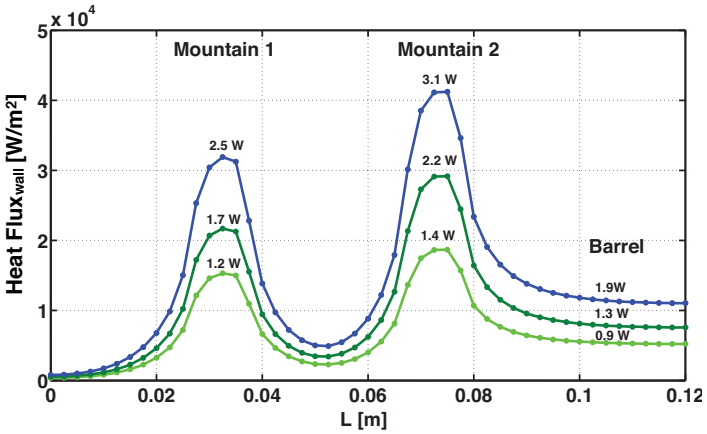

Figure 5.21: Simulated heat flux through pipe with FEA under various heat load versus the length of the PoC prototype

calculated and shown in Figure 5.22. The predicted temperatures on top of the mountains and

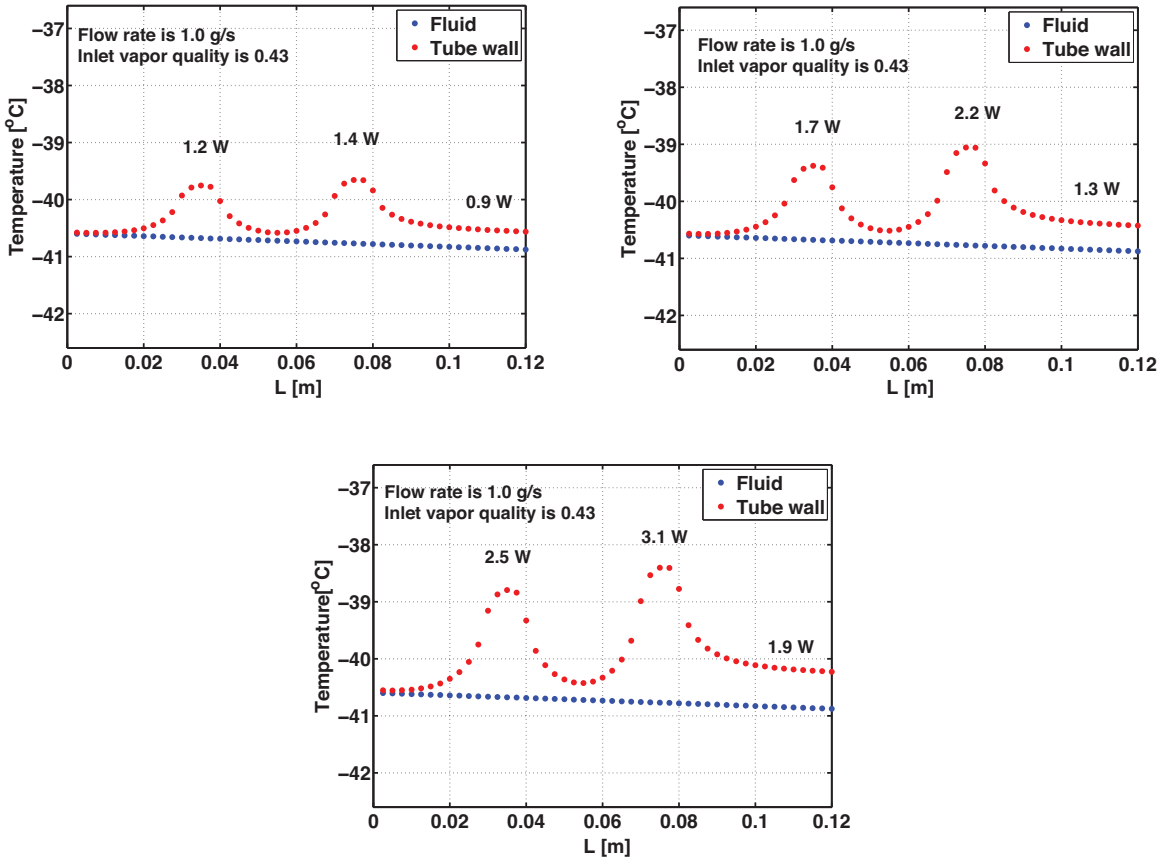

Figure 5.22: ΔT_{CO2} Simulation results for the PoC prototype.

in the barrel are summarized in Table 5.8. The results of the measurements (Table 5.7) and

Table 5.8: Results of the temperature predictions on top of the mountains and in the barrel of the PoC prototype for various heat load with the evaporation temperature of -40.5°C.

$\dot{Q}_{Mountain1}$[W]	T[°C]	$\dot{Q}_{Mountain2}$[W]	T[°C]	$\dot{Q}_{Barrel}$[W])	T[°C]
1.2	-35.5	1.4	-33.7	0.9	-39.0
1.7	-33.2	2.2	-29.6	1.3	-38.1
2.5	-29.7	3.1	-25.1	1.9	-36.8

the predictions presented (Table 5.8) are used to get the measured and predicted temperature difference ΔT_{TopCO2}. The comparison between measurements and predictions is shown in Figure 5.23 as a function of heat load. As seen, the predictions agree with measurements within uncertainties, which indicates that the model employed is able to describe the measurements.

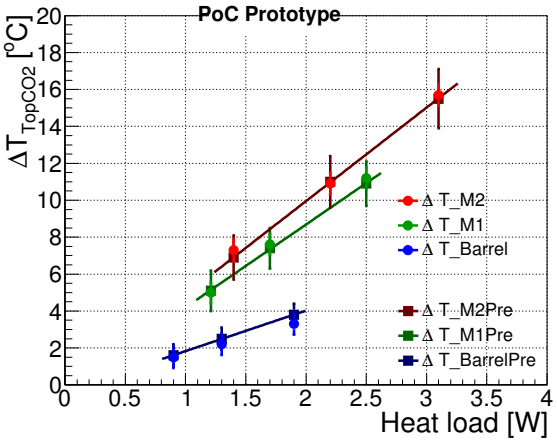

Figure 5.23: Comparison of predictions and measurements of PoC prototype as a function of heat load. The dark red, green and blue lines represent the prediction results of M2, M1 and barrel respectively. The light red, dark green and dark blue dots represent the measurement results of M2, M1 and barrel region respectively.

The maximum value of ΔT_{TopCO2} are located on top of the mountains. There is at most about 15°C temperature difference between the heater and the CO_2 fluid when the CO_2 fluid is at -40°C. The result shown here and in Table 5.7 and Table 5.8 satisfy the general requirement that the T_{sensor} is below -20 °C and verifies that the Alpine structure can be effectively cooled down with a CO_2 two-phase cooling system.

Using the measurements of the temperature on the heater (T_{Top}) and the calculation of the temperature of the tube wall (T_{wall}), the temperature difference (=T_{Top}-T_{wall}) is used to express the thermal figure of merit of the measurements. Figure 5.24 presents the result of $TFoM_{Support}$ for M1. The measured value of M1 is 15 ±3 Kcm^2/W and satisfies the requirement.

5.6.2 ThermalGraph Prototype

Figure 5.25 (left) presents the predicted heat fluxes through the cooling tube wall for various heat load applied on the mountain of the ThermalGraph prototype as a function of the length. The conditions are T_{CO2}= -35.0°C and Fr=0.66 g/s. Since the heat load is dissipated by the in-going and out-going cooling pipes, it is assumed that half of the heat load gets into each of

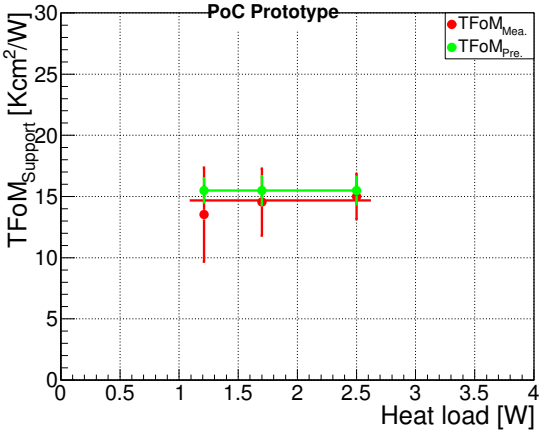

Figure 5.24: The comparison of $TFoM_{Support}$ between measurements and predictions of PoC prototype for mountain 1.

the cooling pipes. Figure 5.25 (right) shows the temperature distribution of the fluid and of the tube wall (T_{wall}) along the length of the prototype for four heat loads respectively. The maximum temperature of the tube wall happens when the CO_2 flows underneath the mountain where the heat flux is maximum.

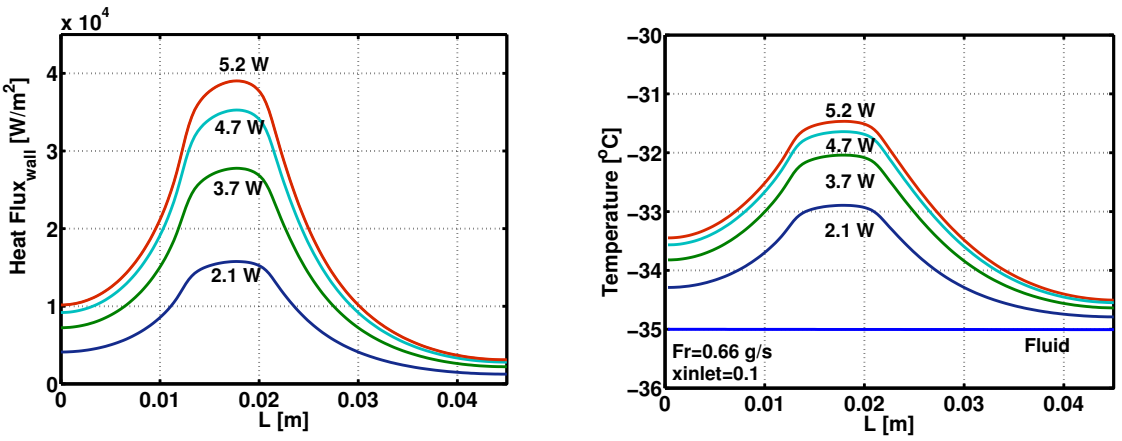

Figure 5.25: The heat flux through pipe wall as a function of the flow direction with various heat loads applied to mountain of the ThermalGraph prototype for T_{CO2}= -35.0°C and Fr= 0.66 g/s (left). CO_2 and tube wall temperature along the flow direction with different heat load applied on the mountain (right).

Figure 5.26 shows the comparison between the predictions and measurements of ΔT_{TopCO2} and $\Delta T_{Support}$. It is seen that the model fails to describe the measurement. Moreover, when the heat load exceeds 3.5 W, the ΔT_{TopCO_2} becomes larger than 15 °C, therefore the temperature on top of the mountain exceeds the general design requirement of -20 °C, if the CO_2 saturation temperature is set at -35.0°C.

The measured temperature difference $\Delta T_{Support}$ is calculated by subtracting the value of ΔT_{CO2} from ΔT_{TopCO2}. The Figure shows a linear increase of the $\Delta T_{Support}$ with the heat load, having a different slope for the predictions and the measurements. Since the ratio $\frac{\Delta T}{\dot{Q}}$ is proportional to the thermal resistance of the support structure, a higher slope indicates an extra heat resistance which is not taken into account in the prediction. The values of $TFoM_{Support}$ are shown in Figure 5.27 as a function of heat load. The measured $TFoM_{Support}$

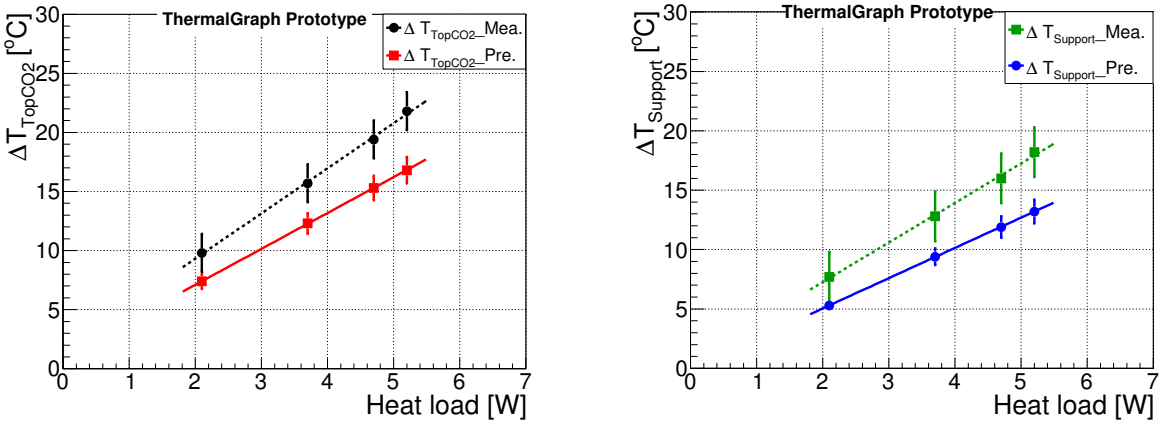

Figure 5.26: The comparison of ΔT_{TopCO2} between measurements and predictions of ThermalGraph prototype.

has an average value of 26 K·cm^2/W while the predicted value is 19 K·cm^2/W. These values are above the requirement. In the next section, the disagreement between the measurements and the predictions will be discussed.

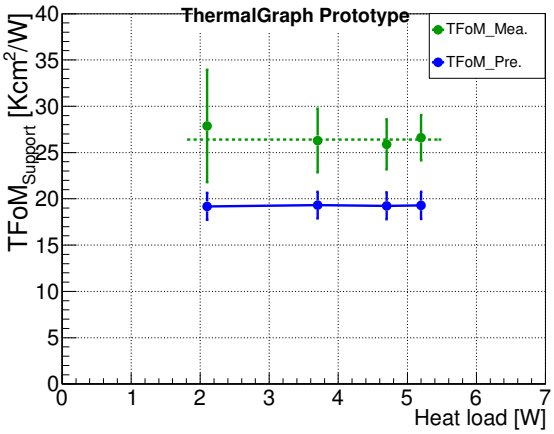

Figure 5.27: The comparison of $TFoM_{Support}$ between measurements and predictions of ThermalGraph prototype.

5.7 Discussion

The PoC prototype measurement results show a good agreement with the predictions within the uncertainties, while a difference of above 25% is seen between predictions and measurements for the ThermalGraph prototype. This suggests that in the second case additional effects are present that are not described by the model. It is important to understand the origin of the difference in order to be confident in the calculations and understand the measurements. A disagreement of 30% between the predictions and measurements was also observed for the first IBL prototype[26]. At that time, it was noted that the fraction of the cooling pipe in contact with carbon foam depends on the imperfections and voids of the foam and its pores can cause an ineffective thermal contact not included in ideal simulations.

5.7.1 Effect of the production

Glue-foam interface

The ThermalGraph prototype being tested is the first prototype built by the institute of LPSC. As mentioned in Section 5.1.2, one of the steps to produce the prototype is to glue manually the cooling pipe into the cavity of the carbon foam. During this process, there is no precise control of the thickness around the cooling pipe which is estimated to be 0.2 mm. The uncertainty on this quantity was not reliably measured, and a value of 0.05 mm was assumed as rough estimate. The variation of the glue thickness is studied in Figure 5.28. It is seen that it leads to a large uncertainty on the prediction of $\Delta T_{Support}$. A 0.1 mm extra thickness induces 1.5 °C of difference on $\Delta T_{Support}$. Figure 5.28 (right) presents the prediction of $\Delta T_{Support}$ as a function of heat load for various thickness around the cooling pipe. It is seen that if the thickness of the glue around the pipe is increased to 0.3 mm, the prediction would not manifest a similar slope as the measurement, therefore, the observed difference between the measurements and the predictions is most likely not dominated by an imperfect modelisation of the thickness of the glue.

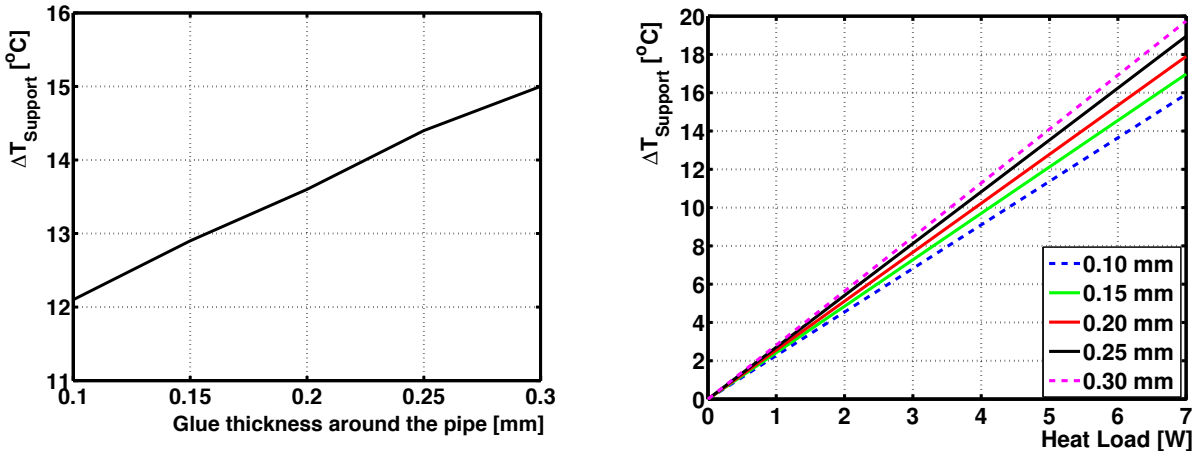

Figure 5.28: Variation of $\Delta T_{Support}$ as function of the thickness of the glue layer around the cooling pipe with power density of 0.7 W/cm^2 (left). $\Delta T_{Support}$ as a function of heat load for various glue thickness around the cooling pipe.

In addition to the average glue thickness, another concern is the uniformity of the glue layer along the longitudinal direction of the cooling pipe. During the current gluing procedure, air bubbles are easily trapped between the glue and the carbon foam due to the roughness of the carbon foam, which can generate a contact thermal resistance. The net effect at the interface can be taken in to account as a change of the effective thermal conductivity of the glue ($K_{glue'}$). Figure 5.29 (left) shows the effect of $K_{glue'}$ on $\Delta T_{Support}$. When the $K_{glue'}$ decreases, the $\Delta T_{Support}$ increases. The effect is studied as the function of heat load in Figure 5.29 (right). It is noticed that the slope of the prediction increases with the decreasing effective glue and this effect could bring the predictions in agreement with the measurements.

According to these considerations, the gluing procedure may significantly alter the thermal performance of the prototype. Therefore the gluing procedure should be documented in detail and provided by the manufacturer. A cut at the cross-section of the prototype would be helpful in examining the interfaces.

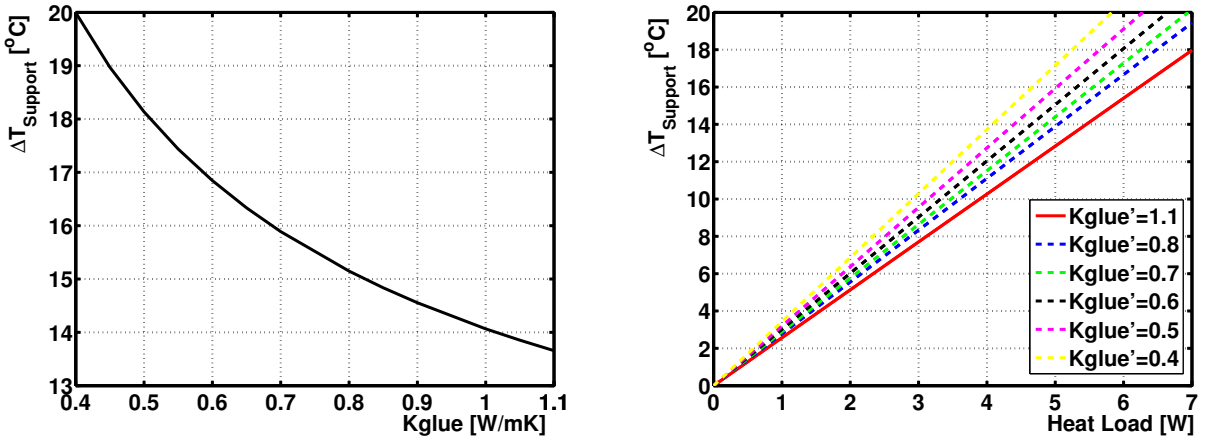

Figure 5.29: Variation of $\Delta T_{Support}$ as function of the effective therml conductivity of the glue around the cooling pipe with 0.7 W/cm^2 (left). $\Delta T_{Support}$ as a function of heat load for various effective thermal conductivity of the glue aroung the cooling pipe (right).

Carbon foam

The same technology to produce the carbon foam blocks may result in different thermal conductivity. According to the experience from IBL project, K_{foam} has a spread from 35 W/m·K to 24 W/m·K. In order to see the effect of the variation of K_{foam}, $\Delta T_{Support}$ is plotted as a function of K_{foam} in Figure 5.30. To account for this effect, a systematic error of 0.7°C was already assigned to the FEA calculations, by varying the $K_{foam}$by ±4W/m·K around a nominal value of 28 W/m·K. The $\Delta T_{Support}$ as a function of heat load with various K_{foam} is shown in the right plot. It is seen that the slope of the straight line increases when the K_{foam} decreases, but its slope is far from the measurement, hence, the variation of carbon foam is not the main cause of the difference between the measurements and predictions.

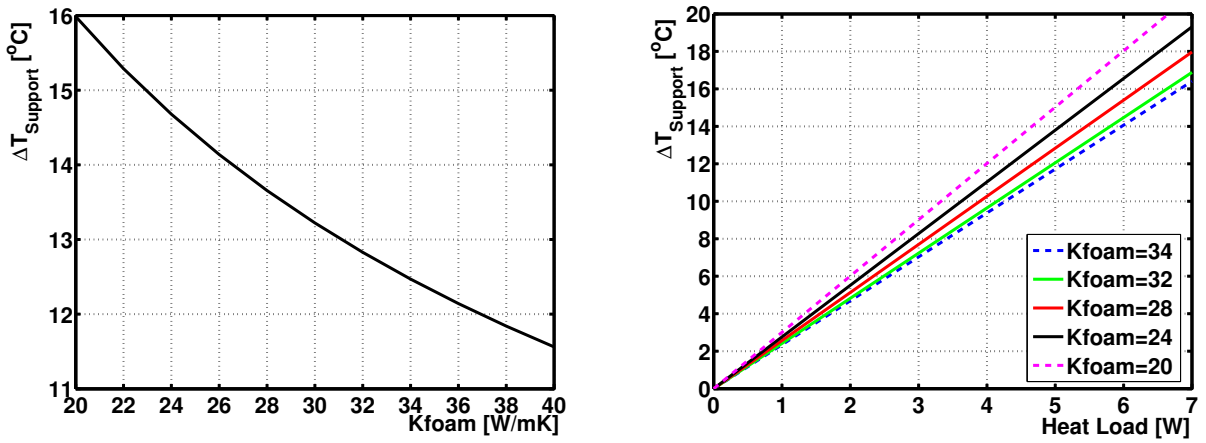

Figure 5.30: Variation of $\Delta T_{Support}$ as function of the therml conductivity of carbon foam with power density of 0.7 W/cm^2 (left). $\Delta T_{Support}$ as a function of heat load for various thermal conductivity of carbon foam (right).

5.7.2 Measurement accuracy

The accuracy of the temperature measurements is determined by the temperature probe accuracy as well as by effects such as probe calibration and heat leak from environment. The reading accuracy of the probes is guaranteed by the manufacture to be 0.3 °C, according to the data-sheet. Before each measurement, all the temperature probes are inter-calibrated to give a response within 0.1°C. These values are relatively small to explain the observed discrepancy.

During the measurement, T_{CO2} is taken as an average in different locations of the cooling pipe, and the difference among measurements is taken as uncertainty. The uncertainty on the value of T_{CO2} can be greatly reduced by using an absolute pressure sensor at CO_2 inlet of the prototype and by referencing the absolute pressure back to the saturation temperature. In this case, the measurement on T_{CO2} would have a higher accuracy limited only by the pressure measurement which is normally at per mil level.

As the measurement was carried out at room temperature, a certain amount of heat leak into the test system is unavoidable[87] and this is difficult to calculate analytically. The presence of the heat leak effects was demonstrated by the temperature difference between the top and the bottom of the mountain when no heat load was applied and the thermal equilibrium is reached. The effect of heat leak was estimated of the order of 1°C. The heat leak is affected by the quality of the thermal insulation around the prototype. The heat leak effect was further investigated by putting another prototype in a climate chamber without thermal insulation and performed the same test procedure. All the temperature sensors showed the same temperature within uncertainties when the temperature of the CO_2 was the same as the climate chamber. Increasing the temperature of the climate chamber, a temperature difference was observed between the top and bottom of the mountain of the prototype when no heat load was applied. This difference was 2.5 °C when the climate chamber was at a temperature of 20 °C. This behavior suggests that the difference between temperature probes under no heat load is due to heat leak from environment. It is foreseen therefore to improve the insulation material to reduce the heat leak effect.

5.8 Summary

In this chapter, the Proof-of-Concept (PoC) and Function-Demonstration (FD) prototypes are produced and tested with an CO_2 two-phase cooling system. The PoC prototype is manufactured with IBL production procedure and tested to verify the feasibility of Alpine design, and the FD prototype is manufactured with the real shape of Alpine stave and new production procedure and used to demonstrate the thermal performance of the Alpine stave. The modeling with respect to analyzing the thermal performance of the prototype are based on the FEA and CoBra program.

The measurement results of PoC prototype shows a feasibility of the Alpine design since the value of $TFoM_{Support}$ is 15 ± 3 K·cm^2/W which is close to the thermal requirement. While for one of the FD prototypes, ThermalGraph, an disagreement is observed between the measurements and the predictions. The FD prototype has an $TFoM_{Support}$ of 26 ± 4 K·cm^2/W, which is higher than the predicted value as well as of the thermal requirement. The main cause may be due to the gluing procedure which is not completely under control. This effect cannot be quantitatively evaluated and therefore cannot be introduced in the model. It is noted that this prototype is not manufactured based on the design specifics. By the future prototypes which use more efficient material at heat dissipation and take better production procedure to control the parameters, the thermal performance is expected to be improved to satisfy the requirements.

Chapter 6

Conclusion and Outlook

This thesis has introduced a novel layout "Alpine" pixel detector for the ATLAS ID upgrade during phase II for the HL-LHC. In this Alpine Detector, the sensors are almost perpendicularly to the track of the particles emerging from the interaction of the beam. The local support structure to support and cool the modules, the Alpine stave, is designed with an optimized geometry and with an advanced CO_2 two-phase cooling system. A numerical program, CoBra, simulating the CO_2 evaporative heat transfer flowing through a pipe is developed in this thesis using the most up to date CO_2 flow pattern map and heat transfer and pressure drop models. With this program, it is verified that the CO_2 two-phase system can be used to efficiently cool down the detector. Based on the preliminary thermal requirements, this thesis has proposed few parameters for cooling the Alpine detector. They include in particular:

- the optimal diameter of the cooling pipe inside the Alpine Pixel detector: 1.3 mm for layer 1; 1.6 for layer 2 and 1.9 mm for layer 3. For the reason of production simplification, 1.5 mm is recommended for both layer 1 and layer 2.

- the range of the mass flow rate for thermal test: between 0.5 g/s to 2 g/s by considering the margin to the dry-out phenomenon and taking advantage of the high heat transfer coefficient.

In addition, in this thesis, the temperature and pressure distributions are also discussed and present assuming a uniform heat flux or using the more realistic non-uniform heat flux.

A FEA model of the local support structure at the mountain region is built for thermal analysis. With respect to reducing the mass of the material, manufacture procedure, mechanical stiffness and thermal performance, the geometry of the local support is optimized. The main optimization of the support structure are listed here:

- the material of the face-plate can be in carbon graphite such as TPG, which has high thermal conductivity through and along planes. It is better to select the material of the glue with a thermal conductivity above 2.5 W/mK assuming that the thickness is 0.1 mm.

- removing the material of electrical insulation, the Parylen, and considering other method of insulate.

- the U-shape structure underneath the mountain can provide a better stiffness

- making a groove at the base support carbon form is easier to implement the cooling pipe without introducing too much extra mass of glue

- the distance between in-going and out-going pipes can be between 14 mm and 16 mm

The two simulations (CoBra and the FEA) are combined to characterize the thermal performance of two prototypes: PoC prototype and FD prototype. The measurements done with the PoC prototype shows that the Alpine design can be effectively cooled down. The measurements agree with the predictions within the considered systematic uncertainties, and its TFoM is about 15 Kcm^2/W, close to the thermal requirement. While the first FD prototype produced based on the optimized Alpine geometry with limited improvements on materials shows a less satisfactory behavior. The FD prototype has an average vale of $TFoM_{Support}$ at 26 Kcm^2/W, which is higher than the predicted value by 25%. Both the predictions and measurements are higher than the thermal requirement. Since the FD prototype is the first tentative production, possible effects occurring during the production are discussed.

In order to improve the thermal performance of the future prototype, two aspects are under consideration:

- The interface between the carbon foam and the cooling pipe will be investigated to calculate the potential contact resistance. The measured contact resistance can be considered as an input parameter in the simulation to account for this production parameter. A well-controlled gluing procedure will be applied for controlling the thickness of the glue layer.

- The simulation prediction shows that using a ThermalGraph material with 300 microns rather than 30 microns as the face-plate provides a better thermal performance by 4 °C under the power density of 0.7 W/cm^2. A new prototype is planned to be produced for verifying this prediction.

From the point of view of the thermal measurements, a pressure transducer can be installed locally where the tested prototype is connected in the test set-up. According to the measurement of the pressure, the local CO_2 fluid temperature is derived. This method will improve the accuracy of the fluid temperature measurement.

Bibliography

[1] Lyndon Evans and Philip Bryant. LHC Machine. *Journal of Instrumentation*, 2008.

[2] ATLAS collaboration. *Letter of Intent for a General-Purpose pp Experiment at the Large Hadron Collider at CERN*. CERN/LHCC, 1992.

[3] ALICE Collaboration. *ALICE : Technical proposal for a Large Ion collider Experiment at the CERN LHC, CERN-LHCC-95-71* . CERN, 1995.

[4] CMS Collaboration. *CMS Technical Proposal , CERN-LHCC-94-38* . CERN, 1994.

[5] LHCb Collaboration. *LHCb : Technical Proposal, CERN-LHCC-98-004* . CERN, 1998.

[6] W W Armstrong, et al. ATLAS: Technical proposal for a general-purpose p p experiment at the Large Hadron Collider at CERN. Technical report, 1994.

[7] A Airapetian, et al. *ATLAS detector and physics performance: Technical Design Report, 1.* CERN, 1999.

[8] G Aad, et al. Observation of a new particle in the search for the Standard Model Higgs boson with the ATLAS detector at the LHC. *Physics Letters B*, 2012.

[9] Jörn Grosse-Knetter. The ATLAS pixel detector. *Nuclear Instruments and Methods in Physics Research Section A: Accelerators, Spectrometers, Detectors and Associated Equipment*, 2006.

[10] ATLAS IBL Collaboration. Production and Integration of the ATLAS Insertable B-Layer (Draft) . Technical report, 2015.

[11] A Miucci. The ATLAS Insertable B-Layer project. *Journal of Instrumentation*, 2014.

[12] A Abdesselam, et al. The barrel modules of the ATLAS semiconductor tracker. *Nuclear Instruments and Methods in Physics Research Section A: Accelerators, Spectrometers, Detectors and Associated Equipment*, 2006.

[13] A Abdesselam, et al. The ATLAS semiconductor tracker end-cap module. *Nuclear Instruments and Methods in Physics Research Section A: Accelerators, Spectrometers, Detectors and Associated Equipment*, 2007.

[14] A Ahmad, et al. The silicon microstrip sensors of the ATLAS semiconductor tracker. *Nuclear Instruments and Methods in Physics Research Section A: Accelerators, Spectrometers, Detectors and Associated Equipment*, 2007.

[15] Y Unno. ATLAS silicon microstrip detector system (SCT). *Nuclear Instruments and Methods in Physics Research*, 2003.

[16] E Abat and others. The ATLAS TRT barrel detector. *JINST*, 2008.

[17] E Abat and others. The ATLAS Transition Radiation Tracker (TRT) proportional drift tube: Design and performance. *JINST*, 2008.

[18] V A Mitsou and for the ATLAS TRT collaboration. The ATLAS Transition Radiation Tracker. *arXiv.org*, 2003.

[19] M Aharrouche. The ATLAS liquid argon calorimeter: Construction, integration, commissioning and combined test beam results. *Nuclear Instruments and Methods in Physics Research Section A: Accelerators, Spectrometers, Detectors and Associated Equipment*, 2007.

[20] P Adragna, et al. The ATLAS hadronic tile calorimeter: from construction toward physics. *IEEE Trans. Nucl. Sci.*

[21] Sandro Palestini. The muon spectrometer of the ATLAS experiment. *Nuclear Physics B - Proceedings Supplements*, 2003.

[22] J Snuverink. *The ATLAS muon spectrometer*. PhD thesis, 2009.

[23] Giorgio Apollinari, Oliver Brüning, and Lucio Rossi. High Luminosity LHC Project Description. Technical report, 2014.

[24] Heinz Pernegger. The Pixel Detector of the ATLAS Experiment for LHC Run-2. Technical report, 2015.

[25] A La Rosa. ATLAS IBL Pixel Upgrade. *Nuclear Physics B - Proceedings Supplements*, 2011.

[26] Jennifer Jentzsch. Performance tests during the ATLAS IBL Stave Integration. Technical report, 2014.

[27] C Gallrapp. Planar Pixel Sensors for the ATLAS tracker upgrade at HL-LHC. *Nucl. Instrum. Methods Phys. Res., A*, 2012.

[28] D Aruntinov, et al. Experience with 3D integration technologies in the framework of the ATLAS pixel detector upgrade for the HL-LHC. *Nucl. Instrum. Methods Phys. Res., A*, 2013.

[29] Giovanni Darbo. Experience on 3D Silicon Sensors for ATLAS IBL. Technical report, 2014.

[30] ATLAS collaboration. Letter of Intent for the Phase-II Upgrade of the ATLAS Experiment. Technical report, 2013.

[31] P Weigell. Recent Results of the ATLAS Upgrade Planar Pixel Sensors Research and Development Project. *Nucl. Instrum. Methods Phys. Res., A*, 2013.

[32] M Bomben. Novel Silicon n-on-p Edgeless Planar Pixel Sensors for the ATLAS upgrade. *Nucl. Instrum. Methods Phys. Res., A*, 2013.

[33] M Bomben. Development of Edgeless n-on-p Planar Pixel Sensors for future ATLAS Upgrades. *Nucl. Instrum. Methods Phys. Res., A*, 2013.

[34] G Lindstrom. Radiation damage in silicon detectors. *Nuclear Instruments and Methods in Physics Research*, 2003.

[35] S Feigl. Performance of capacitively coupled active pixel sensors in 180 nm HV-CMOS technology after irradiation to HL-LHC fluences. *J. Instrum.*, 2014.

[36] Simone Coelli. Mechanics and infrastructure for the ATLAS Pixel Detector. *Nuclear Physics B - Proceedings Supplements*, 2007.

[37] R J Apsimon, et al. Application of advanced thermal management technologies to the ATLAS SCT barrel module baseboards. *Nuclear Instruments and Methods in Physics Research Section A: Accelerators, Spectrometers, Detectors and Associated Equipment*, 2006.

[38] Mukund Gupta. Calculation of radiation length in materials. Technical report, 2010.

[39] James Klett, et al. High-thermal-conductivity, mesophase-pitch-derived carbon foams: effect of precursor on structure and properties. *Carbon*, 2000.

[40] Thermal conductivity database of various structural carbon-carbon composite materials.

[41] Graham Beck and Georg Viehhauser. Analytic model of thermal runaway in silicon detectors. *Nuclear Instruments and Methods in Physics Research Section A: Accelerators, Spectrometers, Detectors and Associated Equipment*, 2010.

[42] W O Miller, A Seiden, and C Haber. Thermal runaway in silicon strip detectors. 1995.

[43] C Bayer, et al. Development of fluorocarbon evaporative cooling recirculators and controls for the ATLAS inner silicon tracker. In *2000 IEEE Nuclear Science Symposium. Conference Record*, 2000.

[44] B Gorski, et al. The design and prototyping of the ATLAS inner detector evaporative cooling system. In *IEEE Symposium Conference Record Nuclear Science 2004.*

[45] Hoo-Kyu Oh, et al. Flow boiling heat transfer characteristics of carbon dioxide in a horizontal tube. *Applied Thermal Engineering*, 2008.

[46] Xiulan Huai, et al. An experimental study of flow boiling characteristics of carbon dioxide in multiport mini channels. *Applied Thermal Engineering*, 2004.

[47] Jostein Pettersen. *Flow Vaporization of CO2 in Microchannel Tubes.* PhD thesis, 2002.

[48] B Verlaat, M Van Beuzekom, and A Van Lysebetten. *CO2 cooling for HEP experiments.* Topical Workshop on Electronics for Particle Physics (TWEPP-2008), Naxos, Greece, 2008.

[49] A A M Delil, A A Woering, and B. Verlaat. Development of a Mechanically Pumped Two-Phase CO2 Cooling Loop for the AMS-2 Tracker Experiment. *NLR Technical Note*, 2003.

[50] D C Mo, et al. Comparison of Pressure Drop between Calculation and Experiment for a Two-phase Carbon Dioxide Loop. *Microgravity Science and Technology*, 2008.

[51] Marek Gutt-Mostowy and Piotr Cyklis. *CO2 flexible vacuum Insulated transfer line for ATLAS IBL detector cooling system.* PhD thesis, Cracow Tech. U., 2013.

[52] A Van Lysebetten, B Verlaat, and M Van Beuzekom. CO2 cooling experience (LHCb). *PoS*, 2007.

[53] Bart Verlaat, A Van Lysebetten, and M Van Beuzekom. COOLING FOR THE LHCB-VELO EXPERIMENT AT CERN. In *IIFI/IR Gustav Lorentzen conference on Nature Working Fluids*, 2008.

[54] Bart Verlaat. Controlling a 2-phase CO2 loop using a 2-phase accumulator. In *22nd International Congress of Refrigeration*.

[55] Bart Verlaat and Joao Noite. Design Considerations of Long Length Evaporative CO2 Cooling Lines. *Proceedings of 10h IIF/IIR Gustav Lorentzen Conference on Natural Refrigerants*, 2012.

[56] Frank P Incropera and David P DeWitt. *Fundamentals of heat and mass transfer; 5th ed.* Wiley, 2002.

[57] Rin Yun, et al. Boiling heat transfer and dryout phenomenon of CO2 in a horizontal smooth tube. *International Journal of Heat and Mass Transfer*, 2003.

[58] J R Thome. *Chapter 12 Two-Phase Flow Patterns*. Wolverine engineering data book III, 2004.

[59] N Kattan, J R Thome, and D Favrat. Flow Boiling in Horizontal Tubes: Part 1—Development of a Diabatic Two-Phase Flow Pattern Map. *Journal of Heat Transfer*, 1998.

[60] Lixin Cheng, et al. New prediction methods for CO2 evaporation inside tubes: Part I – A two-phase flow pattern map and a flow pattern based phenomenological model for two-phase flow frictional pressure drops. *International Journal of Heat and Mass Transfer*, 2008.

[61] J R Thome. *Chapter 17 Void Fractions in Two-Phase Flows*. Wolverine engineering data book III.

[62] Jesus MORENO QUIBEN. *Experimental and Analytical Study of Two-phase Pressure Drops During Evaporation in Horizontal Tubes*. PhD thesis, 2005.

[63] Rémi Revellin and John R Thome. Adiabatic two-phase frictional pressure drops in microchannels. *Experimental Thermal and Fluid Science*, 2007.

[64] Satish G Kandlikar. Fundamental issues related to flow boiling in minichannels and microchannels. *Experimental Thermal and Fluid Science*, 2002.

[65] Jesús Moreno Quibén and John R Thome. Flow pattern based two-phase frictional pressure drop model for horizontal tubes. Part I: Diabatic and adiabatic experimental study. *International Journal of Heat and Fluid Flow*, 2007.

[66] Jesús Moreno Quibén and John R Thome. Flow pattern based two-phase frictional pressure drop model for horizontal tubes, Part II: New phenomenological model. *International Journal of Heat and Fluid Flow*, 2007.

[67] J R Thome. *Chapter 13 Two-Phase Pressure Drops*. Wolverine engineering data book III, 2006.

[68] J R Thome, V Dupont, and A M Jacobi. Heat transfer model for evaporation in microchannels. Part I: presentation of the model. *International Journal of Heat and Mass Transfer*, 2004.

[69] V Dupont, J R Thome, and A M Jacobi. Heat transfer model for evaporation in microchannels. Part II: comparison with the database. *International Journal of Heat and Mass Transfer*, 2004.

[70] Lixin Cheng, Gherhardt Ribatski, and John R Thome. New prediction methods for CO2 evaporation inside tubes: Part II—An updated general flow boiling heat transfer model based on flow patterns. *International Journal of Heat and Mass Transfer*, 2008.

[71] Sung-Min Kim and Issam Mudawar. Universal approach to predicting saturated flow boiling heat transfer in mini/micro-channels – Part I. Dryout incipience quality. *International Journal of Heat and Mass Transfer*, 2013.

[72] Sung-Min Kim and Issam Mudawar. Universal approach to predicting saturated flow boiling heat transfer in mini/micro-channels – Part II. Two-phase heat transfer coefficient. *International Journal of Heat and Mass Transfer*, 2013.

[73] Satish G Kandlikar, et al. Flow boiling in minichannels and microchannels. In *Heat Transfer and Fluid Flow in Minichannels and Microchannels*. 2006.

[74] S G Kandlikar. A General Correlation for Saturated Two-Phase Flow Boiling Heat Transfer Inside Horizontal and Vertical Tubes. *Journal of Heat Transfer*, 1990.

[75] J P Holman. *Heat transfer 9th Edition*. New York, 2002.

[76] X H Sun, et al. Analysis of Temperature Oscillations in Parallel Evaporators of a Carbon Dioxide Two-Phase Loop. *Microgravity Science and Technology*, 2009.

[77] F Vakili-Farahani, B Agostini, and J R Thome. Experimental study on flow boiling heat transfer of multiport tubes with R245fa and R1234ze(E). *International Journal of Refrigeration*, 2013.

[78] *Pixel ITk Mechanical Requirements*, 2014.

[79] *Updates on the evaporation temperature requirement for Pixel*, 2015.

[80] Saeed Moaveni. *Finite element analysis: theory and application with ANSYS; 2nd ed.* Prentice-Hall, 2003.

[81] M F Ashby. Multi-objective optimization in material design and selection. *Acta Materialia*, 2000.

[82] Momentive. TPG Thermal Management Material.

[83] Momentive. High Thermal Conductivity Graphite and Composites .

[84] AMEC Thermasol. THERMAGRAPH MATERIALS FGS 003.

[85] X Tang, et al. *Carbon Nanotube Enhanced Thermally and Electrically Conductive Adhesive for Advanced Packaging* . IEEE, 2010.

[86] F Joshua. Design and Construction of a Concentric Tube Heat Exchanger. *AU JT*, 2009.

[87] G Barbier, et al. Thermal Grease Evaluation for ATLAS Upgrade Micro-Strip Detector. Technical report, 2010.

Appendix A

Momentum pressure drop

$$\Delta P_{mon} = G^2\{[\frac{(1-x)^2}{\rho_L(1-\epsilon)} + \frac{x^2}{\rho_V\epsilon}]_{out} - \frac{(1-x)^2}{\rho_L(1-\epsilon)} + \frac{x^2}{\rho_V\epsilon}]_{in}\} \tag{A.1}$$

Parameters of Friedel correlation

$$\rho_H = (\frac{x}{\rho_V} + \frac{1-x}{\rho_L}) \tag{A.2}$$

$$E = (1-x)^2 + x^2(\frac{\rho_L f_{VO}}{\rho_G f_{LO}}) \tag{A.3}$$

$$F = x^{0.87}(1-x)^{0.224} \tag{A.4}$$

$$H = (\frac{\rho_L}{\rho_G})^{0.91}(\frac{\mu_G}{\mu_L})^{0.91}(1-\frac{\mu_G}{\mu_L})^{0.7} \tag{A.5}$$

Homogeneous dynamic viscosity

$$\mu_H = \mu_L(1-x) + \mu_V x \tag{A.6}$$

Dry-out vapor quality

$$x_{di} = 0.58e[0.52 - 0.236We_V^{0.17}F_{RV}^{0.17}(\frac{\rho_V}{\rho_L})^{-0.25}(\frac{q}{q_{crit}})^{-0.27}] \tag{A.7}$$

$$x_{de} = 0.61e[0.57 - 0.502We_V^{0.16}F_{RV}^{0.15}(\frac{\rho_V}{\rho_L})^{-0.09}(\frac{q}{q_{crit}})^{0.72}] \tag{A.8}$$

where We_V and F_{RV} are the vapor Weber number and Froude number.

Critical heat flux

$$q_{crit} = 0.131\rho_V^{0.5}h_{LV}[g\sigma(\rho_L - \rho_V)]^{0.25} \tag{A.9}$$

Parameters of the flow boiling heat transfer

$$h_{wet} = [(Sh_{nb})^3 + h_{cb}^3]^{1/3} \tag{A.10}$$

S is the nucleate boiling heat transfer suppression factor. When $x < x_{IA}$, S =1, when $x \geq x_{IA}$,

$$S = 1 - 1.14(\frac{D_{eq}}{0.00753})^2(1 - \frac{\delta}{\delta_{IA}}) \tag{A.11}$$

If $D_{eq} > 7.53$ mm, set $D_{eq} = 7.53$ mm. The liquid film thickness δ is

$$\delta = \frac{D_{eq}}{2} - [(\frac{D_{eq}}{2})^2 - \frac{2A_L}{2\pi - \theta_{dry}}]^{1/2} \tag{A.12}$$

whenever $\delta > D_{eq}/2$, δ is set equal to $D_{eq}/2$. The liquid film δ_{IA} is calculated at the transition between intermittent flow to annular flow.

$$h_{nb} = 131P_r^{-0.0063}(-\log_{10} Pr)^{-0.55}M^{-0.5}q^{0.58} \tag{A.13}$$

The convective boiling heat transfer coefficient h_{cb} is calculated with:

$$h_{cb} = 0.0133[\frac{4G(1-x)\delta}{\mu_L(1-\epsilon)}]^{0.69}[\frac{C_{pL}\mu_L}{k_L}]^{0.4}\frac{k}{\delta} \tag{A.14}$$

Parameters of heat transfer of mist flow

$$Re_H = \frac{GD_{eq}}{\mu_V}[x + \frac{\rho_V}{\rho_L}(1-x)] \tag{A.15}$$

$$Y = 1 - 0.1[(\frac{\rho_L}{\rho_V} - 1)(1-x)]^{0.4} \tag{A.16}$$

List of Figures

List of Tables